

# Transport Properties of the Half-Metallic Heusler Alloy NiMnSb: Influence of Relaxation and Lattice Defects

Dissertation

zur Erlangung des akademischen Grades

Dr. rer. nat.

eingereicht an der

Mathematisch-Naturwissenschaftlich-Technischen Fakultät

der Universität Augsburg

von

**Andreas Prinz-Zwick**

Augsburg, Dezember 2017



Universität Augsburg  
Institut für Physik

Erstgutachter: Prof. Dr. Ulrich Eckern  
Zweitgutachter: Prof. Dr. Liviu Chioncel

Tag der mündlichen Prüfung: 23. Februar 2018

# Contents

<b>1</b>	<b>Introduction</b>	<b>1</b>
<b>2</b>	<b>Basics of Density Functional Theory</b>	<b>9</b>
2.1	The Hohenberg-Kohn Theorem . . . . .	9
2.2	The Kohn-Sham Equations . . . . .	13
2.3	Exchange Correlation Functional . . . . .	21
2.4	The SIESTA Code . . . . .	22
2.5	Pseudopotentials . . . . .	23
<b>3</b>	<b>Basics of Transport Theory</b>	<b>31</b>
3.1	The Transport Problem . . . . .	31
3.2	Non-Equilibrium Green's Function Formalism . . . . .	33
3.3	The SMEAGOL Code . . . . .	41
<b>4</b>	<b>Transport in the Kronig-Penney Model</b>	<b>43</b>
4.1	The Kronig-Penney Model . . . . .	43
4.2	The Transfer Matrix Method . . . . .	49
4.3	A Toy Model for Half-Metallic Transport . . . . .	53
<b>5</b>	<b>Material and System Setup</b>	<b>67</b>
5.1	About Heusler Alloys and NiMnSb . . . . .	67
5.2	The Transport Setup . . . . .	73
<b>6</b>	<b>Transmission Without Defects</b>	<b>77</b>
6.1	One Unit Cell NiMnSb . . . . .	77
6.2	Two Unit Cells NiMnSb . . . . .	84
6.3	Three Unit Cells NiMnSb . . . . .	91
6.4	Four Unit Cells NiMnSb . . . . .	94
6.5	Conclusion . . . . .	98
<b>7</b>	<b>Transmission with Defects</b>	<b>101</b>
7.1	Vacancy at Ni site . . . . .	101
7.2	Unexpected Antiparallel Ordering . . . . .	110
7.3	Swapping of Mn and Ni . . . . .	114
7.4	Conclusion . . . . .	126
<b>8</b>	<b>Summary and Conclusion</b>	<b>127</b>
	<b>Acknowledgement/Danksagung</b>	<b>133</b>
	<b>Bibliography</b>	<b>135</b>



# 1 Introduction

In this thesis, two technical terms will come up remarkably often: “Heusler alloy” and “half-metallic”. The former is a collective description for a class of alloys whose history goes back to the early years of the last century, when they were discovered by the German mining engineer FRIEDRICH HEUSLER in 1903 [1], and the latter is a descriptive adjective for an even broader class of materials, who came to their name 80 years later, when DE GROOT *et al.* published his famous paper about this new class of materials [2].

The novelty of those half-metallic materials was that metallic as well as insulating/semiconducting properties can be observed in the *same* material at the *same* time. This is possible because the two spin channels show a completely different behavior. While the majority spin channel is metallic, the minority channel possesses a band gap around the Fermi level. A direct consequence of this fact is that the total magnetization per unit cell (in  $\mu_B$ ) has always an integer value, and the spin polarization at the Fermi level is predicted to be 100%.

The two keywords “Heusler alloy” and “half-metallic” can often be found in the same context because the family of Heusler alloys contributes a huge part to the family of half-metallic materials. An example of a half-metallic Heusler alloy is NiMnSb, which is the material for which half-metallicity was first discovered by DE GROOT. The family of half-metals also contains non-Heusler materials which do not play a role in this thesis, but shall be mentioned nevertheless in order to give an overview of the field.

***Non-Heusler half-metals.*** One example for non-Heusler half-metals are metal oxides such as  $\text{CrO}_2$ , for which the spin polarization was measured using superconducting point contacts by SOULEN *et al.* [3]. The results of this measurement showed that the spin polarization for this material is about 90%. Another subclass of potential half-metals, namely manganites (manganese oxides) were also discussed in the same paper. For the compound  $\text{La}_{0.7}\text{Sr}_{0.3}\text{MnO}_3$  a spin polarization of roughly 80% was found. Another class of materials that can show half-metallicity are the double perovskites. A series of  $^{75}\text{Re}$  (rhenium) based compounds of this family were investigated by KATO *et al.* [4], where especially for  $\text{Sr}_2\text{CrReO}_6$  and  $\text{Sr}_2\text{FeReO}_6$  half-metallic properties were found for the intergrain tunneling magnetoresistance in polycrystalline samples. Pyrites, a subgroup of the sulfides are also capable of developing half-metallicity, as was shown by SHISHIDOU *et al.* for the ferromagnetic material  $\text{CoS}_2$ , by means of computational simulations [5]. Some compounds from

the family of zinc-blende structures, consisting of transition metals such as CrAs or CrSb, also provide a half-metallic band structure, as calculated by GALANAKIS *et al.* [6] in a computational study. Doped semiconductors such as  $\text{Mn}_x\text{Ge}_{1-x}$  can also show half-metallicity for special doping concentrations, as was found by STROPPA *et al.* who calculated the electronic structure of MnGe and MnSi using density functional theory [7]. For the aforementioned  $\text{Mn}_x\text{Ge}_{1-x}$  half-metallicity was found for  $x = 0.03125$ , whereas for the MnSi semiconductor no half-metallic behaviour was observed.

**Heusler alloys.** Going back to Heusler alloys, one distinguishes full-Heusler and half-Heusler compounds. Full-Heusler alloys are of the form  $\text{X}_2\text{YZ}$  where X is a transition metal and Y and Z are from the 5th to 8th main group. Among the full-Heusler alloys there are also inverse full-Heuslers, where one of the X atoms switches places with the Y or Z atom. Half-Heuslers are of the form XYZ, and can be generated from a full-Heusler alloy by replacing one specific X atom with a vacancy. Heusler alloys form a face centered cubic lattice, and the atoms are positioned on the space diagonal of the primitive unit cell. The distance between the atomic positions is one fourth of the length of that space diagonal. In the common notation for a full-Heusler alloy, the two X atoms occupy the  $(0, 0, 0)$  and the  $(\frac{1}{2}, \frac{1}{2}, \frac{1}{2})$  positions, and the Y and Z atoms occupy the  $(\frac{1}{4}, \frac{1}{4}, \frac{1}{4})$  and  $(\frac{3}{4}, \frac{3}{4}, \frac{3}{4})$  positions, respectively. The very first Heusler alloy that was discovered in 1903 is the full-Heusler  $\text{Cu}_2\text{MnAl}$  [1], which is ferromagnetic, although all the elements this compound consists of, are not.

Regarding half-metallicity, other full-Heuslers are more promising (in terms of computational simulations), namely the Co based compounds  $\text{Co}_2\text{MnGe}$  or  $\text{Co}_2\text{MnSi}$ . Those were predicted to be half-metallic by ISHIDA *et al.* [8], and later further investigated by PICOZZI *et al.* [9], where also strain effects were taken into account. In the case of  $\text{Co}_2\text{MnSi}$ , half-metallicity was directly observed by JOURDAN *et al.* using ultraviolet-photoemission spectroscopy and high energy X-ray photoemission spectroscopy, which yielded a spin polarization of roughly 93% at room temperature [10].

As an example for an inverse full-Heusler alloy, the compound  $\text{Ti}_2\text{FeSn}$  was predicted to be half-metallic by BIRSAN [11]. In that compound the Fe atom switches places with the second Ti atom, so that Fe is positioned at  $(\frac{1}{2}, \frac{1}{2}, \frac{1}{2})$  and Ti at  $(\frac{1}{4}, \frac{1}{4}, \frac{1}{4})$ . The band gap in the spin- $\downarrow$  channel was found to be about 0.5 eV wide.

Half-Heusler alloys are particularly interesting for this work, since the transport properties for NiMnSb are investigated, which is the most famous half-metallic half-Heusler compound. Today many more half-metals from this family are known, such as the Co or Fe based alloys  $\text{CoMnSb}$  and  $\text{FeMnSb}$ , as shown by GALANAKIS [12] and DE GROOT [13]. Although all these three materials share the feature of containing Mn as well as Sb, there are many other half-Heusler alloys such as NiCrSi and NiMnSi that were predicted to be half-metallic by GALANAKIS *et al.* [14] in a computational study, where special emphasis was put on the influence of defects

and interfaces.

This is a very crucial point, since half-metallicity is mainly a bulk property and perturbations to the periodic structure of a crystal, for example, defects or a surface, may destroy the half-metallic properties.

**Interfaces.** For the transport setup which is used in this thesis, NiMnSb is connected to gold leads. This creates an interface that is especially interesting with respect to half-metallicity. Another example for interfaces corrupting half-metallicity was given by PICOZZI *et al.* who investigated the interface properties of Co<sub>2</sub>MnGe and Co<sub>2</sub>MnSi on GaAs and Ge in a computational study [15, 16]. Although interfaces may be very destructive regarding half-metallicity, according to GALANAKIS it is still possible to achieve a high spin polarization, as he found in his investigations of the Co<sub>2</sub>CrAl/InP interface using density functional theory [17]. For the half-Heusler compound NiMnSb, the structural and magnetic properties of the (001) and the (111) surface were calculated by LEŽAIĆ *et al.* [18], with the result that the Mn/Sb terminated surface shows electronic and magnetic properties similar to the bulk.

The importance of interfaces is also substantiated by experiment, because experimental methods that are especially sensitive to surfaces and interfaces tend to show a smaller spin polarization. An early example for this was given by BONA *et al.* in 1985, where spin polarized photoemission experiments were carried out on NiMnSb, for which at most a 50% spin polarization was found [19].

As another example, CLOWES *et al.* used point contact Andreev reflection (PCAR) with niobium tips to measure the transport current spin polarization at the free surface of bulk NiMnSb at a temperature of 4.2 K [20]. The maximal value for the spin polarization was found to be only 44%, also a remarkably large deviation from the theoretical full polarization. Similar results were found by RITCHIE *et al.* who measured the spin polarization of Co<sub>2</sub>MnSi and NiMnSb, also with PCAR, and determined the polarization to be 56% and 45%, respectively [21].

Using a superconducting quantum interference device (SQUID) magnetometer, for low temperatures (5 K), they found the saturation magnetisation of NiMnSb to be  $4.02 \mu_B$  per formula unit, which comes very close to the theoretical value of  $4 \mu_B$ , which will be explained in detail in chapter five. TURBAN *et al.* grew thin films of NiMnSb onto a vanadium substrate, which itself was grown onto a MgO substrate [22]. A measurement of the saturation magnetization yielded a value of  $3.9 \pm 0.2 \mu_B$  per formula unit. An interesting discovery, especially with regard to this thesis, was that already these films of NiMnSb have all the electric and magnetic properties of the bulk, however this does not hold for the film surface.

KOMESU *et al.* epitaxially grew NiMnSb onto Mo (which was again grown on MgO) and capped the NiMnSb layer with a 1000 Å layer of Sb to prevent oxidization [23]. X-ray absorption spectroscopy (XAS) and spin polarized inverse photoemission spectroscopy (SPIPES) was used, showing that the polarization decreases with increasing thickness of the Sb capping layer. In his work together with RISTOIU,

they were able to indicate a conduction band edge about 250 meV above the Fermi level, which is consistent with band structure calculations. A crucial observation was that the surface of NiMnSb is very fragile and that the surface preparation may have a significant impact on the electronic structure. A first-principle study of the role of stoichiometric as well as nonstoichiometric defects on NiMnSb was done by ALLING *et al.* with the result that defects with low formation energies can preserve half-metallicity. Some defects even increase the magnetic moment [24].

**Disorder.** Another important question in addition to interfaces and surfaces with respect to electronic structure and stability is disorder. Studies on this topic are particularly interesting because the growth of the crystals may very well result in disorder, which was investigated for the full-Heusler compound  $\text{Co}_2\text{FeSi}$  by JENICHEN *et al.* by means of transmission electron microscopy (TEM) and X-ray diffraction [25]. For the half-Heusler compound NiMnSb the growth on MgO and Si was studied by SCHLOMKA *et al.* [26] using X-ray scattering. The surface roughness of the *in situ* grown NiMnSb increased with thickness of the films. Optimal growth conditions were found for the substrate MgO at a temperature of 250 °C. An *ab initio* study on disorder was done by LARSON *et al.* who analysed several structures for half-Heusler compounds, using density functional theory [27]. It was shown that the structure of NiMnSb was the most stable among the considered structures.

Atomic disorder that often occurs in thin films was studied by ORGASSA *et al.* [28]. Several kinds of defects were investigated, employing the layer Korringa-Kohn-Rostoker (KKR) method. The result was that for a very low concentration of defects, states form in the minority spin gap but half-metallicity is still preserved. However, when the concentration of defects exceeds a certain level, the spin polarization drops dramatically and half-metallicity is lost.

For the full-Heusler alloy  $\text{Cr}_2\text{CoAl}$  a combined experimental and computational study was presented by KUDRYAVTSEV *et al.* [29]. By using flash evaporation on glass surfaces at different temperatures, they managed to create different strengths of disorder with the result that the saturation magnetization and the Curie temperature of the alloy is reduced. Recent studies show that, to a certain degree, disorder may be beneficial to thermoelectric properties of Heusler alloys [30]. An *ab initio* study on the influence of disorder on the spin polarization was carried out by HASNIP *et al.* for the full-Heusler compound  $\text{Co}_2\text{Fe}_x\text{Mn}_{1-x}\text{Si}$ . It was shown that the type of disorder has a strong influence on half-metallicity. The spin polarization may be lowered or even reversed for one kind of disorder, but may be untouched by another [31]. Optical measurements on NiMnSb were carried out by MANCOFF *et al.* for a large energy range from infrared to visible light [32]. Since their optical reflectance spectroscopy is less sensitive to surface imperfections a good agreement with the bulk properties was found, implying a true half-metallic character of the material.

**Electronic correlations.** A third aspect that can have a negative influence on the half-metallic properties are electronic correlations. The influence of strong elec-

tronic correlations was investigated by CHIONCEL *et al.* for the compound FeMnSb using dynamic mean field theory (DMFT) [33]. They observed the formation of minority spin states with a vanishing quasiparticle weight, so called non-quasiparticle (NQP) states. Those NQP states reduce the spin polarization at the Fermi level. A similar analysis for the metal oxides CrO<sub>2</sub> and Fe<sub>3</sub>O<sub>4</sub> showed that NQP states were also found in these metal oxides, and that they indeed play a role for depolarization effects in half-metals [34, 35]. For the half-Heusler compound NiMnSb the influence of electronic correlations was studied by ALLMAIER *et al.* who used a combined density functional and many-body approach, where the many-body problem was solved with the Variational Cluster Approach [36], and by CHIONCEL *et al.* with LDA+DMFT [37]. Similar to the previously mentioned FeMnSb, also here NQP states were found to diminish the spin polarization at the Fermi level, which possibly provides an explanation for the low spin polarization measured in PCAR experiments. However, as pointed out by BORCA *et al.* after observing a high polarization value in their spin polarized inverse photoemission data at room temperature, the effect of these NQP states are, at least for NiMnSb, quite small [38].

**NiMnSb.** Experimental methods that are less sensitive to surface effects lead to different results. A famous experiment, for example, was carried out by HANSEN *et al.* who examined the electronic properties of a NiMnSb single crystal using positron annihilation technique [39]. In that experiment half-metallicity could be confirmed with an accuracy of roughly 0.01 *e* per formula unit. The gap width for the minority spin channel was measured by KIRILLOVA *et al.* to be around 0.4 eV, which is even smaller than most theoretical predictions [40]. Another successful experiment was done by HORDEQUIN *et al.* [41] who used polarized neutron diffraction on NiMnSb and found a spin polarization close to 95%. In an experiment with inelastic neutron scattering they observed a transition in the magnetic behaviour from a half-metal to a normal ferromagnet at about 80 K [42].

This phase transition was further investigated by BORCA *et al.* using magnetic circular dichroism measurements and spin-polarized inverse photoemission [43]. Below this transition temperature a dramatic increase of the magnetic moment in Mn and Ni occurs. Even though they found almost 100% spin polarization in the center of the Brillouin zone at room temperature, they pointed out that techniques that do not provide a sufficient *k*-sampling are unsuited for determining half-metallicity. Although there is a phase transition at 80 K, for lower temperatures a wide set of experiments such as elastic and inelastic neutron scattering, static magnetic measurements, magnetoresistance, Hall effect, thermopower and ferromagnetic resonance all hint towards a fully spin polarized conduction band [44].

Another interesting feature of NiMnSb is its half-metallic stability with respect to strain. It was calculated by GALANAKIS *et al.* that NiMnSb remains half-metallic for lattice dilations and contractions for up to 2% of the experimental lattice parameter [45].

**Transport.** The half-metallicity of Heusler alloys makes them a very promising material family for possible application in spintronic devices. With that in mind, the transport properties of Heusler alloys have always been a hot topic. For the full-Heusler alloy  $\text{Co}_2\text{TiSn}$  the transport properties were investigated by MAJUMDAR *et al.* who found some unexpected features [46]. At a temperature of 350 K they observed a transition from a semiconductor to a metal which is also associated with a transition from a paramagnetic to a ferromagnetic state. The metallic behavior below the transition temperature is presented as consistent with the predicted half-metallicity of the compound. Measurements of the transport properties of NiMnSb were done by OTTO *et al.* who analysed the anomalous Hall effect and the electrical resistivity [47]. An estimation of the contributions of side-jumps and skew scattering of the anomalous Hall effect was possible due the known conduction electron spin polarization at low temperatures. The magnetotransport properties of NiMnSb which was deposited onto heater Si using flash evaporation technique was discussed by AHN TUAN *et al* [48]. A negative magnetoresistance was found and assigned to grain-grain boundaries inside the polycrystalline structure.

Transport measurements were also carried out by GARDELIS *et al.* who grew polycrystalline NiMnSb onto single crystals of InSb [49]. For low temperatures around 5 K they found a saturation magnetization of  $4 \mu_B$  per formula unit, as expected for this half-metal, and a resistivity of  $6 \mu\Omega\text{cm}$ . At room temperature the resistivity was found to be about  $20 \mu\Omega\text{cm}$ . Regarding the possible usage of NiMnSb in magnetoresistance devices, a heterostructure of NiMnSb and silver was analysed by WEN *et al.* with special emphasis on the current-perpendicular-to-plane giant magnetoresistance (CPP-GMR) ratio [50]. This quantity, which is determined by the resistivities of the heterostructure for parallel and antiparallel arrangement of the magnetizations, was measured to be 21% at 4.2 K, and about 8% for room temperature. These small values are surprising since indications were found for a robust bulk half-metallicity against thermal fluctuations. The reason for the deviation of the expected high CPP-GMR ratio was attributed to interface effects between the Heusler alloy and the Ag spacer layer.

ZOU *et al.* investigated the transport properties of polycrystalline NiMnSb films with oxidized grain surfaces [51]. The Heusler alloy was grown onto a Si substrate via pulsed-laser deposition technique in an oxygen atmosphere which led to  $\text{MnO}_x$  layers at the grain boundaries. These intergrain interfaces have a huge impact on the resistivity, which is much higher for the thin films than for the NiMnSb target that has no  $\text{MnO}_x$  grain boundaries.

**Thin films.** Thin films of half metals have been an interesting topic for the past three decades. In the early 1990's KABANI *et al.* measured the magnetic properties of NiMnSb films and found a magnetization and Kerr rotation similar to the bulk [52]. No significant spin polarization in the magnetic Heusler layer was found in a tunnel junction of the form NiMnSb/MgO/Al at 0.4 K, where Al is superconductive and the Zeeman-splitting of the quasiparticle density of states causes a spin polar-

ization [53]. An interesting observation was that the resistivity for low temperatures drops in a linear fashion, rather than by a  $T^2$  law like for normal ferromagnets such as Fe, Ni and Co [54]. Resistivity measurements of thin films of this material and especially comparisons with the bulk are very difficult as described in the work of GIAPINTZAKIS *et al.* who grew NiMnSb at (relatively) low temperatures using pulsed-laser deposition [55]. They found that the transport properties of thin films are consistent with the NiMnSb crystal that was used as target. This feature was attributed to the fact that the target as well as the grown film had a huge amount of structural disorder. The quality of the target in deposition techniques and other procedural parameters may have a strong influence on the transport properties of thin films. This is supported by the work of CABALLERO *et al.* for CPP-MR measurements on the spin valve structure NiMnSb/Cu/NiMnSb/FeMn [56]. One result was that the deposition temperature of the Cu spacer layer has a significant influence on the GMR due to variations in the atomic disorder at the interfaces.

The application of NiMnSb in spintronic devices was discussed by HARRIS *et al.* who examined chemical disorder at the surface of a single crystal [57]. An extended X-ray absorption fine structure (EXAFS) analysis yielded Ni-Mn short range disorder at the interface which is an explanation for the often measured low spin polarization. On the other hand, a possible usage of NiMnSb was proposed by GARDELIS *et al.* who grew polycrystalline NiMnSb films on a single crystal InSb substrate [58]. An important feature regarding possible applications was the low coercive field since it defines the operating field range of active devices. The manipulation of magnetic moments is a key property in spintronic devices. A room-temperature spin-orbit torque in NiMnSb was found by CICCARELLI *et al.* [59].

**Spintronic devices.** The importance of Heusler alloys for the field of spintronic devices was pointed out by SAKURABA *et al.* who measured the tunneling magnetoresistance of  $\text{Co}_2\text{MnSi}$  with an amorphous aluminium oxide spacer layer [60]. They found values for the tunneling magnetoresistance ratio (TMR) well above 500%, which was the highest ever reported for an amorphous Al-O barrier. A possible application of Heusler alloys for field programmable gate arrays was proposed by THOMAS *et al.* [61], who presented a logic gate using  $\text{Co}_2\text{FeSi}/\text{AlO}_x/\text{Co}_{70}\text{Fe}_{30}$  tunnel junctions.

Other cobalt based full-Heusler alloys have also been investigated for their applicability in spintronic devices such as  $\text{Co}_2\text{FeAl}_{0.5}\text{Si}_{0.5}$  by WANG *et al.* [62]. They found that a MgO substrate can lead to highly ordered thin films with small surface roughness after post-deposition annealing. The in-plane magnetic anisotropy found in that material makes it a suitable material for heterostructures in spintronic devices. A nice collection of Co based Heusler alloys and the progress regarding spintronics can be found in the review article by GRAF *et al.* [63].

**Nanoparticles.** Nanoparticles of Heusler alloys are also promising candidates for spintronic devices. A detailed collection of the literature about these nanoparticles can be found in the review article of WANG *et al.* [64]. The advantages and

disadvantages of polycrystalline thin films of Heusler alloys versus epitaxially grown Heusler alloys were investigated by HIROHATA *et al.* [65]. They found that the activation diameter is much larger for polycrystalline films, which makes them suitable for read heads in spin transfer torque memory devices. Further information about the application of Heusler alloys in the field of spintronics is given by CASPER *et al.* [66], where special emphasis is put on the tunability of the band gap by interchanging atomic species.

As we can see, Heusler alloys have been intensively investigated for their applicability in various devices. This is where this thesis ties on, as we are interested in the influence of interfaces and lattice defects on the transmission coefficient and the on the spin polarization of the current. These questions are particularly relevant when it comes to creating actual devices, because interfaces with other materials always appear and because the growth process will most likely incorporate lattice defects to some degree. The functionality of the material, i.e., the spin polarization of the current must therefore be robust against those effects. If that is the case shall be answered within the framework of density functional theory (DFT) and non-equilibrium Green's function (NEGF) transport theory.

## Outline of the thesis

In the next two chapters, a short introduction in DFT and NEGF is given. The goal of these chapters is to provide a step-by-step derivation of the most important equations of the respective theories.

In the fourth chapter we will introduce the Kronig-Penney model, a very simple model for a one-dimensional crystal that results in multiple energy bands which we use to mimic a half-metallic material. This toy model is then used to calculate transmission coefficients, which can be compared with the results of the NEGF calculation.

Chapter 5 gives an introduction to the material and its structural and electric bulk properties. The lattice constant that is used throughout the rest of this thesis is calculated within the frame of DFT by minimizing the total energy. Furthermore the transport setup will be defined and explained.

In chapter 6 the transport properties without lattice defects will be investigated. We will consider up to four layers of NiMnSb and also include different methods of interface relaxation.

Chapter 7 then includes lattice defects in the transport calculations. This inclusion is restricted to two different defects, namely a vacancy at a Ni site and a swapping of a Ni with a Mn atom. For the latter also a distinction of the position of the defect is made.

In the last chapter a conclusion of the previous results is drawn. We will also compare our results with recent research including electronic correlations within the frame of dynamical mean-field theory.

# 2 Basics of Density Functional Theory

## Contents

---

<b>2.1</b>	<b>The Hohenberg-Kohn Theorem . . . . .</b>	<b>9</b>
<b>2.2</b>	<b>The Kohn-Sham Equations . . . . .</b>	<b>13</b>
<b>2.3</b>	<b>Exchange Correlation Functional . . . . .</b>	<b>21</b>
<b>2.4</b>	<b>The SIESTA Code . . . . .</b>	<b>22</b>
<b>2.5</b>	<b>Pseudopotentials . . . . .</b>	<b>23</b>

---

Density Functional Theory (DFT) was first developed in 1964 by WALTER KOHN and PIERRE HOHENBERG [67] and was finally rewarded in 1998 with the Nobel Prize in chemistry for WALTER KOHN. The cornerstone of Density Functional Theory is the fact that the ground state energy of a given many-electron system depends solely on the charge density. Therefore the ground state energy is a unique functional of the charge density as it was shown in the Hohenberg-Kohn theorem.

## 2.1 The Hohenberg-Kohn Theorem

The Hohenberg-Kohn theorem consists of two parts which form the mathematical basis of the DFT. The first theorem states that the ground state energy is a unique functional of the electron density. This means that two different potentials never lead to the same ground state of an electron system. The second theorem states that the true ground-state energy is the minimum value of the energy functional.

[67] “There exists a unique functional of the  $F[n(\mathbf{r})]$ , independent of  $V^{\text{ext}}(\mathbf{r})$ , such that  $E = \int V^{\text{ext}}(\mathbf{r})n(\mathbf{r})d^3r + F[n(\mathbf{r})]$  has as its minimum value the correct ground state energy associated with  $V^{\text{ext}}(\mathbf{r})$ .”

The first part of the theorem, the existence of  $E$  as a functional of  $n$ , is proved by *reductio ad absurdum*:

*Proof:* Let us assume that two different external potentials  $\hat{V}_1$  and  $\hat{V}_2$  with two different nondegenerate ground states  $|\Psi_1\rangle$  and  $|\Psi_2\rangle$  lead to the same electron density  $n(\mathbf{r})$ . Since  $|\Psi_1\rangle$  is the ground state of the Hamiltonian  $\hat{H}_1$  it is clear

that the expectation value of  $\hat{H}_1$  in the state  $|\Psi_2\rangle$  leads to a larger energy value:

$$E_1 = \langle \Psi_1 | \hat{H}_1 | \Psi_1 \rangle < \langle \Psi_2 | \hat{H}_1 | \Psi_2 \rangle. \quad (2.1)$$

Since both Hamiltonians differ only by the potentials  $\hat{V}_i$  we can write  $\hat{H}_1$  in dependence of  $\hat{H}_2$  and the potentials:

$$\hat{H}_1 = \hat{H}_2 + \hat{V}_1 - \hat{V}_2. \quad (2.2)$$

Because  $E_2 = \langle \Psi_2 | \hat{H}_2 | \Psi_2 \rangle$  Eq. (2.1) can be written as follows

$$E_1 < E_2 + \langle \Psi_2 | (\hat{V}_1 - \hat{V}_2) | \Psi_2 \rangle. \quad (2.3)$$

Since the whole argumentation can be done vice versa, it is valid to change the indices of this equation:

$$E_2 < E_1 + \langle \Psi_1 | (\hat{V}_2 - \hat{V}_1) | \Psi_1 \rangle. \quad (2.4)$$

In order to evaluate the expectation values on the right hand sides of Eq. (2.3) and (2.4) we need to insert unity matrices. In the following this is demonstrated with a single-particle Hamiltonian for simplicity's sake. The calculation for a many-body Hamiltonian yields the same result.

$$\begin{aligned} \langle \Psi_1 | (\hat{V}_2 - \hat{V}_1) | \Psi_1 \rangle &= \iint \langle \Psi_1 | \mathbf{r}' \rangle \langle \mathbf{r}' | (\hat{V}_2 - \hat{V}_1) | \mathbf{r} \rangle \langle \mathbf{r} | \Psi_1 \rangle d^3 r' d^3 r \\ &= \iint \langle \Psi_1 | \mathbf{r}' \rangle (V_2(\mathbf{r}) - V_1(\mathbf{r})) \delta(\mathbf{r} - \mathbf{r}') \langle \mathbf{r} | \Psi_1 \rangle d^3 r' d^3 r \\ &= \int (V_2(\mathbf{r}) - V_1(\mathbf{r})) \Psi_1^*(\mathbf{r}) \Psi_1(\mathbf{r}) d^3 r \\ &= \int (V_2(\mathbf{r}) - V_1(\mathbf{r})) n(\mathbf{r}) d^3 r \end{aligned} \quad (2.5)$$

Since the assumption was that both densities are the same ( $\Psi_1^* \Psi_1 = \Psi_2^* \Psi_2$ ), the first expectation value can be written analogical to the previous one,

$$\langle \Psi_2 | (\hat{V}_1 - \hat{V}_2) | \Psi_2 \rangle = \int (V_1(\mathbf{r}) - V_2(\mathbf{r})) n(\mathbf{r}) d^3 r. \quad (2.6)$$

Now Eq. (2.3) and (2.4) can be added, so that the expectation values on the right hand side annihilate each other:

$$E_1 + E_2 < E_1 + E_2 \quad (2.7)$$

This is obviously wrong, which means that the assumption was also wrong.

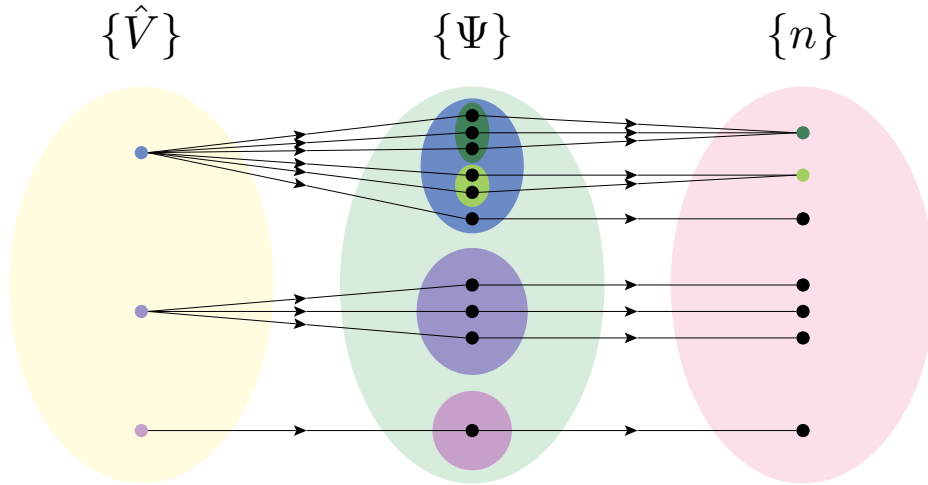


Figure 2.1: Visualization of the Hohenberg-Kohn theorem. A single potential may lead to different wave functions that can give rise to the same electron density, but two different potentials can never result in the same density. Picture originally published in the book “Quantum theory of the electron liquid” [68].

What was proved here, was in fact that the function  $V^{\text{ext}} \mapsto n$  is injective. This means that for all electron densities  $n$  in the image of this function (they are called *v-representable* because they are created by an external potential), the inverse function  $n \mapsto V^{\text{ext}}$  also exists. And since  $V^{\text{ext}}$  uniquely determines the Hamiltonian, which determines the ground state, we can say that the ground state  $|\Psi[n]\rangle$  is uniquely specified by the electron density  $n$ . The ground state energy is therefore itself a functional of  $n$ . This proves the first part of the Hohenberg-Kohn theorem.

To prove the second part of the theorem, that the minimum of the functional  $E[n]$  equals the real ground state energy, we need to split up the Hamiltonian:

$$H = V^{\text{ext}} + T + U, \quad (2.8)$$

where  $T$  is the kinetic energy,  $U$  is the interaction of the electrons and  $V^{\text{ext}}$  is the external potential. Let  $n_0$  be the ground state density of the Hamiltonian  $H$ . The vector  $|\Psi[n]\rangle$  is then the ground state for a different Hamiltonian, determined by

the *v-representable* density  $n$ . The functional,

$$\begin{aligned}
 E[n] &= \langle \Psi[n] | (V^{\text{ext}} + T + U) | \Psi[n] \rangle \\
 &= \int V^{\text{ext}}(\mathbf{r})n(\mathbf{r})d^3r + \langle \Psi[n] | (T + U) | \Psi[n] \rangle \\
 &= \int V^{\text{ext}}(\mathbf{r})n(\mathbf{r})d^3r + F[n],
 \end{aligned} \tag{2.9}$$

can therefore only be minimized by the true ground state density  $n_0$ . The resulting energy value is therefore the true ground state energy, thus proving the second part of the theorem.

Another formalism to find the ground state energy is the constrained search formalism described by LEVY [69]. In this formalism the Rayleigh-Ritz principle of finding the ground state energy of a given Hamiltonian via variation of the wave function

$$E_0 = \min_{\Psi} \langle \Psi | H | \Psi \rangle, \tag{2.10}$$

where the wave function must be antisymmetric and must satisfy certain boundary conditions, is split up into two steps. In the first step the minimization is done over a certain set of wave functions that all yield the same density  $n(\mathbf{r})$  and in the second step the energy is minimized via the densities.

$$\begin{aligned}
 E_0 &= \min_{\Psi} \langle \Psi | \hat{H} | \Psi \rangle \\
 &= \min_{n(\mathbf{r})} \min_{\Psi \rightarrow n(\mathbf{r})} \langle \Psi | \hat{T} + \hat{U} + \hat{V}^{\text{ext}} | \Psi \rangle \\
 &= \min_{n(\mathbf{r})} \min_{\Psi \rightarrow n(\mathbf{r})} \left[ \langle \Psi | \hat{T} + \hat{U} | \Psi \rangle + \langle \Psi | \hat{V}^{\text{ext}} | \Psi \rangle \right] \\
 &= \min_{n(\mathbf{r})} \left[ F[n] + \int n(\mathbf{r})V^{\text{ext}}(\mathbf{r})d^3r \right]
 \end{aligned} \tag{2.11}$$

For the case that the density  $n(\mathbf{r})$  is *v-representable*, the functional  $F[n]$  is the universal functional which is mentioned in the quote of HOHENBERG and KOHN and is valid for any number of electrons and any external potential. Unfortunately  $F[n]$  is unknown. The great advantage is that the density in this formalism does not have to be *v-representable*. This is, in theory, important because it cannot be guaranteed that if a certain density is *v-representable*, a small variation of that density  $n(\mathbf{r}) + \delta n(\mathbf{r})$  is also *v-representable*. In reality, however, this does not matter since, as we will see in the next section, the used densities are by construction always *v-representable*. Nevertheless the LEVY formulation shows in an esthetic way that the ground state energy is the minimum of the cited functional.

## 2.2 The Kohn-Sham Equations

We learned in the previous above that DFT relies on a functional  $F[n]$ , whose explicit form is unknown. Today's most common way to deal with this unknown functional was developed by WALTER KOHN and LU JEU SHAM in 1965 [70]. Their approach was to replace the interacting electron system by a non-interacting system, which is assumed to have the same density  $n(\mathbf{r})$  as the interacting one. This non-interacting system is in an effective potential  $V^{\text{eff}}$ . The first step is to divide the ground state energy functional into four parts.

$$E[n] = T_s[n] + E_H[n] + E_{XC}[n] + \int n(\mathbf{r})V^{\text{ext}}(\mathbf{r})d^3r \quad (2.12)$$

Here,  $T_s[n]$  is the kinetic energy of a non-interacting electron system,  $E_H[n]$  is the Hartree contribution of the electron-electron interaction,  $E_{XC}[n]$  is the so called exchange-correlation functional which contains contributions that go beyond the Hartree approximation, and lastly the integral that is the functional for the external potential. The sum of the first three functionals is the universal functional  $F[n]$  from the Hohenberg-Kohn theorem.

The kinetic energy functional can be written as follows.

$$T_s[n] = \min_{\Psi \rightarrow n(\mathbf{r})} \langle \Psi | \sum_{i=1}^N \frac{\hat{P}_i^2}{2m_e} | \Psi \rangle \quad (2.13)$$

This is an application of the previously mentioned constrained search algorithm since the variation has to be done in two steps. The Hartree contribution to the electron-electron is defined as

$$E_H[n] = \frac{e^2}{2} \iint \frac{n(\mathbf{r})n(\mathbf{r}')}{|\mathbf{r} - \mathbf{r}'|} d^3r' d^3r. \quad (2.14)$$

The exact form of the exchange correlation functional is unknown and has to be approximated. The idea is to replace something unknown (the universal function  $F[n]$ ) by something known ( $T_s[n]$  and  $E_H[n]$ ) plus something unknown ( $E_{XC}[n]$ ) in order to create a self-consistent formalism. Since the derivation of the self-consistent equations in the original paper of KOHN and SHAM is kept very brief, a more detailed description shall be given in the following paragraph.

First, we take the functional for the kinetic energy as given in Eq. (2.13) and insert unity matrices in the many-body real-space basis at both sides of the energy operator, thus going from the DIRAC notation in Eq. 2.13 to wave functions and from abstract operators to their real-space representation.

$$T_s[n] = \min_{\Psi \rightarrow n} \int \Psi^*(\mathbf{r}_1, \dots, \mathbf{r}_N) \left( - \sum_{i=1}^N \frac{\hbar^2}{2m_e} \nabla_i^2 \right) \Psi(\mathbf{r}_1, \dots, \mathbf{r}_N) d^3r_1 \dots d^3r_N \quad (2.15)$$

In the next step, we utilize that the wave functions of non-interacting electron systems can always be represented as Slater determinants, which means they can be written in the following way:

$$\Psi(\mathbf{r}_1, \dots, \mathbf{r}_N) = \frac{1}{\sqrt{N!}} \det \begin{pmatrix} \phi_1(\mathbf{r}_1) & \phi_2(\mathbf{r}_1) & \cdots & \phi_N(\mathbf{r}_1) \\ \phi_1(\mathbf{r}_2) & \phi_2(\mathbf{r}_2) & \cdots & \phi_N(\mathbf{r}_2) \\ \vdots & \vdots & \ddots & \vdots \\ \phi_1(\mathbf{r}_N) & \phi_2(\mathbf{r}_N) & \cdots & \phi_N(\mathbf{r}_N) \end{pmatrix}. \quad (2.16)$$

Now let us assume that the single-particle wave functions  $\phi_i$  are orthonormalized which means that the following integral rule holds for each pair of them:

$$\int \phi_i^*(\mathbf{r}) \phi_j(\mathbf{r}) d^3r = \delta_{ij}. \quad (2.17)$$

What happens if the Slater determinant is inserted into Eq. (2.15) shall be explained in a small example of a two-electron wave function, which according to Eq. (2.16) looks like this:

$$\Psi(\mathbf{r}_1, \mathbf{r}_2) = \frac{1}{\sqrt{2}} \left( \phi_1(\mathbf{r}_1) \phi_2(\mathbf{r}_2) - \phi_1(\mathbf{r}_2) \phi_2(\mathbf{r}_1) \right). \quad (2.18)$$

If we now evaluate only one part of the integrand, namely  $\Psi^* \nabla_1^2 \Psi$  we get the following expression:

$$\begin{aligned} \Psi^*(\mathbf{r}_1, \mathbf{r}_2) \nabla_1^2 \Psi(\mathbf{r}_1, \mathbf{r}_2) = \frac{1}{2} \left[ \phi_2^*(\mathbf{r}_2) \phi_2(\mathbf{r}_2) \phi_1^*(\mathbf{r}_1) \nabla_1^2 \phi_1(\mathbf{r}_1) + \right. \\ \phi_1^*(\mathbf{r}_2) \phi_1(\mathbf{r}_2) \phi_2^*(\mathbf{r}_1) \nabla_1^2 \phi_2(\mathbf{r}_1) - \\ \phi_1^*(\mathbf{r}_2) \phi_2(\mathbf{r}_2) \phi_1^*(\mathbf{r}_1) \nabla_1^2 \phi_2(\mathbf{r}_1) - \\ \left. \phi_2^*(\mathbf{r}_2) \phi_1(\mathbf{r}_2) \phi_2^*(\mathbf{r}_1) \nabla_1^2 \phi_1(\mathbf{r}_1) \right] \quad (2.19) \end{aligned}$$

When the terms in **blue** color are integrated over  $\mathbf{r}_2$ , they become 1 due to the normalization of the single-particle wave functions. The **red** colored terms on the other side vanish when integrated due to the orthogonality that was assumed. If we now add the second term with the nabla operator  $\nabla_2$  for the second coordinate  $\mathbf{r}_2$  and integrate over both coordinates we get

$$\begin{aligned} \iint \Psi^*(\mathbf{r}_1, \mathbf{r}_2) \left( \nabla_1^2 + \nabla_2^2 \right) \Psi(\mathbf{r}_1, \mathbf{r}_2) d^3r_1 d^3r_2 = \frac{1}{2} \int \phi_1^*(\mathbf{r}_1) \nabla_1^2 \phi_1(\mathbf{r}_1) d^3r_1 + \\ \frac{1}{2} \int \phi_1^*(\mathbf{r}_2) \nabla_2^2 \phi_1(\mathbf{r}_2) d^3r_2 + \\ \frac{1}{2} \int \phi_2^*(\mathbf{r}_1) \nabla_1^2 \phi_2(\mathbf{r}_1) d^3r_1 + \\ \frac{1}{2} \int \phi_2^*(\mathbf{r}_2) \nabla_2^2 \phi_2(\mathbf{r}_2) d^3r_2. \quad (2.20) \end{aligned}$$

Since now the integrals on the right side are separated, we can rename the variables  $\mathbf{r}_1, \mathbf{r}_2 \rightarrow \mathbf{r}$  and add up the integrals pairwise. The first two and the second two integrals are equivalent, which means the factors of  $\frac{1}{2}$  add up to 1. For the general case of  $N$  particles the Slater determinant would consist of  $N!$  terms, of which each is a product of  $N$  single-particle wave functions. The prefactors would thus be  $\frac{1}{N!}$ . If we then write down the object  $\Psi^* \nabla_1^2 \Psi$  according to Eq. (2.19), we would get  $(N!)^2$  terms. Each of these terms again contains a factor with the nabla operator and the wave functions with the coordinate  $\mathbf{r}_1$  and also  $N - 1$  pairs of wave functions, that are either of the **blue** or of the **red** type. When the integration over all coordinates is performed, from all those  $(N!)^2$  terms only the ones that contain solely **blue** pairs of wave functions survive. According to the rules of combinatorics there are  $N!$  of these terms. These  $N!$  terms can be ordered according to the index of the wave functions that depend on  $\mathbf{r}_1$  which gives  $N$  groups consisting of  $(N - 1)!$  terms (just like in Eq. (2.19)). This means that the integration over all  $N$  terms of the form  $\Psi \nabla_i \Psi$  leads to  $N \cdot (N - 1)! = N!$  terms per group which cancels out with the prefactor so that they all add up to 1. With that in mind we can abridge Eq. (2.15) to the following form:

$$T_s[n] = \min_{\{\phi_i\} \rightarrow n} \left\{ -\frac{\hbar^2}{2m_e} \sum_{i=1}^N \int \phi_i^*(\mathbf{r}) \nabla^2 \phi_i(\mathbf{r}) d^3r \right\}. \quad (2.21)$$

The constraint that the set of single particle wave functions yields the density  $n$  has to be understood in the sense that the sum of the squared absolute values of these wave functions is the density in question,

$$n(\mathbf{r}) = \sum_{i=1}^N \phi_i^*(\mathbf{r}) \phi_i(\mathbf{r}). \quad (2.22)$$

For the Hartree energy functional, we can replace the density  $n$  with its definition according to Eq. (2.22), which leads to

$$E_H[n] = \frac{e^2}{2} \iint \frac{\left( \sum_i \phi_i^*(\mathbf{r}) \phi_i(\mathbf{r}) \right) \left( \sum_j \phi_j^*(\mathbf{r}') \phi_j(\mathbf{r}') \right)}{|\mathbf{r} - \mathbf{r}'|} d^3r' d^3r. \quad (2.23)$$

For the exchange correlation functional in Eq. (2.12) we assume, for simplicity, an integral representation like

$$E_{XC}[n] = \int \varepsilon_{XC}(n(\mathbf{r})) n(\mathbf{r}) d^3r, \quad (2.24)$$

where  $\varepsilon_{XC}$  is a not specified function which is requested to be differentiable. We can now replace the density  $n$  at the right hand side of the previous equation with the definition from Eq. (2.22) and finally get

$$E_{XC}[n] = \int \varepsilon_{XC} \left( \sum_i \phi_i^*(\mathbf{r}) \phi_i(\mathbf{r}) \right) \sum_j \phi_j^*(\mathbf{r}) \phi_j(\mathbf{r}) d^3r. \quad (2.25)$$

The functional of the external potential has to be treated in the same manner, which leads to the form

$$\int V^{\text{ext}}(\mathbf{r}) \sum_i \phi_i^*(\mathbf{r}) \phi_i(\mathbf{r}) d^3r. \quad (2.26)$$

The sense in all of the work so far was to transform the variational problem from a variation of the density to a variation of the single-particle wave functions. This was necessary because the functional for the kinetic energy cannot be formulated in a way that only uses the electron density. Now all the functionals are of the same form because only the single particle wave functions appear, for which we now have to perform the variational calculus. In the following, we want to minimize the ground state energy functional with respect to the complex conjugated **first** single-particle wave function  $\phi_1^*(\mathbf{r})$ . By doing so we get an equation for the single-particle wave functions. A minimization with respect to the non-conjugated wave functions would lead to an equation for the complex conjugated wave functions. In order to perform the minimization, we must replace  $\phi_1^*(\mathbf{r})$  with  $\phi_1^*(\mathbf{r}) + \varepsilon \eta^*(\mathbf{r})$  wherever it appears. Here,  $\eta^*(\mathbf{r})$  is a perturbation function and  $\varepsilon$  is a small parameter. This replacement changes the electron density  $n(\mathbf{r})$  to  $n_\varepsilon(\mathbf{r})$ , which is defined by

$$n_\varepsilon(\mathbf{r}) = n(\mathbf{r}) + \varepsilon \eta^*(\mathbf{r}) \phi_1(\mathbf{r}). \quad (2.27)$$

According to the variational principle, the functional becomes extremal when the derivative of the functional with respect to the parameter  $\varepsilon$  vanishes at  $\varepsilon = 0$ . For the functional of the kinetic energy as in Eq. (2.21), only one term in the sum contains an  $\varepsilon$  so that the differentiation is easily done:

$$\left. \frac{d}{d\varepsilon} T_s[n_\varepsilon] \right|_{\varepsilon=0} = -\frac{\hbar^2}{2m_e} \int \eta^*(\mathbf{r}) \nabla^2 \phi_1(\mathbf{r}) d^3r \quad (2.28)$$

If we do the same for the Hartree energy functional, the product of the two electron densities transforms according to

$$\begin{aligned} n(\mathbf{r})n(\mathbf{r}') &\rightarrow n(\mathbf{r})n(\mathbf{r}') + \varepsilon^2 \eta^*(\mathbf{r})\eta^*(\mathbf{r}')\phi_1(\mathbf{r})\phi_1(\mathbf{r}') + \\ &\varepsilon \eta^*(\mathbf{r}')n(\mathbf{r})\phi_1(\mathbf{r}') + \varepsilon \eta^*(\mathbf{r})n(\mathbf{r}')\phi_1(\mathbf{r}). \end{aligned} \quad (2.29)$$

The first term vanishes during the differentiation with respect to  $\varepsilon$  and the second term vanishes when  $\varepsilon$  is set to zero in the derivative. The last two terms on the right side survive this process. The integral in Eq. (2.14) can now be split up into two identical parts, that can be simply added up:

$$\begin{aligned} \left. \frac{d}{d\varepsilon} E_H[n_\varepsilon] \right|_{\varepsilon=0} &= \frac{e^2}{2} \iint \frac{\eta^*(\mathbf{r}')n(\mathbf{r})\phi_1(\mathbf{r}')}{|\mathbf{r} - \mathbf{r}'|} d^3r' d^3r + \\ &\frac{e^2}{2} \iint \frac{\eta^*(\mathbf{r})n(\mathbf{r}')\phi_1(\mathbf{r})}{|\mathbf{r} - \mathbf{r}'|} d^3r' d^3r \\ &= e^2 \int \eta^*(\mathbf{r}) \int \frac{n(\mathbf{r}')}{|\mathbf{r} - \mathbf{r}'|} d^3r' \phi_1(\mathbf{r}) d^3r. \end{aligned} \quad (2.30)$$

The integral that is the functional of the external potential transforms to

$$\int \eta^*(\mathbf{r}) V^{\text{ext}}(\mathbf{r}) \phi_1(\mathbf{r}) d^3r. \quad (2.31)$$

For the exchange correlation functional we need the differentiability of the function  $\varepsilon_{XC}(n)$  in order to perform the differentiation with respect to  $\varepsilon$  via chain rule,

$$\frac{d}{d\varepsilon} E_{XC} \Big|_{\varepsilon=0} = \int \eta^*(\mathbf{r}) V_{XC}(n(\mathbf{r})) \phi_1(\mathbf{r}) d^3r, \quad (2.32)$$

where  $V_{XC}$  is the so called exchange-correlation potential, which is defined as follows:

$$V_{XC}(n) = \varepsilon_{XC}(n) + \frac{d\varepsilon_{XC}(n)}{dn} n. \quad (2.33)$$

One last aspect which has to be taken into account before we proceed to the Kohn-Sham equations is to make sure that the single-particle wave functions are indeed orthonormal, since many steps in the previous calculations were only possible under that assumption. In order to make sure that this assumption is justified we include the orthonormality as a constraint. This is done with Lagrange multipliers similar to classical mechanics, which means that the minimization problem is formally extended to

$$L[n, \lambda] = E[n] - \lambda G[n], \quad (2.34)$$

where  $G[n]$  is a functional that describes the constraint that is imposed on the system. Since we have  $N$  particles, we get  $N^2$  constraints which can be summarized as:

$$\sum_{i,j=1}^N \lambda_{ij} \left( \int \phi_i^*(\mathbf{r}) \phi_j(\mathbf{r}) d^3r - \delta_{ij} \right). \quad (2.35)$$

Of course we have to apply to these functionals the same procedure as for the other ones. After replacing  $\phi_1^*$  with  $\phi_1^* + \varepsilon \eta^*$ , calculating the derivative with respect to  $\varepsilon$  and finally setting  $\varepsilon = 0$  we get

$$\sum_{j=1}^N \lambda_{1j} \int \eta^*(\mathbf{r}) \phi_j(\mathbf{r}) d^3r. \quad (2.36)$$

Now we have a set of functionals in an integral form, all of them containing a single  $\eta^*(\mathbf{r})$  function on the leftmost side of the integrand. We can finally write everything into one integral. Therefore, it is practical to define an effective potential

$$V^{\text{eff}}(\mathbf{r}) = V^{\text{ext}}(\mathbf{r}) + e^2 \int \frac{n(\mathbf{r}')}{|\mathbf{r} - \mathbf{r}'|} d^3r' + V_{XC}(n(\mathbf{r})) \quad (2.37)$$

With this abbreviation we can formulate the minimization condition, that is

$$\frac{d}{d\varepsilon} L[n_\varepsilon, \{\lambda_{ij}\}] \Big|_{\varepsilon=0} = 0, \quad (2.38)$$

in the following way:

$$\int \eta^*(\mathbf{r}) \left[ \left( -\frac{\hbar^2}{2m_e} \nabla^2 + V^{\text{eff}}(\mathbf{r}) \right) \phi_1(\mathbf{r}) - \sum_{j=1}^N \lambda_{1j} \phi_j(\mathbf{r}) \right] d^3r = 0. \quad (2.39)$$

Since the perturbation function  $\eta^*(\mathbf{r})$  is completely arbitrary but the integral has to vanish nevertheless, we conclude that the part in the brackets has to be zero,

$$\underbrace{\left( -\frac{\hbar^2}{2m_e} \nabla^2 + V^{\text{eff}}(\mathbf{r}) \right)}_{\hat{H}^{\text{eff}}} \phi_1(\mathbf{r}) - \sum_{j=1}^N \lambda_{1j} \phi_j(\mathbf{r}) = 0. \quad (2.40)$$

Here we define an effective Hamiltonian, consisting of the kinetic energy operator and the effective potential. So far we only minimized the ground state energy functional with respect to  $\phi_1^*(\mathbf{r})$ . In order to minimize the functional with respect to the whole density, we must repeat the previous calculations with all other complex conjugated single-particle wave functions. This is of course done in the very same manner, which means we get  $N - 1$  other equations of exactly the same form as Eq. (2.40). If one writes those  $N$  equations underneath each other, one can see that it is possible to write them as a vector equation,

$$\hat{H}^{\text{eff}} \underbrace{\begin{pmatrix} \phi_1(\mathbf{r}) \\ \phi_2(\mathbf{r}) \\ \vdots \\ \phi_N(\mathbf{r}) \end{pmatrix}}_{|\phi\rangle} - \underbrace{\begin{pmatrix} \lambda_{11} & \lambda_{12} & \cdots & \lambda_{1N} \\ \lambda_{21} & \lambda_{22} & \cdots & \lambda_{2N} \\ \vdots & \vdots & \ddots & \vdots \\ \lambda_{N1} & \lambda_{N2} & \cdots & \lambda_{NN} \end{pmatrix}}_{\Lambda} \underbrace{\begin{pmatrix} \phi_1(\mathbf{r}) \\ \phi_2(\mathbf{r}) \\ \vdots \\ \phi_N(\mathbf{r}) \end{pmatrix}}_{|\phi\rangle} = \begin{pmatrix} 0 \\ 0 \\ \vdots \\ 0 \end{pmatrix}. \quad (2.41)$$

In order to simplify the following steps it is practical to introduce the vector  $|\phi\rangle$ , which is a  $N$ -element column vector where each element is a single-particle wave function. This notation is admittedly quite uncommon, but useful nevertheless. The elegance of DIRAC'S bra-ket notation helps to explain what happens in the next steps without having to introduce abstract unitary transformations. The matrix  $\Lambda$  is defined by the  $N^2$  Lagrange multipliers which we used to formulate the constraints. In the following we are interested in the properties of this matrix  $\Lambda$ . Therefore we take Eq. (2.40) for the  $i$ -th particle, multiply it with  $\phi_k^*(\mathbf{r})$  from the left hand side and finally integrate over the volume,

$$\int \phi_k^*(\mathbf{r}) \hat{H}^{\text{eff}} \phi_i(\mathbf{r}) d^3r - \int \sum_{j=1}^N \lambda_{ij} \phi_k^*(\mathbf{r}) \phi_j(\mathbf{r}) d^3r = 0. \quad (2.42)$$

Since the single-particle wave functions must be orthonormal, only one term in the sum survives the integration, so that we finally get

$$\int \phi_k^*(\mathbf{r}) \hat{H}^{\text{eff}} \phi_i(\mathbf{r}) d^3r = \lambda_{ik}. \quad (2.43)$$

This can of course be done again with exchanged indexes, which leads to

$$\int \phi_i^*(\mathbf{r}) \hat{H}^{\text{eff}} \phi_k(\mathbf{r}) d^3r = \lambda_{ki}. \quad (2.44)$$

The effective Hamiltonian  $\hat{H}^{\text{eff}}$  is hermitian, which has an immediate effect on the Lagrange multipliers, as we can now write the identity

$$\lambda_{ik} = \lambda_{ki}^*. \quad (2.45)$$

For the matrix  $\Lambda$  this means that  $\Lambda$  is also hermitian and can therefore be diagonalized. This is formally done by

$$\Lambda = \sum_{j=1}^N \varepsilon_j |\varepsilon_j\rangle \langle \varepsilon_j|. \quad (2.46)$$

The vector  $|\varepsilon_j\rangle$  and its respective bra-vector are  $N$ -dimensional. Now we insert this decomposition into Eq. (2.41) and multiply it with the constant vector  $\langle \varepsilon_i|$  from the left. Since the effective Hamiltonian  $\hat{H}^{\text{eff}}$  acts as a scalar and thus does not affect the vector  $\langle \varepsilon_i|$ , we can write

$$\hat{H}^{\text{eff}} \langle \varepsilon_i | \phi \rangle = \varepsilon_i \langle \varepsilon_i | \phi \rangle. \quad (2.47)$$

The “scalar product”  $\langle \varepsilon_i | \phi \rangle$  is a linear combination of the single-particle wave functions that were introduced in the Slater determinant Eq. (2.16). This is because, according to the definition of the vector  $|\phi\rangle$ , its components are the single-particle wave functions  $\phi_i(\mathbf{r})$ . Thus, this “scalar product” can be identified as a wave function itself,

$$\langle \varepsilon_i | \phi \rangle = \psi_i(\mathbf{r}). \quad (2.48)$$

These wave functions are called the Kohn-Sham wave functions and solve the so called Kohn-Sham equations,

$$\left( -\frac{\hbar^2}{2m_e} \nabla^2 + V^{\text{eff}}(\mathbf{r}) \right) \psi_i(\mathbf{r}) = \varepsilon_i \psi_i(\mathbf{r}). \quad (2.49)$$

The electron density is of course the central quantity in DFT and therefore a crucial question is, if the density of the  $N$  Kohn-Sham wave functions is the same as the density of the single-particle wave functions from Eq. (2.16). Therefore, we calculate the electron density using the Kohn-Sham wave functions as follows:

$$n_{\text{KS}}(\mathbf{r}) = \sum_{j=1}^N \psi_j^*(\mathbf{r}) \psi_j(\mathbf{r}) = \sum_{j=1}^N \langle \phi | \varepsilon_j \rangle \langle \varepsilon_j | \phi \rangle = \langle \phi | \phi \rangle = \sum_{j=1}^N \phi_j^*(\mathbf{r}) \phi_j(\mathbf{r}) = n(\mathbf{r}) \quad (2.50)$$

As we can see the density obtained from the Kohn-Sham wave functions is indeed the same density as from the single-particle wave functions. The Kohn-Sham equations

have to be solved self-consistently because the electron density, which is calculated using the solutions of the equations, is also part of the equation itself. In the effective potential Eq. (2.37) of the Kohn-Sham equations the electron density appears in the Hartree term and also in the exchange-correlation potential.

The self-consistent loop is sketched in Fig. 2.2. One starts with an initial density  $n(\mathbf{r})$ . This density is then used to construct the effective potential  $V^{\text{eff}}(\mathbf{r})$  as in Eq. (2.37). This potential is also commonly referred to as Kohn-Sham potential  $V^{\text{KS}}(\mathbf{r})$ . Once the effective potential is constructed, the eigenfunctions of the Kohn-Sham Hamiltonian can be calculated according to Eq. (2.49). Among these eigenfunctions, the Kohn-Sham orbitals/wave functions, the ones with the  $N$  lowest eigenvalues are chosen to form the new density for the next iteration step. This is done according to Eq. (2.22). In many implementations of the self consistent loop the new density is mixed with the old density in a linear combination in order to ease the convergence:

$$n_{\text{in}}^{\text{new}}(\mathbf{r}) = \alpha n_{\text{out}}^{\text{old}}(\mathbf{r}) + (1 - \alpha) n_{\text{in}}^{\text{old}}(\mathbf{r}), \quad (2.51)$$

where  $\alpha$  is usually a small parameter. After the new density is obtained, the cycle restarts again with creating the effective potential. This goes on until some convergence condition is fulfilled, which means that the change of a specific value between two iteration steps is smaller than a previously defined accuracy parameter.

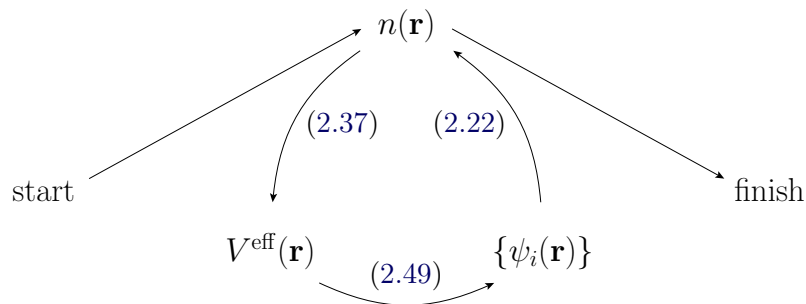


Figure 2.2: Sketch of the self-consistency loop of the Kohn-Sham scheme. An initial electron density is used to generate the effective potential, using Eq. (2.37), which determines the effective Hamiltonian. The eigenfunctions of the effective Hamiltonian, gathered from Eq. (2.49), are then used to calculate the density for the next iteration using Eq. (2.22).

## 2.3 Exchange Correlation Functional

The exchange-correlation functional (potential) is a critical point in density functional theory because its true form is unknown. The search for viable approximations has been an active field of research since 1960's. One of the earliest approximations was the local density approximation (LDA), which was also used in the derivation of the Kohn-Sham equations in the last section,

$$E_{XC}^{LDA}[n] = \int \varepsilon_{XC}^{LDA}(n(\mathbf{r})) n(\mathbf{r}) d^3r. \quad (2.52)$$

In this approximation, the functional is an integral that only depends only on the density. In its most basic formulation the unknown function in the integral is split into an exchange and a correlation part, where the known exchange energy density of a homogenous electron gas is used. For the correlation energy density several approximations exist. SIESTA allows for two different functionals in the LDA approximation, namely one by CEPERLEY and ALDER (CA) [71] and one by PERDEW and WANG (PW92) [72]. An extension of the LDA is the inclusion of spin polarization, which leads to the so called local spin density approximation (LSDA),

$$E_{XC}^{LSDA}[n_{\uparrow}, n_{\downarrow}] = \int \varepsilon_{XC}^{LSDA}[n_{\uparrow}(\mathbf{r}), n_{\downarrow}(\mathbf{r})] n(\mathbf{r}) d^3r. \quad (2.53)$$

However, mostly used in this thesis is another approximation that also incorporates gradients of the electron density. Functionals with this feature belong to the family of generalized gradient approximations (GGA), which can be described by the following formula:

$$E_{XC}^{GGA}[n_{\uparrow}, n_{\downarrow}] = \int \varepsilon_{XC}^{GGA}[n_{\uparrow}(\mathbf{r}), n_{\downarrow}(\mathbf{r}), \nabla n_{\uparrow}(\mathbf{r}), \nabla n_{\downarrow}(\mathbf{r})] n(\mathbf{r}) d^3r. \quad (2.54)$$

The GGA replaced the formerly suggested gradient expansion approximation (GEA) by using more general functions of the density and its gradients, instead of a series expansion. Due to the flexibility of these functionals, a specific tailoring of the calculation setup onto the concrete problem is possible. The specific functional used for most calculations in this thesis was proposed by PERDEW, BURKE and ERNZERHOF (PBE) [73]. Although there are revised versions available for this functional such as (revPBE) by ZHANG *et al.* [74] or (RPBE) by HAMMER *et al.* [75], the original version is still commonly used in the community and yields almost no changes in band structure and density of states. While LDA has a long success story regarding metals, it is well documented that its ability to describe semiconductors is limited. Since half-metallic Heusler alloys are semiconductors for at least one spin direction, the generalized gradient approximation is employed in the remainder of this thesis.

## 2.4 The SIESTA Code

For the DFT calculations in this thesis the SIESTA package was used. The name of the package is an acronym for **S**panish **I**nitiative for **E**lectronic **S**imulations with **T**housands of **A**toms. The program is free for academic purposes and comes with a variety of tools to analyse the received data. The method was originally proposed by SOLER *et al.* in 2002 and is used by a huge community, which is documented by over 7000 citations of the original paper [76].

A huge advantage of SIESTA is the reduction of computation time through the use of norm conserving pseudopotentials, which will be discussed in more detail in the next section. A wide set of well tested pseudopotentials is accessible on the SIESTA homepage, but the package also includes a tool, the *atom* program, which allows the users to create pseudopotentials themselves. This may be needed in special cases where the potentials have to be tailored manually to suit the user's needs.

The wave functions are comprised of a linear combination of (pseudo) atomic orbitals, which is useful for the chemical analysis of the output data, since the projected density of states and population numbers are easily accessible.

For the exchange correlation functional a wide range of local spin density or generalized gradient approximations are available. SIESTA is capable of calculating molecular dynamics and generalized forces, which is used to optimize the crystal structure of a periodic system as well as to relax the surface of a material or the interface of two materials. A great advantage of SIESTA is the flexibility with respect to the desired calculation type. For smaller systems an exact diagonalization method is available which produces accurate results, and larger systems can be treated with an order- $N$  algorithm, drastically reducing the computation time.

The so called Z-matrix formalism implemented in SIESTA allows for a structure optimization over a large range of constraints, for example, fixed angles or distances which is especially helpful if molecules are investigated. The usage of multiple- $\zeta$  spin polarized basis functions allows for a detailed magnetic analysis of considered structures. Also spin resolved population analyses for different atomic orbitals are available. This is particularly important for this thesis because of the complex magnetic structure of half-metallic ferromagnets.

SIESTA also comes with a considerable amount of auxiliary programs, such as, for example, *rho2xfs* which uses the density matrix and the eigenvectors of the Hamiltonian to calculate a spin resolved, space dependent, local density of states, a feature that is often used in this thesis. Also the flexible data format (fdf) of the input file makes it easy to automatize a large set of calculations via a simple shell script, which is useful for convergence tests with respect to a specific parameter, for example, the lattice constant. SIESTA has also interfaces with other programs like SMEAGOL for non-equilibrium transport properties. This interface was an important argument for choosing SIESTA as the DFT code that fits best for our purposes, since transport properties are the main aspect of this thesis.

## 2.5 Pseudopotentials

The pseudopotential approach allows for a drastic reduction of the computation time because the chemically inert core electrons are not a part of the minimization process anymore. Instead their potential is combined with the potential of the nucleus which suppresses divergences and removes the oscillations of the wave functions of the valence electrons, which originate in the orthogonality of all wave functions, of course including the ones for the core electrons. To illustrate what is meant by that, a sketch of the paper by PHILLIPS and KLEINMAN follows [77]. Let us consider a Hamiltonian  $\hat{H}$  with  $N$  core electrons which are described by core wave functions  $|\chi_n\rangle$  with the eigenvalues  $E_n$ . Now let us consider a valence electron wave function  $|\psi\rangle$  with an eigenvalue  $E$ . The pseudo wave function  $|\phi\rangle$  is connected to the valence wave function via a linear combination of the core wave functions,

$$|\psi\rangle = |\phi\rangle + \sum_{n=1}^N \alpha_n |\chi_n\rangle. \quad (2.55)$$

Due to the orthogonality of the wave function and the core functions,  $\langle \chi_n | \psi \rangle = 0$ , the coefficients of the core wave functions are determined by a scalar product of the pseudo wave function  $|\phi\rangle$  with the respective core wave function  $\langle \chi_n |$ ,

$$\alpha_n = -\langle \chi_n | \phi \rangle. \quad (2.56)$$

This relation can be reinserted into the definition of the pseudo wave function Eq. (2.55), which yields the following expression:

$$|\psi\rangle = |\phi\rangle - \sum_{n=1}^N |\chi_n\rangle \langle \chi_n | \phi \rangle. \quad (2.57)$$

This can be inserted into the Schrödinger equation, which then can be rearranged to finally take on the form

$$\left( \hat{H} + \sum_{n=1}^N (E - E_n) |\chi_n\rangle \langle \chi_n| \right) |\phi\rangle = E |\phi\rangle. \quad (2.58)$$

What we have now is a modified Schrödinger equation with an additional non-local potential. If we consider that the Hamiltonian  $\hat{H}$  consists of a kinetic part and a potential  $V(\hat{\mathbf{r}})$ , a transformation into the real-space representation results in the following Schrödinger equation:

$$-\frac{\hbar^2}{2m} \nabla^2 \phi(\mathbf{r}) + V(\mathbf{r}) \phi(\mathbf{r}) + \int \sum_{n=1}^N (E - E_n) \chi_n(\mathbf{r}) \chi_n^*(\mathbf{r}') \phi(\mathbf{r}') d^3 r' = E \phi(\mathbf{r}). \quad (2.59)$$

The non-locality of the additional potential comes on the one hand from the energy dependence, which means that different pseudo wave functions “see” different potentials, and on the other hand there is also a space-like non-locality because the

potential cannot be brought into a form like  $\tilde{V}(\mathbf{r})\phi(\mathbf{r})$ . Note that the eigenvalue of the pseudo wave function with respect to the pseudo Hamiltonian is the same eigenvalue that the real valence state wave function has with respect to the real Hamiltonian. The pseudo wave function is not unique, though. This can be seen when an arbitrary linear combination of core wave functions is added to the pseudo wave function. First, we let the additional non-local potential operator act on the modified pseudo wave function:

$$\underbrace{\left( \sum_{n=1}^N (E - E_n) |\chi_n\rangle \langle \chi_n| \right)}_{\hat{V}_{\text{nl}}} \left( |\phi\rangle + \sum_{i=1}^N \beta_i |\chi_i\rangle \right) = \hat{V}_{\text{nl}} |\phi\rangle + \sum_{n=1}^n (E - E_n) \beta_n |\chi_n\rangle. \quad (2.60)$$

Here, the double sum disappears due to the orthogonality of the core wave functions  $\langle \chi_i | \chi_j \rangle = \delta_{ij}$ . Then, we let the original Hamiltonian act on the modified pseudo wave function:

$$\hat{H} \left( |\phi\rangle + \sum_{n=1}^N \beta_n |\chi_n\rangle \right) = \hat{H} |\phi\rangle + \sum_{n=1}^N \beta_n \hat{H} |\chi_n\rangle = \hat{H} |\phi\rangle + \sum_{n=1}^N \beta_n E_n |\chi_n\rangle. \quad (2.61)$$

Now these two equations can be added up, which results in the cancellation of all terms that include  $E_n$  on the right side:

$$\left( \hat{H} + \hat{V}_{\text{nl}} \right) \left( |\phi\rangle + \sum_{n=1}^N \beta_n |\chi_n\rangle \right) = \underbrace{\left( \hat{H} + \hat{V}_{\text{nl}} \right) |\phi\rangle}_{E|\phi\rangle} + E \sum_{n=1}^N \beta_n |\chi_n\rangle = E \left( |\phi\rangle + \sum_{n=1}^N \beta_n |\chi_n\rangle \right). \quad (2.62)$$

We can see that the modified pseudo wave function is a solution to the same pseudo Hamiltonian as for the unmodified version and also for the same eigenvalue. A famous method to create pseudopotentials was proposed by TOULLIER and MARTINS [78]. The main idea was to create a pseudo wave function with desired properties beforehand and construct the pseudopotential afterwards, so that it yields the desired pseudo wave function. These pseudo wave functions generally have the form of a radial function  $R_{nl}^{\text{PP}}(r)$  which is multiplied with some spherical harmonics. Note that the subscript here is a set of two quantum numbers  $n$  and  $l$ , unlike as in  $\hat{V}_{\text{nl}}$  where it simply meant “non-local”. The superscript stands for pseudopotential which distinguishes it from the all-electron  $R_{nl}^{\text{AE}}(r)$  radial function with which it must be compared. The radial part of the pseudo wave function  $R_{nl}^{\text{PP}}(r)$  must have some specific properties in order to be suitable for our purposes. These requirements are based on the original work of HAMANN, SCHLÜTER and CHIANG, who introduced the concept of norm-conserving pseudopotentials back in 1979 [79]. The first requirement for the radial part of the pseudo wave function is that it has no nodes because the wiggling that is associated with those nodes is undesired. The second

property is that the pseudo wave functions and the all-electron wave functions are identical beyond some cutoff radius  $r_{nl}^C$ ,

$$R_{nl}^{\text{PP}}(r) = R_{nl}^{\text{AE}}(r) \quad \forall r > r_{nl}^C. \quad (2.63)$$

This cutoff radius is not universal and depends on the quantum numbers of the specific wave function. This condition assures that overlaps of wave functions that are associated with neighbouring atoms are represented accurately, which is important because they have a crucial influence on the chemical bonding behaviour. The third condition that must be fulfilled is the charge equality inside a sphere described by the cutoff radius:

$$\int_0^{r_{nl}^C} r^2 R_{nl}^{\text{PP}}(r) dr = \int_0^{r_{nl}^C} r^2 R_{nl}^{\text{AR}}(r) dr. \quad (2.64)$$

This, together with the second requirement ensures that the total charge, or integrated probability density of both wave functions is the same. The fourth and last condition that has to be satisfied is the equality of the eigenvalues:

$$E_{nl}^{\text{PP}} = E_{nl}^{\text{AE}}. \quad (2.65)$$

Once one has found such a pseudo wave function, it is possible to construct the pseudo potential by inverting the radial part of the Schrödinger equation,

$$\begin{aligned} \left( -\frac{\hbar^2}{2m_e} \partial_r^2 + \frac{\hbar^2 l(l+1)}{2m_e r^2} + V_{nl}^{\text{PP}}(r) \right) r R_{nl}^{\text{PP}}(r) &= E_{nl}^{\text{PP}} r R_{nl}^{\text{PP}}(r) \\ \Leftrightarrow \\ V_{nl}^{\text{PP}}(r) &= E_{nl}^{\text{PP}} - \frac{\hbar^2 l(l+1)}{2m_e r^2} + \frac{\hbar^2 \partial_r^2 (r R_{nl}^{\text{PP}}(r))}{2m_e r R_{nl}^{\text{PP}}(r)}. \end{aligned} \quad (2.66)$$

The pseudo potential in Eq. (2.66) is the so-called screened pseudo potential. This potential can be transformed into the semilocal ionic pseudo potential by subtracting the Hartree and exchange-correlation potentials that arise from the pseudo wave functions. This semilocal form can then be transformed into a non-local form by using the procedure of KLEINMAN and BYLANDER [80]. Since the radial part of the Schrödinger equation is an ordinary second order differential equation, the wave function is determined by its value **and** the value of its derivative at a specific yet arbitrary point  $r_0$  for any energy  $E$  (not necessary the eigenvalue). The logarithmic derivative

$$\frac{\partial}{\partial r} \ln \left( R_{nl}^{\text{PP}}(r) \right) \Big|_{r=r_0} = \frac{1}{R_{nl}^{\text{PP}}(r)} \frac{\partial R_{nl}^{\text{PP}}(r)}{\partial r} \Big|_{r=r_0} \quad (2.67)$$

is thus a quantity well suited for describing the pseudo wave function. As a test for pseudopotentials the logarithmic derivative of the pseudo wave function at a position  $r_0 \geq r_{nl}^C$  as a function of the energy  $E$  is compared with the same quantity for the all-electron wave function. A good accordance between those two quantities is an

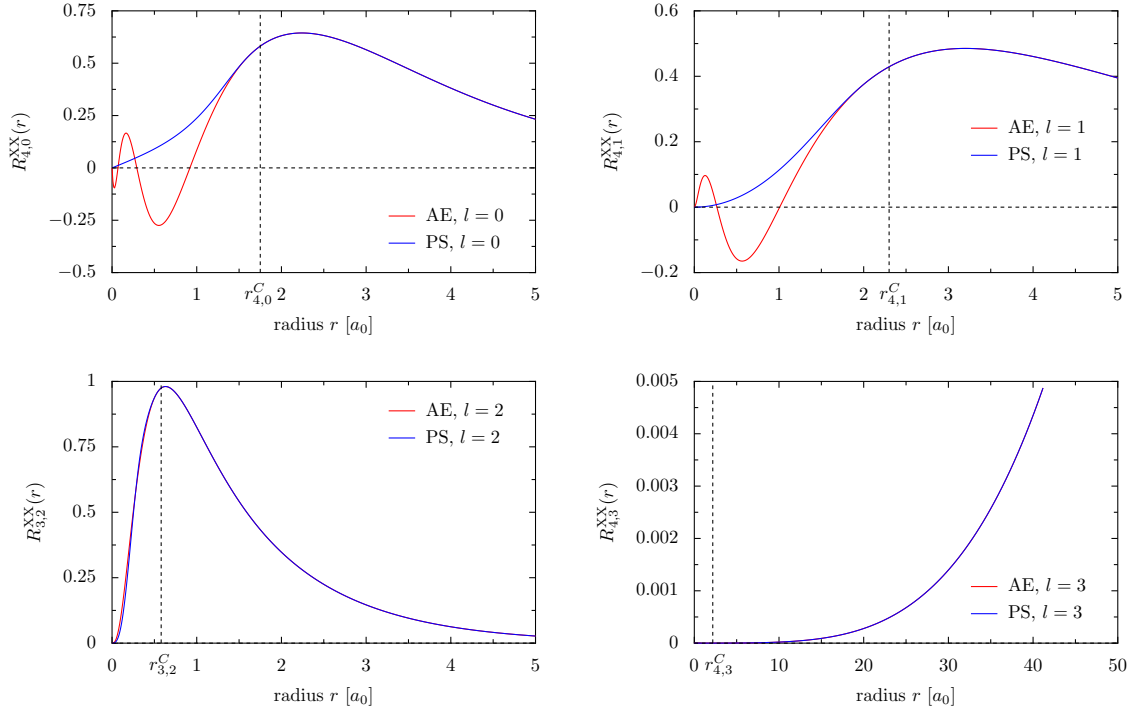


Figure 2.3: Radial parts of wave functions  $R_{n,l}^{XX}(r)$  (XX = PS for pseudo wave function, XX = AE for all-electron) for different angular momenta  $l$ . The cutoff radii are depicted as vertical dotted lines. The position of the cutoff radius is usually chosen near the last extremal point of the all-electron wave function. All radii are given in atomic units  $a_0$ .

indication for a good transferability, which means that the potential can be used in different chemical environments. The agreements of the logarithmic derivatives of the all-electron and the pseudo wave function and their first derivatives with respect to the energy for  $r > r_{nl}^C$  can be used to test the quality of the pseudopotentials. These requirements can be summarized in a formula that can be found in the original paper of HAMANN *et al.* [79],

$$-2\pi(rR_{nl}^{\text{PP}}(E, r))^2 \frac{\partial}{\partial E} \frac{\partial}{\partial r} \ln \left( R_{nl}^{\text{PP}}(E, r) \right) \Big|_{r_{nl}^C}^{E_{nl}} = 4\pi \int_0^{r_{nl}^C} r^2 |R_{nl}^{\text{PP}}(E, r)|^2 dr. \quad (2.68)$$

Here  $R_{nl}^{\text{PP}}(E, r)$  denotes the eigenfunction of the pseudo Hamiltonian from Eq. (2.66) with an arbitrary energy  $E$  instead of the real eigenvalue  $E_{nl}^{\text{PP}}$ .

When pseudopotentials are created for SIESTA by using the *atom* program, one has to specify the electronic (valence) configuration of a specific atom and define the cutoff radii for each valence orbital. A comparison of the all-electron and the pseudo wave functions for the atom Ni for different angular momenta is given in Fig. 2.3. The atomic valence configuration for this case is  $4s^2 4p^0 3d^8 4f^0$ , which gives a

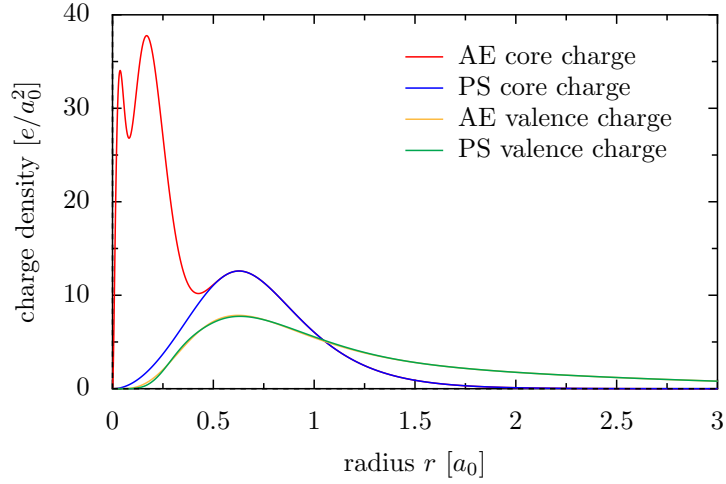


Figure 2.4: Charge densities for pseudo and all-electron wave functions. The valence charge densities are practically identical. A non-linear core correction was used with a pseudo core radius  $r_{\text{PC}} = 0.60 a_0$ .

total number of 10 valence electrons. When comparing the pseudo and all-electron wave functions one notices the smoothness of the pseudo wave functions due to the absence of the wiggling near the origin. Beyond the cutoff radius the pseudo wave functions are identical to the all-electron wave functions, and inside the cutoff radius a norm conservation is present. The charge that is assigned to the pseudo wave functions as well as the charge for the all-electron wave functions can be seen in Fig. 2.4. As far as the valence charge is concerned (green and orange curve), both curves are practically identical. For the core charge in this case a so called non-linear core correction was used as proposed by LOUIE *et al.* [81], (blue curve). A core correction is necessary if there is a significant overlap between the core- and valence charge density. In that case a linearisation of the exchange-correlation functional, which results in a separation of the valence- and the core density, is not possible anymore,

$$E_{XC}[n(\mathbf{r})] \neq E_{XC}[n_V(\mathbf{r})] + E_{XC}[n_C(\mathbf{r})]. \quad (2.69)$$

In the approach by LOUIE the ionic pseudopotential is generated like

$$V_{nl}^{\text{ion}}(\mathbf{r}) = V_{nl}^{\text{PP}}(\mathbf{r}) - V_H(\rho_{\text{PV}}(\mathbf{r})) - V_{XC}(\rho_{\text{PV}}(\mathbf{r}) + \rho_{\text{PC}}(\mathbf{r}), \xi(\mathbf{r})), \quad (2.70)$$

where  $V_{nl}^{\text{PP}}(\mathbf{r})$  is the screened pseudopotential from Eq. (2.66),  $\rho_{\text{PV}}(\mathbf{r})$  is the valence charge density of the pseudo wave functions,  $\rho_{\text{PC}}(\mathbf{r})$  is the pseudo core charge density, and  $\xi(\mathbf{r})$  is the spin polarization which is defined as,

$$\xi(\mathbf{r}) = \frac{\rho_{\text{PV}}(\mathbf{r}) - \rho_{\text{PC}}(\mathbf{r})}{\rho_{\text{PV}}(\mathbf{r}) + \rho_{\text{PC}}(\mathbf{r})}. \quad (2.71)$$

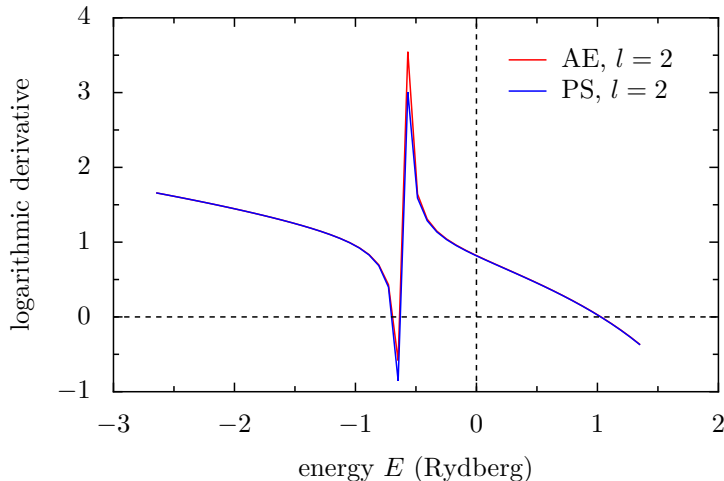


Figure 2.5: Logarithmic derivatives for the all-electron wave function and the pseudo wave function for the Ni  $3d$  orbital ( $l = 2$ ) versus the energy. The radius for which the logarithmic derivative was calculated is  $3a_0$ .

Another case where non-linear core corrections are often used is in spin density calculations. In our Ni example the charge density overlap is quite large as can be seen in Fig. 2.4, and furthermore we are interested in a spin polarized density for future use in half-metallic ferromagnets, so both arguments for using a core correction apply here. In the formalism by LOUIE, the pseudo core charge density is required to be equal to the all-electron core charge density beyond some pseudo core radius  $r_{PC}$ , and for all smaller radii behaves according to the formula

$$\rho_{PC}(r) = Ar \sin(br). \quad (2.72)$$

Here,  $A$  and  $b$  are parameters that have to be chosen accurately to provide a smooth matching to the all-electron core density. This formula, however, is only used for pseudo potentials in the local density approximation. For GGA pseudo potentials (as in this case) another pseudo core charge density is employed:

$$\rho_{PC}(r) = r^2 \exp(a + br^2 + cr^4). \quad (2.73)$$

Here, the parameters  $a$ ,  $b$  and  $c$  are chosen such that the density as well as its derivatives up to second order are continuous. In our example the values were calculated to be  $a = 4.153$ ,  $b = -0.938$  and  $c = -2.052$ . The pseudo core radius  $r_{PC}$  was chosen to be  $0.60a_0$ , which is approximately the position of the last maximum of the all-electron core charge density. The total charge inside the pseudo core for this example turned out to be  $9.00e$ , which is half of the total all-electron core charge. In Fig. 2.5 the logarithmic derivatives, compare Eq. (2.67), for the Ni  $3d$  pseudo- and all-electron states are shown. The radius  $r_0$  for which the logarithmic derivative was calculated is  $3a_0$ . The cutoff radius for the  $l = 2$  pseudo wave function

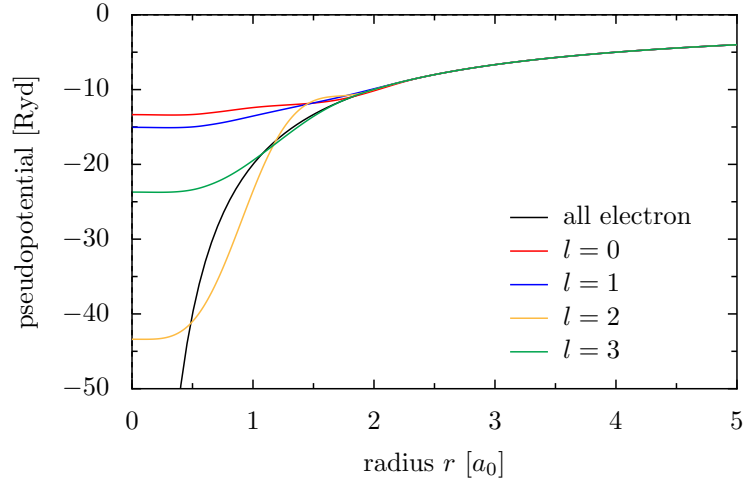


Figure 2.6: Pseudopotentials for different angular momenta. Beyond the cutoff radius the potentials show a typical  $-\frac{Z}{r}$  behaviour.

$r_{3,2}^C = 0.58 a_0$  (as seen in Fig. 2.3), i.e., much smaller than  $r_0$ . The good accordance of the pseudo logarithmic derivative with the all-electron one is an indication for high transferability.

In Fig. 2.6 the unscreened pseudopotentials, which are the potentials from Eq. (2.66) with subtracted Hartree- and exchange-correlation potentials, are shown for different angular momenta. For large radii they all show the typical Coulomb behaviour of  $-\frac{Z}{r}$ . The value of  $Z$ , however, is not the atomic number of the specific element (which would be 28 for Ni), but twice the charge of the pseudo atom, which is determined by the number of valence electrons. In this example the total number of valence electrons is 10, which results in a asymptote of the form  $-\frac{20}{r}$ . For small radii the non-local part dominates since the angular-momentum dependency splits up the potential. Note that the divergence of the potential at  $r = 0$  is removed due to the pseudopotential approach. The correct choice of pseudopotentials is a crucial part for any electronic structure calculation that uses this approximation. An incorrect choice may lead to entirely different physical predictions for a specific material, sometimes even without producing an error during computation. Therefore, experience or known results are helpful to determine if a specific pseudopotential is a good choice for a specific problem.



# 3 Basics of Transport Theory

## Contents

---

<b>3.1</b>	<b>The Transport Problem . . . . .</b>	<b>31</b>
<b>3.2</b>	<b>Non-Equilibrium Green's Function Formalism . . . . .</b>	<b>33</b>
<b>3.3</b>	<b>The SMEAGOL Code . . . . .</b>	<b>41</b>

---

Regarding possible applications of new materials, besides the electronic structure, the transport properties play a major role in determining the usefulness of a specific material for a specific purpose. The goal of this chapter is to define the transport problem, which is considered in the later chapters and to give an introduction to the non-equilibrium Green's function (NEGF) formalism, which is used to solve this problem. The introduction is kept as short as possible, yet as detailed as necessary to obtain the transmission coefficient from a given Hamiltonian.

## 3.1 The Transport Problem

The transport properties of nano structures are particularly interesting in regarding their possible usage in actual devices such as logic gates or data storage media. Due to the small size of the systems, sometimes only a single atom, an accurate quantum mechanical description of the transport process is necessary. The typical setup for such a problem consists of a sample, which can be a molecule, a single atom, or a thin layer of a specific material, **and** two semi-infinite leads which act as a charge reservoir for the system. A quantum mechanical model for such a transport setup is displayed in Fig. 3.1. The leads on both sides are each described by two different Hamiltonians, an “on-site” Hamiltonian  $\hat{H}_0$  for atoms/layers and a “hopping” Hamiltonian  $\hat{H}_1$  for the connection between atoms/layers. Between the two leads lies the extended molecule. This extended molecule consists of the scattering region, which is described by a Hamiltonian  $\hat{H}_M$  and a few layers of the lead material. The reason for why lead layers are included in the extended molecule is that the electrostatic potential of the extended molecule must match the one from the leads at the interface. Inside the extended molecule however, the leads are connected to the scattering region with the Hamiltonians  $\hat{H}_{LM}$  for the left side and

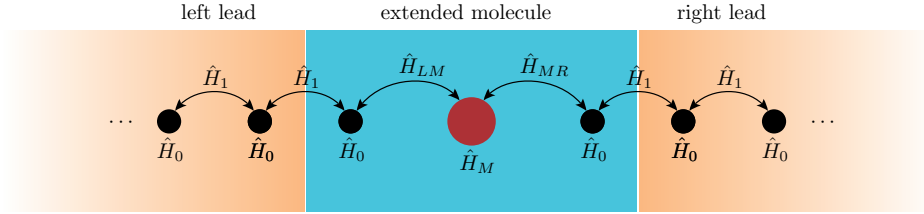


Figure 3.1: Visualization of the transport problem. Two semi-infinite leads are connected to an extended molecule. The extended molecule consists of the scattering region plus a few layers of the leads.

$\hat{H}_{MR}$  (and their respective conjugate transposed versions) for the right side. In the non-equilibrium case the two leads lie on different chemical potentials and a current can flow through the extended molecule. The leads on both sides are required to be strictly periodical without any defects. A useful concept for a quantum mechanical description of the leads is the concept of a principal layer. Depending on the actual structure of the leads, this principal layer may consist of a single atom, or many layers of different atoms. The principal layer is defined as the smallest structure that is periodically repeated in the transport direction and is only interacting with the nearest neighbouring principal layer. Going back to the model in Fig. 3.1, the Hamiltonian  $\hat{H}_0$  describes exactly one of these principal layers. In order to explain the concept of a principal layer, let us consider a linear chain of quantum dots in a tight-binding model. In this specific example we allow a hopping of the particle over a distance of three lattice sites. This means that the particle's hopping probability from lattice site  $i$  to the lattice site  $i + 3$  is non-zero. In this case, the Hamiltonian has on-site energies on the main-diagonal and hopping parameters on the next three superdiagonals. The principal layer is then defined as a block matrix that has just the right size so that the full Hamiltonian can be written as a block-tridiagonal matrix:

$$\begin{pmatrix} \epsilon & \gamma_1 & \gamma_2 & \gamma_3 & 0 & 0 \\ \gamma_1^* & \epsilon & \gamma_1 & \gamma_2 & \gamma_3 & 0 \\ \gamma_2^* & \gamma_1^* & \epsilon & \gamma_1 & \gamma_2 & \gamma_3 \\ \gamma_3^* & \gamma_2^* & \gamma_1^* & \epsilon & \gamma_1 & \gamma_2 \\ 0 & \gamma_3^* & \gamma_2^* & \gamma_1^* & \epsilon & \gamma_1 \\ 0 & 0 & \gamma_3^* & \gamma_2^* & \gamma_1^* & \epsilon \end{pmatrix} \Rightarrow \begin{pmatrix} \epsilon & \gamma_1 & \gamma_2 & \gamma_3 & 0 & 0 \\ \gamma_1^* & \epsilon & \gamma_1 & \gamma_2 & \gamma_3 & 0 \\ \gamma_2^* & \gamma_1^* & \epsilon & \gamma_1 & \gamma_2 & \gamma_3 \\ \gamma_3^* & \gamma_2^* & \gamma_1^* & \epsilon & \gamma_1 & \gamma_2 \\ 0 & \gamma_3^* & \gamma_2^* & \gamma_1^* & \epsilon & \gamma_1 \\ 0 & 0 & \gamma_3^* & \gamma_2^* & \gamma_1^* & \epsilon \end{pmatrix}.$$

On the left hand side, the principal layer is chosen too small because the  $\gamma_3$  and  $\gamma_3^*$  hopping parameters require a third superdiagonal of block matrices. On the right hand side the size of the principal layer is increased so that the  $\gamma_3$  and  $\gamma_3^*$  are now included in the first superdiagonal of block matrices so that now the Hamiltonian of the leads can be written as a true block-tridiagonal matrix. For the more general case of a hopping over the next  $n$  sites, this means that the principal layer consists of  $n$  sites as well. By using these principal layers, the whole Hamiltonian, including



molecule in the middle is of finite size, the sub-Hamiltonians for the semi-infinite leads on both sides are, of course, infinite. When we compare this Hamiltonian with the one from Eq. (3.1) we can identify  $\hat{H}_{L/R}$  with the block-tridiagonal matrix consisting of  $\hat{H}_0$  and  $\hat{H}_1$ . For the matrices  $\hat{\tau}_L$  and  $\hat{\tau}_R$ , which describe the connection of the leads to the molecule, we have

$$\hat{\tau}_L = \begin{pmatrix} 0 \\ \vdots \\ 0 \\ \hat{H}_{LM} \end{pmatrix} \quad \text{and} \quad \hat{\tau}_R = \begin{pmatrix} \hat{H}_{RM} \\ 0 \\ \vdots \\ 0 \end{pmatrix}. \quad (3.3)$$

In this notation,  $\hat{H}_{RM}$  is equal to  $\hat{H}_{MR}^\dagger$ . The matrices  $\hat{\tau}_{L/R}$  have the same number of columns as  $\hat{H}_M$  but infinite many rows. For the conjugate transposed matrices  $\hat{\tau}_{L/R}^\dagger$  obviously the opposite is true. Now we can define an energy-dependent single-particle Green's function for the whole Hamiltonian,

$$\hat{G}(E) = (E - \hat{H})^{-1}, \quad (3.4)$$

where  $\hat{H}$  is the  $3 \times 3$  block matrix from Eq. (3.2). Next, we distinguish two different kinds of Green's functions, namely the retarded and the advanced Green's function. They can be derived from Eq. (3.4) by adding (subtracting) an infinitesimally small imaginary part to (from) the energy:

$$\hat{G}^r(E) = \lim_{\delta \rightarrow 0^+} (E - \hat{H} + i\delta)^{-1} \quad (3.5)$$

$$\hat{G}^a(E) = \lim_{\delta \rightarrow 0^+} (E - \hat{H} - i\delta)^{-1}. \quad (3.6)$$

From now on, unless stated otherwise, we are always using the retarded Green's function and therefore drop the superscript  $r$ . The advanced Green's function is then simply the conjugate transposed retarded Green's function.

$$\hat{G}^a(E) \equiv \hat{G}^\dagger(E). \quad (3.7)$$

The time independent Schrödinger equation (3.2) can also be considered as a system of linear equations that reads as follows:

$$\hat{H}_L |\psi_L\rangle + \hat{\tau}_L |\psi_M\rangle = E |\psi_L\rangle, \quad (3.8)$$

$$\hat{\tau}_L^\dagger |\psi_L\rangle + \hat{H}_M |\psi_M\rangle + \hat{\tau}_R^\dagger |\psi_R\rangle = E |\psi_M\rangle, \quad (3.9)$$

$$\hat{\tau}_2 |\psi_M\rangle + \hat{H}_R |\psi_R\rangle = E |\psi_R\rangle. \quad (3.10)$$

Equations (3.8) and (3.10) can be rewritten in terms of the so called surface Green's functions  $\hat{g}_{L/R}(E)$ ,

$$|\psi_L\rangle = (E - \hat{H}_L)^{-1} \hat{\tau}_L |\psi_M\rangle \equiv \hat{g}_L(E) \hat{\tau}_L |\psi_M\rangle \quad (3.11)$$

$$|\psi_R\rangle = (E - \hat{H}_R)^{-1} \hat{\tau}_R |\psi_M\rangle \equiv \hat{g}_R(E) \hat{\tau}_R |\psi_M\rangle. \quad (3.12)$$

These expression can now be inserted into Eq. (3.9) which results in an equation that only contains the wave function of the molecule  $|\psi_M\rangle$ ,

$$\underbrace{\hat{\tau}_L^\dagger \hat{g}_L(E) \hat{\tau}_L}_{\hat{\Sigma}_L} |\psi_M\rangle + \hat{H}_M |\psi_M\rangle + \underbrace{\hat{\tau}_R^\dagger \hat{g}_R(E) \hat{\tau}_R}_{\hat{\Sigma}_R} |\psi_M\rangle = E |\psi_M\rangle, \quad (3.13)$$

where  $\hat{\Sigma}_L$  and  $\hat{\Sigma}_R$  are the self energies of the left and the right lead. The Green's function  $\hat{G}(E)$  can, similarly to the full Hamiltonian  $\hat{H}$ , be written as a block matrix. Therefore we transform the definition of the Green's function in Eq. (3.4) and rewrite it as

$$\begin{pmatrix} E - \hat{H}_L & -\hat{\tau}_L & 0 \\ -\hat{\tau}_L^\dagger & E - \hat{H}_M & -\hat{\tau}_R^\dagger \\ 0 & -\hat{\tau}_R & E - \hat{H}_R \end{pmatrix} \begin{pmatrix} \hat{G}_L & \hat{G}_{LM} & \hat{G}_{LR} \\ \hat{G}_{ML} & \hat{G}_M & \hat{G}_{MR} \\ \hat{G}_{RL} & \hat{G}_{RM} & \hat{G}_R \end{pmatrix} = \begin{pmatrix} \mathbb{1} & 0 & 0 \\ 0 & \mathbb{1} & 0 \\ 0 & 0 & \mathbb{1} \end{pmatrix}. \quad (3.14)$$

Similar to Eq. (3.2), that yielded Eqs. (3.8)-(3.10), also Eq. (3.14) can be interpreted as a system of linear equations, only this time there are 9 equations and the ‘‘variables’’ are the blocks of the Green's function. Now let us consider the three equations that are connected with the second column of Eq. (3.14):

$$(E - \hat{H}_L) \hat{G}_{LM} - \hat{\tau}_L \hat{G}_M = 0, \quad (3.15)$$

$$-\hat{\tau}_L^\dagger \hat{G}_{LM} + (E - \hat{H}_M) \hat{G}_M - \hat{\tau}_R^\dagger \hat{G}_{RM} = \mathbb{1}, \quad (3.16)$$

$$-\hat{\tau}_R \hat{G}_M + (E - \hat{H}_R) \hat{G}_{RM} = 0. \quad (3.17)$$

Analogously to Eqs. (3.8) and (3.10) the blocks  $\hat{G}_{LM}$  and  $\hat{G}_{RM}$  can be written in terms of the central block  $\hat{G}_M$  by using the surface Green's functions  $\hat{g}_{L/R}(E)$ :

$$\hat{G}_{LM} = \hat{g}_L(E) \hat{\tau}_L \hat{G}_M \quad (3.18)$$

$$\hat{G}_{RM} = \hat{g}_R(E) \hat{\tau}_R \hat{G}_M. \quad (3.19)$$

These expressions can now be inserted into Eq. (3.16) which results in the final form of the molecule's retarded Green's function,

$$\hat{G}_M = (E - \hat{\Sigma}_L - \hat{\Sigma}_R - \hat{H}_M)^{-1}, \quad (3.20)$$

where we have introduced the self energies  $\hat{\Sigma}_\alpha = \hat{\tau}_\alpha^\dagger \hat{g}_\alpha(E) \hat{\tau}_\alpha$  of the leads. Now, we use the information gathered so far to calculate the retarded response to a wave incoming from the left side. The incoming wave is denoted by  $|\phi\rangle$  and is an eigenstate of the left-side Hamiltonian  $\hat{H}_L$  with the eigenenergy  $E$ . We must therefore solve the following Schrödinger equation:

$$\begin{pmatrix} \hat{H}_L & \hat{\tau}_L & 0 \\ \hat{\tau}_L^\dagger & \hat{H}_M & \hat{\tau}_R^\dagger \\ 0 & \hat{\tau}_R & \hat{H}_R \end{pmatrix} \begin{pmatrix} |\phi\rangle + |\psi_L\rangle \\ |\psi_M\rangle \\ |\psi_R\rangle \end{pmatrix} = E \begin{pmatrix} |\phi\rangle + |\psi_L\rangle \\ |\psi_M\rangle \\ |\psi_R\rangle \end{pmatrix}. \quad (3.21)$$

We can now separate the left part into an action part, containing only the incoming wave  $|\phi\rangle$  and a response part containing only the response functions  $|\psi_\alpha\rangle$ :

$$\begin{pmatrix} \hat{H}_L & \hat{\tau}_L & 0 \\ \hat{\tau}_L^\dagger & \hat{H}_M & \hat{\tau}_R^\dagger \\ 0 & \hat{\tau}_R & \hat{H}_R \end{pmatrix} \begin{pmatrix} |\phi\rangle \\ 0 \\ 0 \end{pmatrix} + \hat{H} \begin{pmatrix} |\psi_L\rangle \\ |\psi_M\rangle \\ |\psi_R\rangle \end{pmatrix} = E \begin{pmatrix} |\phi\rangle + |\psi_L\rangle \\ |\psi_M\rangle \\ |\psi_R\rangle \end{pmatrix}. \quad (3.22)$$

The leftmost matrix vector product can be evaluated by using the previously mentioned eigenvalue equation of the incoming wave  $\hat{H}_L|\phi\rangle = E|\phi\rangle$ :

$$\begin{pmatrix} E|\phi\rangle \\ \hat{\tau}_L^\dagger|\phi\rangle \\ 0 \end{pmatrix} + \hat{H} \begin{pmatrix} |\psi_L\rangle \\ |\psi_M\rangle \\ |\psi_R\rangle \end{pmatrix} = \begin{pmatrix} E|\phi\rangle + E|\psi_L\rangle \\ E|\psi_M\rangle \\ E|\psi_R\rangle \end{pmatrix}. \quad (3.23)$$

The term  $E|\phi\rangle$  in the first component of the equation cancels out on both sides. We now bring the response part to the right side of the equation and then multiply with  $(E - \hat{H})^{-1}$ , i.e., the retarded Green's function of the whole system. By doing so, we are able to write the retarded response to the incoming wave by means of the wave itself and the Green's functions:

$$\begin{pmatrix} |\psi_L\rangle \\ |\psi_M\rangle \\ |\psi_R\rangle \end{pmatrix} = \begin{pmatrix} \hat{G}_L & \hat{G}_{LM} & \hat{G}_{LR} \\ \hat{G}_{ML} & \hat{G}_M & \hat{G}_{MR} \\ \hat{G}_{RL} & \hat{G}_{RM} & \hat{G}_R \end{pmatrix} \begin{pmatrix} 0 \\ \hat{\tau}_L^\dagger|\phi\rangle \\ 0 \end{pmatrix}. \quad (3.24)$$

When we use the expressions (3.18) and (3.19) that relate the blocks  $\hat{G}_{LM}$  and  $\hat{G}_{RM}$  with the surface Green's functions and the retarded Green's function of the molecule, it is possible to write the retarded response in terms of the surface and central Green's functions:

$$|\psi_L\rangle = \hat{g}_L \hat{\tau}_L \hat{G}_M \hat{\tau}_L^\dagger |\phi\rangle, \quad (3.25)$$

$$|\psi_M\rangle = \hat{G}_M \hat{\tau}_L^\dagger |\phi\rangle, \quad (3.26)$$

$$|\psi_R\rangle = \hat{g}_R \hat{\tau}_R \hat{G}_M \hat{\tau}_L^\dagger |\phi\rangle. \quad (3.27)$$

These expressions are later needed when we want to calculate the charge current through the molecule. However, before we do that, we need an expression for the probability current in terms of the wave functions. This probability current is obtained by assuming that the probability to find an electron in the molecule is constant, which is equivalent to the assumption that the rate of electrons entering the molecule is the same as the rate of electrons leaving the molecule. Therefore, the time derivative of this quantity must vanish:

$$0 = \frac{\partial}{\partial t} \sum_{i \in M} \langle \psi | i \rangle \langle i | \psi \rangle = \sum_{i \in M} \left( \langle \dot{\psi} | i \rangle \langle i | \psi \rangle + \langle \psi | i \rangle \langle i | \dot{\psi} \rangle \right). \quad (3.28)$$

Here,  $i$  is an index that runs over the vector/matrix components that correspond to the molecule part of the wave function/Hamiltonian. The time derivative of the total wave function  $|\psi\rangle$  can be written by using the Schrödinger equation  $i\hbar|\dot{\psi}\rangle = \hat{H}|\psi\rangle$ :

$$0 = \frac{i}{\hbar} \sum_{i \in M} \left( \langle \psi | \hat{H} | i \rangle \langle i | \psi \rangle - \langle \psi | i \rangle \langle i | \hat{H} | \psi \rangle \right). \quad (3.29)$$

The minus sign in the brackets comes from the imaginary unit that was moved from the denominator to the numerator in the prefactor. The other term lacks that minus sign due to the additional minus from the complex conjugation. In the following we want to evaluate the term  $\sum_{i \in M} \langle \psi | \hat{H} | i \rangle \langle i | \psi \rangle$  explicitly and use the results analogously for the other term. The key for the correct evaluation is the sum of outer products  $|i\rangle\langle i|$  which leads to a diagonal matrix where only the molecule subspace is filled with 1's. Therefore, we can write,

$$\left( \langle \phi | + \langle \psi_L |, \langle \psi_M |, \langle \psi_R | \right) \begin{pmatrix} \hat{H}_L & \hat{\tau}_L & 0 \\ \hat{\tau}_L^\dagger & \hat{H}_M & \hat{\tau}_R^\dagger \\ 0 & \hat{\tau}_R & \hat{H}_R \end{pmatrix} \begin{pmatrix} 0 & 0 & 0 \\ 0 & \mathbf{1} & 0 \\ 0 & 0 & 0 \end{pmatrix} \begin{pmatrix} |\psi_L\rangle \\ |\psi_M\rangle \\ |\psi_R\rangle \end{pmatrix} \quad (3.30)$$

$$= \left( \langle \phi | + \langle \psi_L |, \langle \psi_M |, \langle \psi_R | \right) \begin{pmatrix} 0 & \hat{\tau}_L & 0 \\ 0 & \hat{H}_M & 0 \\ 0 & \hat{\tau}_R & 0 \end{pmatrix} \begin{pmatrix} |\psi_L\rangle \\ |\psi_M\rangle \\ |\psi_R\rangle \end{pmatrix} \quad (3.31)$$

$$= \left( 0, (\langle \phi | + \langle \psi_L |) \hat{\tau}_L + \langle \psi_M | \hat{H}_M + \langle \psi_R | \hat{\tau}_R, 0 \right) \begin{pmatrix} |\psi_L\rangle \\ |\psi_M\rangle \\ |\psi_R\rangle \end{pmatrix} \quad (3.32)$$

$$= \langle \psi_L | \hat{\tau}_L | \psi_M \rangle + \langle \psi_M | \hat{H}_M | \psi_M \rangle + \langle \psi_R | \hat{\tau}_R | \psi_M \rangle. \quad (3.33)$$

When the same is done for the other term one has to switch the positions of the Hamiltonian and the diagonal matrix, giving a similar result,

$$\sum_{i \in M} \langle \psi | i \rangle \langle i | \hat{H} | \psi \rangle = \langle \psi_M | \hat{\tau}_L^\dagger | \psi_L \rangle + \langle \psi_M | \hat{H}_M | \psi_M \rangle + \langle \psi_M | \hat{\tau}_R^\dagger | \psi_R \rangle. \quad (3.34)$$

When the two expressions are now inserted into Eq. (3.29), the expectation value of the molecule's Hamiltonian cancels out and we finally get,

$$0 = \frac{i}{\hbar} \left[ \left( \langle \psi_L | \hat{\tau}_L | \psi_M \rangle - \langle \psi_M | \hat{\tau}_L^\dagger | \psi_L \rangle \right) + \left( \langle \psi_R | \hat{\tau}_R | \psi_M \rangle - \langle \psi_M | \hat{\tau}_R^\dagger | \psi_R \rangle \right) \right], \quad (3.35)$$

where the left bracket describes the net current from the left side and the right bracket the net current from the right side. The electrical current is given by the probability current times the charge, in this case  $-e$ . In order to calculate the net current to the right side in terms of an incoming wave from the left side, we need

the relations from Eqs. (3.25)-(3.27) and their conjugate transposed versions. When these equations are inserted into the charge multiplied probability current, we obtain

$$\frac{-ie}{\hbar} \left( \langle \psi_R | \hat{\tau}_R | \psi_M \rangle - \langle \psi_M | \hat{\tau}_R^\dagger | \psi_R \rangle \right) \quad (3.36)$$

$$= \frac{-ie}{\hbar} \left( \langle \phi | \hat{\tau}_L \hat{G}_M^\dagger \hat{\tau}_R^\dagger \hat{g}_R^\dagger \hat{\tau}_R \hat{G}_M \hat{\tau}_L^\dagger | \phi \rangle - \langle \phi | \hat{\tau}_L \hat{G}_M^\dagger \hat{\tau}_R^\dagger \hat{g}_R \hat{\tau}_R \hat{G}_M \hat{\tau}_L^\dagger | \phi \rangle \right) \quad (3.37)$$

$$= \frac{-ie}{\hbar} \left( \langle \phi | \hat{\tau}_L \hat{G}_M^\dagger \hat{\tau}_R^\dagger (\hat{g}_R^\dagger - \hat{g}_R) \hat{\tau}_R \hat{G}_M \hat{\tau}_L^\dagger | \phi \rangle \right) \quad (3.38)$$

$$= \frac{e}{\hbar} \left( \langle \phi | \hat{\tau}_L \hat{G}_M^\dagger \hat{\Gamma}_R \hat{G}_M \hat{\tau}_L^\dagger | \phi \rangle \right). \quad (3.39)$$

Here, we have introduced the quantity  $\hat{\Gamma}_R = i\hat{\tau}_R^\dagger (\hat{g}_R - \hat{g}_R^\dagger) \hat{\tau}_R$ . The surface Green's function  $\hat{g}_R$  is an infinite square matrix and such is its conjugate transposed  $\hat{g}_R^\dagger$ . Due to the multiplication with the  $\hat{\tau}_R$  matrices, however,  $\hat{\Gamma}_R$  is a finite matrix, which can also be written in terms of the self energy of the corresponding lead,

$$\hat{\Gamma}_R = i(\hat{\Sigma}_R - \hat{\Sigma}_R^\dagger). \quad (3.40)$$

So far, we calculated the probability and charge current induced by a single incoming wave  $|\phi\rangle$ . An important aspect in the derivation of the retarded response to an incoming wave, see Eqs. (3.25)-(3.27), was that the incoming wave is an eigenstate of the left-side Hamiltonian with the specific eigenenergy  $E$ . The retarded Green's function of the molecule  $\hat{G}_M$ , the surface Green's functions and therefore also the newly defined object  $\hat{\Gamma}_R$  are thereby energy dependent. When we consider the leads as a reservoir with many particles, we thus also have to consider the whole energy spectrum.

Another aspect that was neglected until now was that a particle only can jump from the lead to the molecule if it was present in the lead to begin with. Here the Fermi distribution and the chemical potential of the lead become relevant. If we now consider all eigenstates of the (for example) left lead  $|\phi_n\rangle$  with their respective eigenenergies  $E_n$ , the probability that this specific state is occupied is given by the Fermi function  $f(E_n, \mu_L)$ , where  $\mu_L$  is the chemical potential of the (in this case) left lead. Thus, under consideration of spin degeneracy (factor of 2), we can write the total net current from the left lead as follows:

$$I_L = \frac{2e}{\hbar} \int_{-\infty}^{\infty} f(E, \mu_L) \sum_n \delta(E - E_n) \langle \phi_n | \hat{\tau}_L \hat{G}_M^\dagger \hat{\Gamma}_R \hat{G}_M \hat{\tau}_L^\dagger | \phi_n \rangle dE. \quad (3.41)$$

Since  $\hat{\tau}_L$  is a  $(\infty \times N)$  matrix and  $\hat{G}_M^\dagger$  is a  $(N \times N)$  matrix (without specifying what exactly  $N$  is), we can insert a  $(N \times N)$  unity matrix in between them without changing anything. This can be done by expanding the unity matrix in terms of some generic eigenbasis  $\mathbf{1} = \sum_m |m\rangle \langle m|$ . At this point I want to emphasize the difference

compared to what was done in Eq. (3.30). There, the identity was embedded in the Hilbert space of the whole system, which means that the vectors  $|\psi\rangle$  and  $|i\rangle$  were living in the same Hilbert space. Here however, the identity is not embedded in the whole system's Hilbert space which means that the vectors  $|\phi_n\rangle$  have infinite many rows while  $|m\rangle$  has only a finite number of rows and thus the scalar product  $\langle\phi_n|m\rangle$  is not defined. When the  $(N \times N)$  unity is inserted as previously described we get,

$$I_L = \frac{2e}{\hbar} \int_{-\infty}^{\infty} f(E, \mu_L) \sum_n \sum_m \delta(E - E_n) \langle\phi_n|\hat{\tau}_L|m\rangle \langle m|\hat{G}_M^\dagger \hat{\Gamma}_R \hat{G}_M \hat{\tau}_L^\dagger|\phi_n\rangle dE. \quad (3.42)$$

Although the scalar product  $\langle\phi_n|m\rangle$  is not defined, due to the fact that the operators are **not** square matrices, the terms that begin with a bra vector and end with a ket vector are still scalars and thus commute. Therefore, we can rearrange the integral to the following form:

$$I_L = \frac{2e}{\hbar} \int_{-\infty}^{\infty} f(E, \mu_L) \sum_m \langle m|\hat{G}_M^\dagger \hat{\Gamma}_R \hat{G}_M \hat{\tau}_L^\dagger \left( \sum_n \delta(E - E_n) |\phi_n\rangle \langle\phi_n| \right) \hat{\tau}_L|m\rangle dE. \quad (3.43)$$

All the terms containing the index  $n$  are now isolated and form a matrix, of which the trace yields the left lead's density of states. In the following we show that this matrix is related to  $\hat{\Gamma}_L$ , which is defined analogously to its right side counterpart,

$$\hat{\Gamma}_L = i\hat{\tau}_L^\dagger (\hat{g}_L - \hat{g}_L^\dagger) \hat{\tau}_L \quad (3.44)$$

$$= \lim_{\delta \rightarrow 0^+} i\hat{\tau}_L^\dagger \left( (E + i\delta - \hat{H}_L)^{-1} - (E - i\delta - \hat{H}_L)^{-1} \right) \hat{\tau}_L. \quad (3.45)$$

The operators inside the brackets can now be expanded in their eigenbasis, i.e., the eigenbasis of the left Hamiltonian  $\hat{H}_L$ , which is as we know  $\{|\phi_n\rangle\}$  with the respective eigenvalues  $\{E_n\}$ :

$$\hat{\Gamma}_L = \lim_{\delta \rightarrow 0^+} \sum_n i\hat{\tau}_L^\dagger \left( \frac{|\phi_n\rangle \langle\phi_n|}{E + i\delta - E_n} - \frac{|\phi_n\rangle \langle\phi_n|}{E - i\delta - E_n} \right) \hat{\tau}_L \quad (3.46)$$

$$= \lim_{\delta \rightarrow 0^+} \sum_n i\hat{\tau}_L^\dagger |\phi_n\rangle \langle\phi_n| \left( \frac{-2i\delta}{(E - E_n)^2 + \delta^2} \right) \hat{\tau}_L \quad (3.47)$$

$$= \sum_n \hat{\tau}_L^\dagger |\phi_n\rangle \langle\phi_n| 2\pi \lim_{\delta \rightarrow 0^+} \left( \frac{1}{\pi} \frac{\delta}{(E - E_n)^2 + \delta^2} \right) \hat{\tau}_L. \quad (3.48)$$

The term inside the brackets is a Lorentzian which, in the limit of vanishing  $\delta$ , yields the Dirac  $\delta$ -function [83]. With that, we have finally found the relation:

$$\hat{\Gamma}_L = 2\pi \hat{\tau}_L^\dagger \left( \sum_n \delta(E - E_n) |\phi_n\rangle \langle\phi_n| \right) \hat{\tau}_L. \quad (3.49)$$

Since the right hand side of this equation (without the factor of  $2\pi$ ) appears in the expression for the charge current in Eq. (3.43), we can replace it with  $\hat{\Gamma}_L$  divided by  $2\pi$ ,

$$I_L = \frac{e}{\pi\hbar} \int_{-\infty}^{\infty} f(E, \mu_L) \sum_m \langle m | \hat{G}_M^\dagger \hat{\Gamma}_R \hat{G}_M \hat{\Gamma}_L | m \rangle dE \quad (3.50)$$

$$= \frac{e}{\pi\hbar} \int_{-\infty}^{\infty} f(E, \mu_L) \text{Tr} \left( \hat{G}_M^\dagger \hat{\Gamma}_R \hat{G}_M \hat{\Gamma}_L \right) dE. \quad (3.51)$$

The total net current can now be calculated by subtracting the part of the current which is associated with the other contact. When we furthermore revoke the spin degeneracy by dividing the whole expression by 2 and add a spin index  $\sigma$ , we get the final result for the spin resolved current,

$$I_\sigma = \frac{e}{h} \int_{-\infty}^{\infty} \left( f(E, \mu_L) - f(E, \mu_R) \right) \text{Tr} \left( \hat{G}_M^{\sigma\dagger} \hat{\Gamma}_R^\sigma \hat{G}_M^\sigma \hat{\Gamma}_L^\sigma \right) dE. \quad (3.52)$$

This is the same expression that can be found in MEIR and WINGREEN'S article about the Landauer formula for an interacting electron region under the assumption of zero temperature and in linear response [84]. For a more general case, they find a more complicated formula. The difference of the chemical potentials determines (or is determined by) the bias voltage  $V$  that is applied to the molecule:

$$\mu_L - \mu_R = eV. \quad (3.53)$$

The trace inside the integral can be identified with the spin, energy **and** bias voltage dependent transmission:

$$T_\sigma(E, V) = \text{Tr} \left( \hat{G}_M^{\sigma\dagger} \hat{\Gamma}_R^\sigma \hat{G}_M^\sigma \hat{\Gamma}_L^\sigma \right). \quad (3.54)$$

The voltage dependency of the transmission comes from the self energies of the leads, since they depend on the sub-Hamiltonians  $\hat{H}_L$  and  $\hat{H}_R$ , which contain the applied voltage. With that, Eq. (3.54) can be identified with the transmission expression by LANDAUER and BÜTTIKER [85]. The given derivation of the current is a strong simplification. This can be seen easily since a single-particle picture is used in all steps. The presented derivation is only valid for non-interacting systems and should only serve as to show the basic idea. Interacting systems, however, can be treated in a similar way once a mean-field type decoupling is used. The same concept can be employed in DFT when an additional assumption is made, namely that the Kohn-Sham orbitals and bands have a physical meaning [86].

### 3.3 The SMEAGOL Code

The SMEAGOL code (**S**pin and **M**olecular **E**lectronics in an **A**tomically-**G**enerated **O**rbital **L**andscape) provides an *ab initio* method for calculating transmission coefficients and currents for nano-scale devices. It combines electronic structure calculations on the basis of density functional theory (provided by SIESTA) and the non-equilibrium Green's function formalism. For our purposes SMEAGOL turns out to be well-suited due to the fact that it provides a spin resolved transmission calculation, which is needed to describe the transport properties of half-metals. Technical details of the code that exceed the short introduction of the last section can be found in the original paper by ROCCA *et al.* [87]. Another important reference for the SMEAGOL code is the paper by IVAN RUNGGER and STEFANO SANVITO, where they describe a method for calculating the surface Green's functions [88]. In SMEAGOL, the calculation of the self energies and transport properties is done self-consistently. When the implicit dependence of the Hamiltonian  $\hat{H}_M$  on the charge density is known, as it is regularly the case in density functional theory, a trial density  $n(\mathbf{r})$  is chosen to calculate the Hamiltonian. This is used to calculate the retarded Green's function of the scattering region (the extended molecule to be more precise) and the objects  $\hat{\Gamma}_{L/R}$ . These objects are needed to compute the lesser Green's function,

$$\hat{G}_M^<(E) = i\hat{G}_M(E) \left( \hat{\Gamma}_L f(E, \mu_L) + \hat{\Gamma}_R f(E, \mu_R) \right) \hat{G}_M^\dagger(E), \quad (3.55)$$

which is in turn needed to calculate the charge density for the next iteration step. The charge density is connected to the lesser Green's function by the following expression:

$$n(\mathbf{r}) = \langle \mathbf{r} | \hat{\rho}_M | \mathbf{r} \rangle = \frac{1}{2\pi i} \int \langle \mathbf{r} | \hat{G}_M^<(E) | \mathbf{r} \rangle dE. \quad (3.56)$$

This charge density is then inserted into the functional of the Hamiltonian and the process begins anew. Self consistency is reached when the densities matrices  $\hat{\rho}_M$  of two consecutive iteration steps differ component-wise by less than some tolerance parameter  $\delta$ . When convergence is achieved the total current can be calculated with the Landauer formula Eq.(3.52). A technical difficulty in the process comes with the energy integration in Eq. (3.56) due to the fact that the integral is unbound. A trick that is done in SMEAGOL is to divide the density matrix into two parts, one so-called equilibrium density describing the situation when both leads are on the same potential level and a voltage dependent density matrix that is energetically bound by the Fermi functions of both leads. This reduces the energy range for the non-equilibrium part of the density matrix to (approximately) the bias voltage applied to the system. For the equilibrium part of the density matrix the integration is still unbound. However, this problem is solved by a contour integration method in the complex energy plane.



# 4 Transport in the Kronig-Penney Model

## Contents

---

<b>4.1</b>	<b>The Kronig-Penney Model . . . . .</b>	<b>43</b>
<b>4.2</b>	<b>The Transfer Matrix Method . . . . .</b>	<b>49</b>
<b>4.3</b>	<b>A Toy Model for Half-Metallic Transport . . . . .</b>	<b>53</b>

---

In this chapter we introduce the Kronig-Penney Model, one of the simplest models of a crystal that exhibits a band structure including band gaps. Furthermore, a method for calculating transmissions within this model is derived. This can be used to consider a transport problem according to Fig. 3.1 where the leads are explicitly given in terms of the Kronig-Penney model. A simple model of a half-metallic material is presented in the last section of this chapter, which is then analysed using the previously described method.

## 4.1 The Kronig-Penney Model

In this chapter we want to focus on a simple toy model for a crystal. This model was originally suggested by RALPH KRONIG and WILLIAM PENNEY in 1931 [89]. It describes a single particle in a periodic potential. In most examples this periodic potential is given by a sum of Dirac  $\delta$ -functions, making it amenable to an analytic solution of the Schrödinger equation. In some cases however, this representation of the potential may not be the most appropriate choice. For this chapter we choose a periodic box potential because in principle, any other potential could be approximated by a series of boxes. This provides a greater transferability of this method for arbitrary potentials. Also an additional degree of freedom (the width of the box) allows for additional fine-tuning regarding later results. In Fig. 4.1 the relevant parameters are defined. The height of the potential boxes (or barriers) is given by  $V$  and the width of those boxes is given by  $d$ . The lattice constant is defined as  $a$  which automatically determines the space of free propagation to have the width  $a - d$ . The different unit cells of the crystal are labeled with  $n - 1$ ,  $n$ ,  $n + 1$  and so

on. When we search for a solution of the time-independent Schrödinger equation,

$$-\frac{\hbar^2}{2m} \frac{d^2}{dx^2} \Psi(x) + V(x) \Psi(x) = E \Psi(x) \quad (4.1)$$

we make a plane-wave ansatz for a specific unit cell,

$$\Psi_n(x) = \begin{cases} a_n e^{iqx} + b_n e^{-iqx} & \text{for } V(x) = 0 \\ c_n e^{\lambda x} + d_n e^{-\lambda x} & \text{for } V(x) \neq 0 \end{cases}. \quad (4.2)$$

Here,  $q$  is the wave number for the free propagation and  $\lambda$  is an exponential growth/decay parameter for the region inside the potential barrier. Both of them are connected to the eigenenergy  $E$ . According to the stationary Schrödinger equation the relation between these parameters and the energy  $E$  is as follows:

$$q = \sqrt{\frac{2mE}{\hbar^2}} \quad (4.3)$$

$$\lambda = \sqrt{\frac{2m(V-E)}{\hbar^2}}. \quad (4.4)$$

In the following, we use atomic units, i.e., all lengths are expressed in units of the Bohr radius  $a_0 = \frac{\hbar^2}{me^2}$  and all energies in units of the Hartree energy  $E_H = \frac{\hbar^2}{ma_0^2}$ . This is equivalent to the setting  $\hbar = m = 1$  in Eq. (4.1). Note that we implicitly assumed that  $E < V$  and thus  $\lambda$  is a real number. If the energy of the wave function exceeds the height of the potential barrier, the exponential growth/decay parameter  $\lambda$  becomes imaginary. In order to find the coefficients in the wave function Eq. (4.2) we demand the continuity as well as the differentiability of the wave function at the two edges  $x_0, x_1$  of the potential barrier **and** the famous theorem by FELIX BLOCH [90] which states:

$$\Psi(x+a) = e^{ika} \Psi(x), \quad (4.5)$$

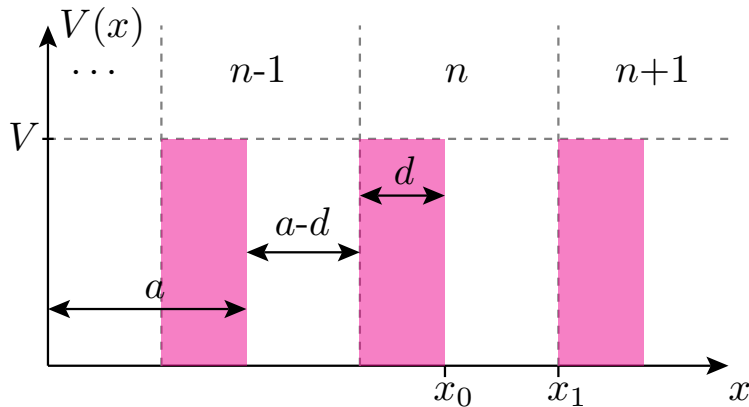


Figure 4.1: Scheme of the potential of the Kronig-Penney model. The lattice constant of the crystal is given by  $a$  and the width of the potential barrier is given by  $d$ .

where  $k$  is an arbitrary parameter, also called Bloch wave vector, and  $a$  is the lattice constant. Because the continuity and differentiability of the wave function at the left edge of the potential barrier  $x_1$  connects two adjacent unit cells, this would lead to equations containing  $a_n$  and  $b_n$  as well as  $c_{n+1}$  and  $d_{n+1}$ . By using Bloch's theorem the coefficients of the  $(n+1)$ -th unit cell can be related to the coefficients of the  $n$ -th unit cell,

$$c_{n+1} = c_n e^{ika - \lambda a} \quad (4.6)$$

$$d_{n+1} = d_n e^{ika + \lambda a}. \quad (4.7)$$

This allows us to formulate an array of four linear equations and four variables  $a_n, b_n, c_n$  and  $d_n$ . This equation array also contains the two positions  $x_0$  and  $x_1$  where the continuity and differentiability of the wave function was demanded. As a linear equation array it has a matrix representation which has the form,

$$\begin{pmatrix} -e^{iqx_0} & -e^{-iqx_0} & e^{\lambda x_0} & e^{-\lambda x_0} \\ -e^{iqx_1} & -e^{-iqx_1} & e^{ika + \lambda(x_0 - d)} & e^{ika - \lambda(x_0 - d)} \\ -ie^{iqx_0} & ie^{-iqx_0} & \lambda e^{\lambda x_0} & -\lambda e^{-\lambda x_0} \\ -iqe^{iqx_1} & iqe^{-iqx_1} & \lambda e^{ika + \lambda(x_0 - d)} & -\lambda e^{ika - \lambda(x_0 - d)} \end{pmatrix} \begin{pmatrix} a_n \\ b_n \\ c_n \\ d_n \end{pmatrix} = \begin{pmatrix} 0 \\ 0 \\ 0 \\ 0 \end{pmatrix}. \quad (4.8)$$

This is a homogeneous equation array which means there only exists a non-trivial solution if the matrix is not invertible, i.e. the determinant vanishes. Calculating the determinant for this matrix and searching for its roots yields the following transcendental equation:

$$\cos(ka) = \cosh(\lambda d) \cos(\underbrace{q(x_1 - x_0)}_{a-d}) + \frac{\lambda^2 - q^2}{2q\lambda} \sinh(\lambda d) \sin(\underbrace{q(x_1 - x_0)}_{a-d}). \quad (4.9)$$

An important observation is that the positions  $x_0$  and  $x_1$ , where the continuity and differentiability was demanded, only appear as a difference, i.e., in relative positions. This means that the absolute positions are irrelevant. This makes sense when we consider that the system, due to its periodicity, can be described by three characteristic values: the barrier width  $d$ , the barrier height  $V$ , and the distance between two barriers  $a - d$ . Any other dependence on the parameters  $x_0, x_1$  would be suspicious and thus would indicate an error in the calculation.

The results of the periodic  $\delta$ -function can be derived from the results of the periodic box potential. Therefore it is necessary to consider the limit  $d \rightarrow 0$  and simultaneously  $V \rightarrow \infty$  in such a way that  $dV \rightarrow A = \text{const}$ . While the hyperbolic cosine function in that limit becomes 1 and can be ignored, the hyperbolic sine function has to be replaced with its linear Taylor expansion, i.e.  $\lambda d$ . For the term  $\lambda^2 - q^2$  we find, according to Eq. (4.3) and Eq. (4.4), the expression  $\frac{2m}{\hbar^2}(V - 2E)$ . This is multiplied with  $d \rightarrow 0$  so that  $2Ed \rightarrow 0$  and  $Vd \rightarrow A$ . Including all these replacements in Eq. (4.9) yields the transcendental equation for the periodic

$\delta$ -potential:

$$\cos(ka) = \cos(qa) + \frac{mA}{\hbar^2 q} \sin(qa). \quad (4.10)$$

Now the band structure, the function  $E(k)$ , can be extracted from the transcendental equation by using the following scheme:

1. Assume an eigenenergy  $E$  (start with  $E = 0$ ).
2. Calculate the wave number  $q$  and the parameter  $\lambda$ .
3. Check if the absolute value of the right side of Eq. (4.9) is smaller than 1.
  - 3.1. If yes, calculate  $k = \pm \frac{1}{a} \arccos(\dots)$  and plot  $E$  versus  $k$ .
4. Restart at step 1 with a larger value for  $E$ .

The result of the procedure is shown in Fig. 4.2. The blue area depicts the allowed values for the right hand side to be identified with  $\cos(ka)$  and the other coloured areas represent the energy values where the right-hand side of Eq. (4.9) lies within the blue area. Thus the energy values that are covered by the three reddish areas are the energy bands or more precisely the energy band widths of the Kronig-Penney model. The real band structure, i.e. the function  $E(k)$  is depicted in Fig. 4.3 for the same parameters as in Fig. 4.9. The three different energy bands are highlighted with the respective color that was assigned in Fig. 4.2. The band structure in this plot is represented in the reduced zone scheme, which means the values of  $k$  range from  $-\frac{\pi}{a}$  to  $\frac{\pi}{a}$ . The length of this interval is  $\frac{2\pi}{a}$  which correspond to the periodicity

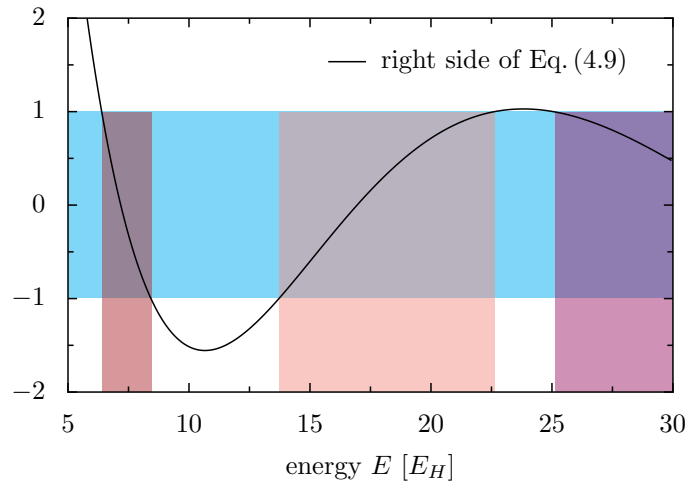


Figure 4.2: Graphical representation of the process that grants the band structure of the Kronig-Penney model. The blue red shaded areas indicate the energy ranges, where solutions exist. Values for the parameters are  $V = 10$ ,  $a = 1.1$  and  $d = 0.8$ .

that is implied in Bloch's theorem. The sizes of the band gaps depend on the height and width of the potential barrier in a non-trivial way. An increasing barrier height leads to a wider band gap, however a variation of the barrier width may increase the size of the first band gap but reduces the size of the second gap.

If we want to look at the wave function itself, we need the coefficients  $a_n, b_n, c_n$  and  $d_n$  that appear in Eq. (4.8). The vector of these coefficients is an element of the kernel of the matrix, which is defined as the set of vectors that are mapped onto the zero vector by said matrix. Since multiples of solutions of homogeneous equation arrays are also solutions, the absolute value of the vector  $(a_n, b_n, c_n, d_n)^T$  is irrelevant for the relation Eq. (4.8). This means that the vector is not uniquely determined. Generally a matrix may have several linear independent vectors in its kernel, however, for the specific matrix in Eq. (4.8) the number of linear independent vectors is either one, for the case that the energy  $E$  lies inside one of the energy bands, or zero, for the case where the energy lies within a band gap. Here we excluded the zero-vector, which is always an element of the kernel for obvious reasons. Relevant for us are only non-trivial solutions. The wave function is thus uniquely determined for a specific energy and a specific choice of  $k$  up to a constant phase-factor. This constant factor leads us directly to the problem of normalization. Similar to a plane wave propagating through an empty space, also the wave function for the Kronig-Penney model cannot be normalized in the sense that the integration over the probability density  $|\Psi(x)|^2$  should give exactly one. Instead the vector  $(a_n, b_n, c_n, d_n)^T$  is normalized.

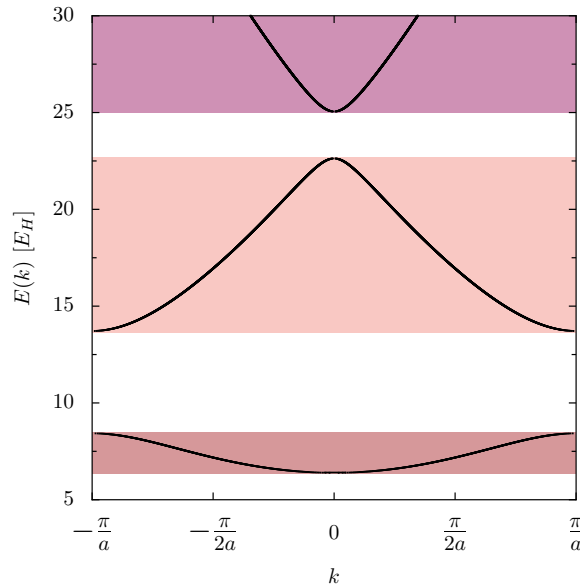


Figure 4.3: Band structure of the Kronig-Penney model according to Fig. 4.2, i.e. with the values  $V = 10$ ,  $a = 1.1$  and  $d = 0.8$ .

In Fig. 4.4 two wave functions for different energies are shown. The set of parameters leading to these wave functions is the same as in Fig. 4.2. The x-axis labels the position in real space over the range of one lattice constant (i.e.  $a = 1.1$ ). Within this range there is the region of finite potential, going from  $x = 0$  to  $x = 0.8$  (i.e. the width of the potential barrier  $d = 0.8$ ) and the region of free propagation, going from  $x = 0.8$  to  $x = 1.1$ .

In the left panel of Fig. 4.4 the eigenenergy is smaller than the barrier height, which leads to a decrease of the probability density in the middle of the barrier at  $x = 0.4$ . In the right panel the eigenenergy is higher than the potential barrier which leads to a plane wave behavior along the whole crystal. What is meant by that is that the exponential functions in Eq. (4.2) become plane waves, as the parameter  $\lambda$  becomes imaginary according to Eq. (4.4). Note that only the probability density is periodic, whereas the real and imaginary part of the wave functions are not. This is a direct consequence of Bloch's theorem. An interesting observation for the high-energy wave function is the flatness of the probability density in the area of free propagation. The reason for the flat probability density is the (almost) vanishing of one of the plane wave coefficients  $a_n$  or  $b_n$ . In this case  $b_n$  is significantly smaller than  $a_n$  which results in a very shallow oscillation of the probability density because it is dominated by the absolute value of  $a_n e^{iqx}$ . In the region of finite potential between  $x = 0$  and  $x = 0.8$  the oscillation of the probability density is much stronger, which corresponds to coefficients  $c_n$  and  $d_n$  of similar magnitude.

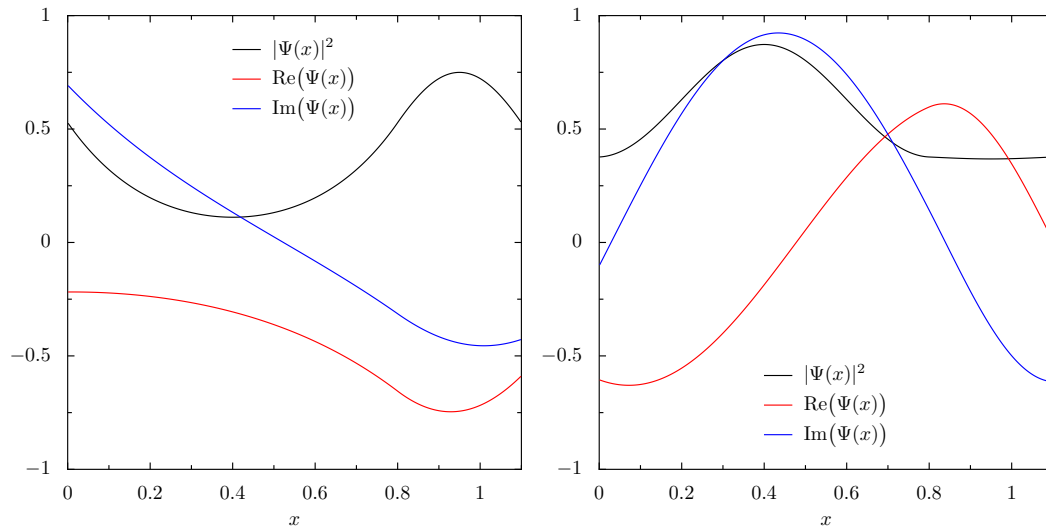


Figure 4.4: Two wave functions for the Kronig-Penney model as in Fig. 4.2 and Fig. 4.3. For  $x < 0.8$ :  $V(x) = 10$  and for  $0.8 < x < 1.1$ :  $V(x) = 0$ .  
 Left: energy  $E = 7.5$  in the middle of the first band,  $k$  positive.  
 Right: energy  $E = 17.5$  in the middle of the second band,  $k$  positive.

## 4.2 The Transfer Matrix Method

In this section I want to present the transfer matrix method for calculating the transmission in the Kronig-Penney model. The following derivation is based on the book by MARKOŠ and SOUKOULIS [91]. The goal is to implement a transport problem analogous to the one mentioned in the second chapter (see. Fig. 3.1). This means that we have two identical leads represented as a Kronig-Penney model on both sides of the scattering region, which is a single box-shaped potential barrier. A scheme of this transport setup is shown in Fig. 4.5. On the left side there is a unit cell of the leads exactly as in Fig. 4.1, followed by an empty space of arbitrary length  $f_l$ . Then we have a single potential barrier of height  $U$  and width  $\delta$ , which is again followed by an empty space of the length  $f_r$ . After the second empty space the next unit cell of the right lead begins, according to the definition of the unit cell in Fig. 4.1, with a potential barrier. If the left empty space region vanishes,  $f_l = 0$ , the height of the scattering barrier is chosen to be  $U = V$ , and the right side empty space is assigned the length  $f_r = a - d$ , Fig. 4.5 would be identical to Fig. 4.1 of the unperturbed Kronig-Penney model. In that case there is no real scattering, as the “scattering region” has the same structure as the leads, which should lead to a transmission coefficient of 1. This property of the scattering region shall be referenced later in this chapter.

The first step in the transfer matrix method is to calculate the effect of a single potential barrier on an incoming plane wave. This is important because the transfer matrix, per definition, maps the wave function on the left side of the barrier onto the wave function on the right side of the barrier. Therefore let us consider the potential barrier in the scattering region, isolated from the rest and assume the solution of the Schrödinger equation to consist of plane waves on both sides of the barrier and a

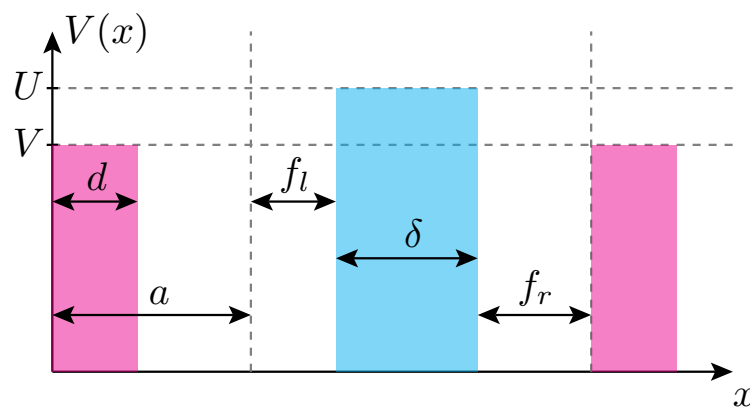


Figure 4.5: Scheme of the transport problem in the Kronig-Penney model with a scattering region consisting of a single potential barrier and variable distance to the leads.

linear combination of exponential functions in between as depicted in Fig. 4.6. The ansatz for the wave function is as follows:

$$\Psi(x) = \begin{cases} Ae^{iqx} + Be^{-iqx}, & x \leq 0 \\ Ee^{\kappa x} + Fe^{-\kappa x}, & 0 < x < \delta \\ Ce^{iqx} + De^{-iqx}, & \delta \leq x \end{cases} . \quad (4.11)$$

When the energy of the wave is smaller than the height of the barrier the parameter  $\kappa$  is a real number, and if it is higher,  $\kappa$  becomes imaginary. The wave function must be continuous and differentiable at both sides of the barrier,  $x = 0$  and  $x = \delta$ , which leads to four equations:

$$A + B = E + F \quad (4.12)$$

$$iqA - iqB = \kappa E - \kappa F \quad (4.13)$$

$$Ce^{iq\delta} + De^{-iq\delta} = Ee^{\kappa\delta} + Fe^{-\kappa\delta} \quad (4.14)$$

$$iqCe^{iq\delta} - iqDe^{-iq\delta} = \kappa Ee^{\kappa\delta} - \kappa Fe^{-\kappa\delta} . \quad (4.15)$$

These four equations contain a total of six variables, which means two of them must be eliminated. Those two variables are  $E$  and  $F$ , i.e. the coefficients of the exponential functions (plane waves) within the potential barrier. Because the first two equations are decoupled from the second two equations it is possible to express  $E$  and  $F$  in terms of  $A$  and  $B$ . Multiplying the first equation with  $\kappa$  and simply adding/subtracting the second equation leads to,

$$2\kappa E = \kappa(A + B) + iq(A - B) \quad (4.16)$$

$$2\kappa F = \kappa(A + B) - iq(A - B) . \quad (4.17)$$

These expressions can be easily inserted into the Eq.(4.14) when it is multiplied

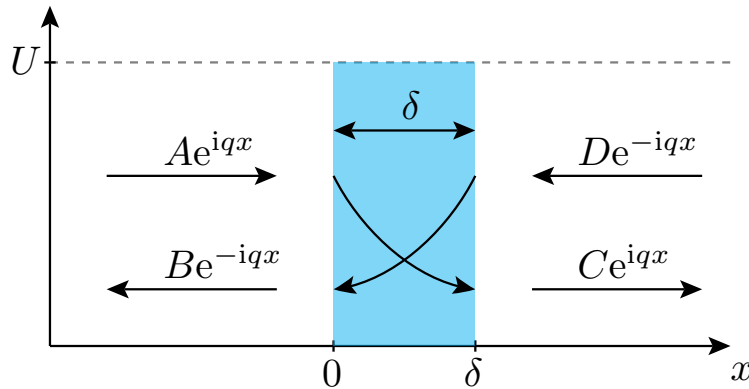


Figure 4.6: Scheme of the scattering process of a plane wave at a single potential barrier.

by  $2\kappa$  and in Eq. (4.15) when it is multiplied by 2. This leads to two equations that only contain  $A, B, C$  and  $D$ :

$$2\kappa C e^{iq\delta} + 2\kappa D e^{-iq\delta} = \left( \kappa(A+B) + iq(A-B) \right) e^{\kappa\delta} + \left( \kappa(A+B) - iq(A-B) \right) e^{-\kappa\delta} \quad (4.18)$$

$$2iq C e^{iq\delta} - 2iq D e^{-iq\delta} = \left( \kappa(A+B) + iq(A-B) \right) e^{\kappa\delta} - \left( \kappa(A+B) - iq(A-B) \right) e^{-\kappa\delta}. \quad (4.19)$$

In the next step these two equations must be transformed in such a way that on left side we either have  $C e^{iq\delta}$  or  $D e^{-iq\delta}$ . This is done by multiplying the first equation with  $iq$  and the second equation with  $\kappa$  and then adding/subtracting the equations:

$$4iq\kappa C e^{iq\delta} = \left( \kappa^2(A+B) + 2iq\kappa A - q^2(A-B) \right) e^{\kappa\delta} + \left( q^2(A-B) + 2iq\kappa A - \kappa^2(A+B) \right) e^{-\kappa\delta} \quad (4.20)$$

$$4iq\kappa D e^{-iq\delta} = - \left( q^2(A-B) - 2iq\kappa B + \kappa^2(A+B) \right) e^{\kappa\delta} + \left( q^2(A-B) + 2iq\kappa B + \kappa^2(A+B) \right) e^{-\kappa\delta}. \quad (4.21)$$

In the last step the terms on the right sides of both equations must be arranged according to their proportionality to  $A$  and  $B$ . The sums and differences of the exponential functions are then expressed as hyperbolic functions. Division by  $4iq\kappa$  for both equations finally leads to:

$$C e^{iq\delta} = \left[ \frac{i}{2} \left( \frac{q}{\kappa} - \frac{\kappa}{q} \right) \sinh(\kappa\delta) + \cosh(\kappa\delta) \right] A - \left[ \frac{i}{2} \left( \frac{q}{\kappa} + \frac{\kappa}{q} \right) \sinh(\kappa\delta) \right] B \quad (4.22)$$

$$D e^{-iq\delta} = \left[ \frac{i}{2} \left( \frac{q}{\kappa} + \frac{\kappa}{q} \right) \sinh(\kappa\delta) \right] A + \left[ \frac{i}{2} \left( \frac{\kappa}{q} - \frac{q}{\kappa} \right) \sinh(\kappa\delta) + \cosh(\kappa\delta) \right] B. \quad (4.23)$$

This gives us directly the transfer matrix, which is as previously mentioned defined as the matrix that maps the wave function on the left side of the barrier to the wave function on the right side of the barrier:

$$\begin{pmatrix} \Psi^+(x=\delta) \\ \Psi^-(x=\delta) \end{pmatrix} = M \begin{pmatrix} \Psi^+(x=0) \\ \Psi^-(x=0) \end{pmatrix}. \quad (4.24)$$

Since we identify  $\Psi^+(x=\delta) = C e^{iq\delta}$  and  $\Psi^+(x=0) = A$  (other components respectively), we identify the transfer matrix as,

$$M = \begin{pmatrix} \frac{i}{2} \left( \frac{q}{\kappa} - \frac{\kappa}{q} \right) \sinh(\kappa\delta) + \cosh(\kappa\delta) & -\frac{i}{2} \left( \frac{q}{\kappa} + \frac{\kappa}{q} \right) \sinh(\kappa\delta) \\ \frac{i}{2} \left( \frac{q}{\kappa} + \frac{\kappa}{q} \right) \sinh(\kappa\delta) & \frac{i}{2} \left( \frac{\kappa}{q} - \frac{q}{\kappa} \right) \sinh(\kappa\delta) + \cosh(\kappa\delta) \end{pmatrix}. \quad (4.25)$$

The matrix in Eq. (4.25) is the transfer matrix for a single potential barrier with width  $\delta$  and height  $U$  and shall thus be referred to as  $M(\delta, U)$  from now on. This

is the potential barrier in the scattering region as seen in Fig. 4.5. In order to calculate the transmission in this transport setup, however, it is also important to include the leads. Therefore we also need the transfer matrix  $M(d, V)$  for one of the potential barriers inside the leads. Since the calculation for  $M(d, V)$  is identical to the calculation for  $M(\delta, U)$ , we easily get  $M(d, V)$  by replacing  $\delta \rightarrow d$  and  $U \rightarrow V$ . Additionally we need transfer matrices for the free propagation of the plane waves in between the potential barriers. Since the free propagation is only a multiplication with a phase factor, the corresponding transfer matrices have the form,

$$M_f(l) = \begin{pmatrix} e^{iq l} & 0 \\ 0 & e^{-iq l} \end{pmatrix}, \quad (4.26)$$

where  $f$  implies “free propagation” and  $l$  is the length of the interval. With that, we write the transfer matrix for one entire unit cell of the leads as a product of two transfer matrices:

$$M_L = M_f(a - d)M(d, V). \quad (4.27)$$

Since a unit cell of the leads “begins” with a potential barrier,  $M(d, V)$  is on the right side and  $M_f(a - d)$  is on the left side, which causes  $M(d, V)$  to act first. The same has to be done for the entire scattering region, which results in a total transfer matrix of the form:

$$M_S = M_f(f_r)M(\delta, U)M_f(f_l). \quad (4.28)$$

The transfer matrix of the leads has then to be diagonalized using a unitary transformation:

$$Q^{-1}M_LQ = \begin{pmatrix} e^{ika} & 0 \\ 0 & e^{-ika} \end{pmatrix}. \quad (4.29)$$

The  $k$  on the right side of the equation is the same parameter as in Bloch’s theorem Eq. (4.5). This is seen if one calculates the eigenvalues of the  $2 \times 2$  matrices on both sides, adds them up, and divides by 2. For the right side, this would lead to  $\cos(ka)$  and for the left side one would get the right side of the transcendental equation Eq. (4.9). The transmission coefficient can now be calculated by multiplying the eigenbasis of the leads’ transfer matrix onto the transfer matrix of the scattering region. The complex transmission amplitude is then the inverse of the 22 (bottom right) matrix element of the resulting matrix. The transmission coefficient  $T$  we are interested in is given by the squared absolute value of the complex transmission amplitude:

$$T = \left| [Q^{-1}M_SQ]_{22} \right|^{-2}. \quad (4.30)$$

The energy dependence of the transmission comes from  $q$ ,  $\lambda$  and  $\kappa$  as in Eq. (4.3) and Eq. (4.4) which appear in  $Q$  as well as in  $M_S$ . Going back to the end of the opening paragraph of this section, we see that if the scattering region is identical to the leads, the eigenbasis  $Q$  of the leads will also diagonalize  $M_S$  which automatically leads to a transmission of  $T = 1$  for all energies.

### 4.3 A Toy Model for Half-Metallic Transport

In this section we want to use the formalism of the previous two sections to discuss a toy model for a half-metallic transport problem. The assumption is that there are two spin channels, i.e., electrons behave differently depending on their spin direction. These spin channels are represented by two different Kronig-Penney potentials that have the same lattice constant  $\alpha$ . By changing the barrier width and height, the goal is to obtain two band structures where, around some energy, one of them has a band gap and the other one does not. The Fermi level is then chosen to be inside the band gap. Another important aspect is that the lead dispersion must not have a band gap at the Fermi level of the scatterer or else there would be no transport at all. In Fig. 4.7 the scheme of the half-metallic transport setup is shown. The leads are described by the potential barrier width  $d$ , the lattice constant  $a$  and the barrier height  $V$ . In the scattering region, the majority spin channel (depicted in red) is defined by the potential barrier width  $\delta_\uparrow$  and height  $U_\uparrow$ , whereas the minority spin channel (depicted in blue) is described by  $\delta_\downarrow$  and  $U_\downarrow$  respectively. Since there are no additional empty spaces between the last unit cell of the left lead and the scattering region and between the scattering region and the right lead, the transfer matrix of the whole scattering region for the majority spin channel is of the form,

$$M_\uparrow = \left( M_f(\alpha - \delta_\uparrow) M(\delta_\uparrow, U_\uparrow) \right)^n, \quad (4.31)$$

where  $n$  is the number of unit cells in the scattering region. For the transfer matrix of the minority spin channel simply replace  $\delta_\uparrow$  with  $\delta_\downarrow$  and  $U_\uparrow$  with  $U_\downarrow$ . Now the parameters that are given in Fig. 4.7 must be used for the band structure calculation

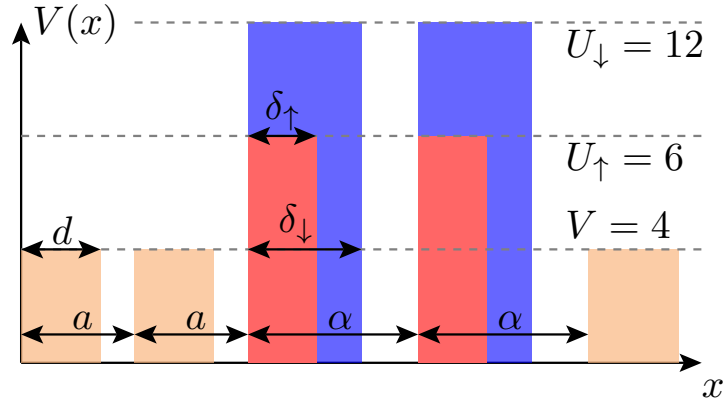


Figure 4.7: Scheme of the half-metallic transport problem in the Kronig-Penney model with a scattering region consisting of two different potentials for the two separate spin channels. Parameters for the leads:  $a = 1.0$  and  $d = 0.8$ . Parameters for the scattering region:  $\delta_\uparrow = 0.2$ ,  $\delta_\downarrow = 0.8$  and  $\alpha = 1.5$ .

of a Kronig-Penney model separately for the leads and both spin channels of the scattering region. The resulting band structures, which are shown in Fig. 4.8, can then be compared with each other to see if they satisfy the conditions mentioned at the beginning of this section.

The Fermi level in Fig. 4.8 was defined to be in the middle of the band gap of the minority spin channel, which corresponds to  $E_F = 16$ . This value will become relevant again later on. What we see is that the majority spin band shows a linear dispersion in the same energy range where the minority spin band has a gap. The band of the leads stretches across an energy window that includes the minority spin gap as well as the entire majority band. A closer look at Fig. 4.8 reveals that the lead band width exceeds the boundaries of the Brillouin zone of the two spin channels of the scattering region. This is due to the different lattice constants in the two sub-systems. While the lattice constant in the scattering region is  $\alpha = 1.5$ , the lattice constant in the leads is only  $a = 1.0$  which results in a larger Brillouin zone. Since the band structures of the leads and the spin channels satisfy the conditions for a simple half-metallic model, the next step is to calculate the energy-dependent transmission  $T(E)$  for each spin channel. In the simplest situation the scattering region consists of a single unit cell, i.e. a single potential barrier followed by an empty space of certain length.

The resulting transmission is shown in Fig. 4.9. The majority spin channel is depicted in red, whereas the minority spin channel is depicted in blue. This standard is kept throughout the rest of the thesis. For both spin channels we see energy ranges

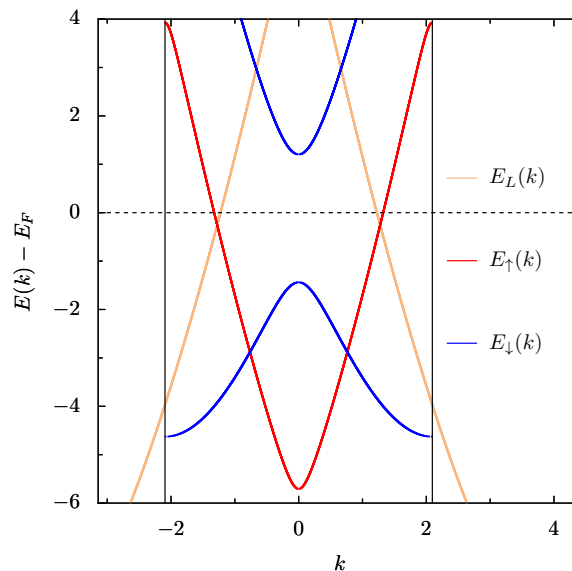


Figure 4.8: Band structures for the leads and the two spin channels of the (periodically repeated) scattering region. The vertical black lines show the borders of the scattering region's Brillouin zone.

where the transmission goes to zero. These energy ranges are marked with beige color and are the same for both channels. The reason for the drop of the transmission in these areas lies in the leads. At those energies, the band structure of the leads has gaps. This means that no wave with an energy within that gap can move unhindered through the leads. Since no wave of such an energy can arrive, there is no scattering which in turn causes the transmission to vanish. For future transmission plots we will therefore confine the considered energy range to an area around the Fermi level, small enough to not be intersected by the leads' band gaps. Another highlighted energy window can be found in the plot for the minority spin channel. There, depicted in light blue, lies the half-metallic band gap of the minority spin channel. The minority spin channel also has other band gaps which were not highlighted in this figure and so does the majority spin channel. An immediate observation is that the transmission shows no interesting features within that energy range. The reason for the absence of any features in that energy range is the simplicity of the chosen model. With only one unit cell of the “half-metal” within the scattering region, the structure is simply too small to develop a band-like behaviour.

Therefore the band structure picture from Fig. 4.8 does not really make sense in this example. An obvious difference in the transmission for the two spin channels can be seen in the energy range of the first and the second leads bands. When we look at the first leads band, which can be found between  $E - E_F = -13$  and  $E - E_F = -8$  we see that for the majority spin channel the transmission increases extremely fast to a value close to 1, whereas the transmission for the minority spin channel stays extremely low and does not even exceed a value of 0.1. The reason for this lies in the band structure of the two spin channels. The majority spin band in that energy

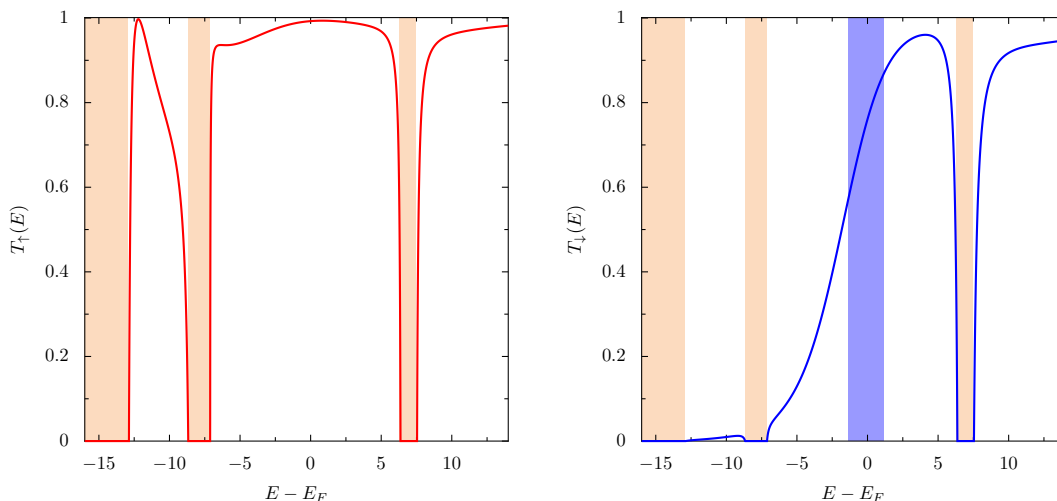


Figure 4.9: Transmission coefficients for the two different spin channels for the case of one unit cell in the scattering region. Colored areas represent band gaps of the leads (beige) and of the minority spin channel (blue).

range is quite extended and covers most of the leads band, whereas the minority spin band is extremely flat, as it covers the energy range from  $E - E_F \in [-12.5, -12]$ .

The situation already looks different when a second unit cell of the “half-metal” is added to the scattering region. Figure 4.10 shows the transmission of both spin channels for a narrower energy window that spans over the second leads band. In addition to the half-metallic gap for the minority spin channel at the Fermi level, this figure also shows another band gap in the minority spin channel at low energies as well as two gaps in the majority spin channel far away from the Fermi level at low and high energies. When we look at the majority spin channel we see a picture that looks very similar to the previous case with only one unit cell. The small plateau that forms around  $E - E_F = -7$  is already lower than before. In the previous case we found that plateau above  $T_{\uparrow} = 0.9$  and now it is slightly below  $T_{\uparrow} = 0.8$ . When we approach the upper edge of the leads band we also see that the decrease of the transmission is much faster than in the previous case. This energy region also concurs with a majority spin band gap. The region around the Fermi level on the other hand shows a very high transmission in general, which is in accordance with the results of the previous case.

The really interesting differences to the previous case come with the minority spin channel. In the considered energy range we have two band gaps. The first one at the lower energies and the second one around the Fermi level. When we consider the first band gap we see that the transmission stays at a very low level and undergoes a strong increase once the energy enters the band of the minority spin channel. This feature was not visible in the last case. When we consider the second gap, the Fermi gap so to say, we also see a reduction of the transmission. An interesting observation

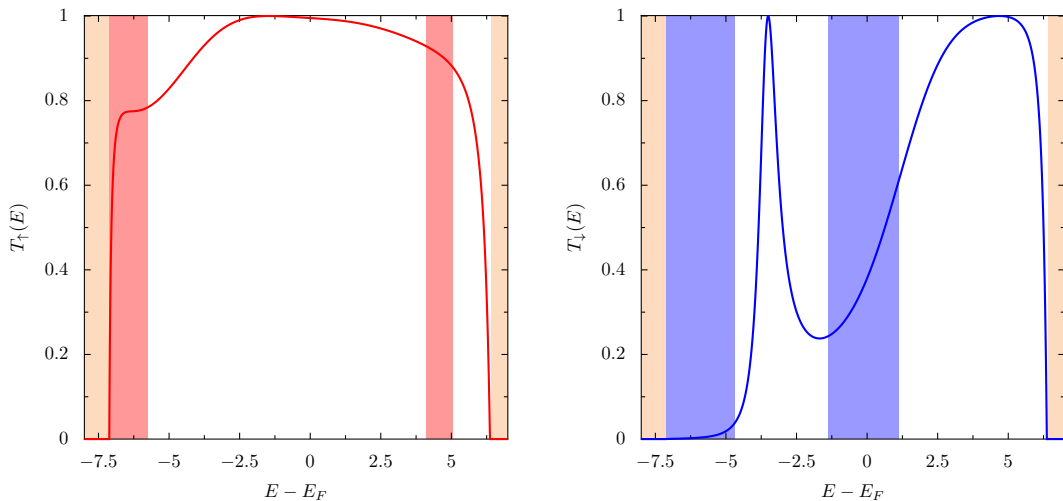


Figure 4.10: Transmission coefficients for the two different spin channels for the case of two unit cells in the scattering region. Rudiments of the band character are already visible

is that the minimum of the transmission does not appear inside the Fermi gap, but slightly below. The high energy part of the transmission, at the right of the Fermi band gap, looks very much like in the single barrier case. For the lower energies at the left of the Fermi band gap however, we get a completely different picture. There is now a peak in the transmission that we did not even see a hint of in the previous case. Calculations for different leads, varying in lattice constant  $a$ , barrier width  $d$ , and also barrier height  $V$ , have shown that the position of this peak with respect to the energy is independent from the leads potential.

In this paragraph we want to explore the origin of this peak in the transmission. Since the position is independent of the leads, the easiest approach is to isolate the scattering region from the leads and trying to find characteristic energy values that match the position of the peak. The requirements for the wave function of this isolated problem are continuity and differentiability at four different points, namely the edges of the two barriers. The two conditions per point yield a total of 8 equations. There are however five areas to cover, the two barriers, the two semi-infinite spaces left and right of the two barriers as well as the small space in between the barriers. If each area is described with a wave function that consists of two plane waves, one moving to the right, the other one moving to the left, we would end up with ten variables. We thus have to remove two of those variables, as is shown in Fig. 4.11. Since the transmission at the considered energy is equal to one, the idea is to remove the left moving plane waves from the semi-infinite areas, because that would describe the situation where an incoming plane wave is

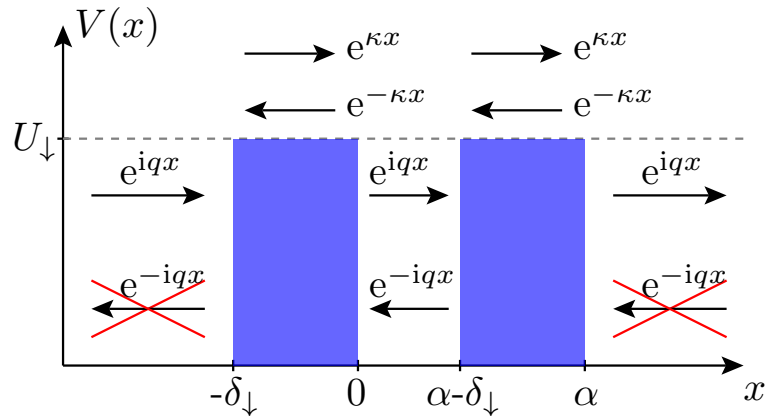


Figure 4.11: Isolated scattering region consisting of two potential barriers.

completely transmitted. For the wave function, we have thus the following ansatz:

$$\Psi(x) = \begin{cases} Ae^{iqx}, & x \leq -\delta_{\downarrow} \\ Ce^{\kappa x} + De^{-\kappa x}, & -\delta_{\downarrow} < x < 0 \\ Ee^{iqx} + Fe^{-iqx}, & 0 \leq x \leq \alpha - \delta_{\downarrow} \\ Ge^{\kappa x} + He^{-\kappa x}, & \alpha - \delta_{\downarrow} < x < \alpha \\ Ie^{iqx}, & \alpha \leq x \end{cases}, \quad (4.32)$$

where the coefficients  $B$  and  $J$  were set to zero (as in Fig. 4.11). The eight continuity and differentiability conditions form a homogeneous system of equations where the variables are the coefficients of the plane waves. The matrix  $K$  that describes this system of equations depends on  $q$  and  $\kappa$  which are themselves both energy dependent. Therefore we can write,

$$K(E) (A, C, D, E, F, G, H, I)^T = \mathbf{0}. \quad (4.33)$$

Similar to Eq. (4.8), we can only find a non-trivial solution if the determinant of this matrix vanishes. Since the matrix  $K$  is  $8 \times 8$  it is suggested to calculate the determinant numerically. The roots of the determinant can be detected graphically by plotting  $\det(K(E)) + 1$  versus  $E - E_F$ . It is shown in Fig. 4.12 that the position of the peak in the transmission aligns perfectly with one of the local minima of the logarithmic determinant. This means that the peak originates from an eigenstate of the isolated problem described in Fig. 4.11. This answer however leads us straight towards the next question. At  $E - E_F = -4$ , just below the energy value that corresponds to the single peak in the transmission, we find another local minimum in the

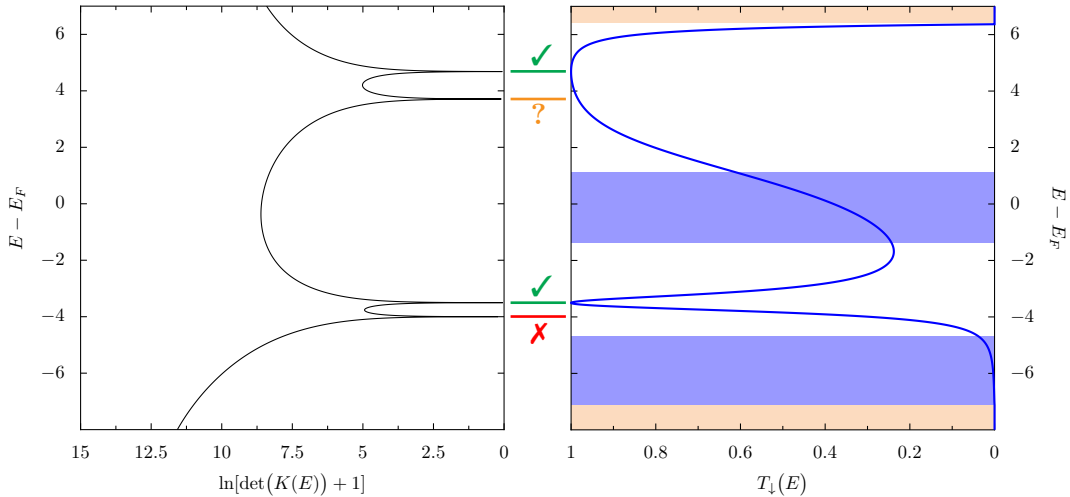


Figure 4.12: Comparison of the logarithmic determinant of  $K(E)$  with the corresponding transmission (both turned sideways). Some of the peaks in the logarithmic determinant align with the local maxima of transmission, whereas some others do not.

logarithmic determinant. Surprisingly nothing special happens in the transmission plot at that specific energy. It is instructive to investigate in the following the origin of this phenomenon.

At  $E - E_F = -4$  the matrix  $K$  becomes singular, which means in the kernel of  $K(E)$  we find two linear independent vectors, which are given by:

$$(A_1, C_1, D_1, E_1, F_1, G_1, H_1, I_1)^T = (0, z, -z, 0, 0, 0, 0, 0)^T \quad (4.34)$$

$$(A_2, C_2, D_2, E_2, F_2, G_2, H_2, I_2)^T = (0, 0, 0, 0, 0, z, -z, 0)^T, \quad (4.35)$$

where  $z$  is a complex number with absolute value  $\frac{1}{\sqrt{2}}$ . In order to understand these results it is important to remember the value of the Fermi level, which was set to  $E_F = 16$ . When we now consider the position of the peak  $E - E_F = -4$  we find that the energy of the wave function is  $E = 12$ , which is exactly the height of the potential barrier. This is a crucial point because the parameter  $\kappa$ , which is energy dependent (also see Eq.(4.4)), becomes zero when the energy of the wave equals the height of the potential. This has the consequence that we get  $ze^0 - ze^{-0} = 0$  for the considered part of the wave function, which, together with the other coefficients, sets the whole wave function to zero. Hence in this particular case the peak in Fig. 4.12 indicates the deficiency of the wave function representation rather than a physical meaning. For the aforementioned peak in the transmission at a slightly higher energy however we get a non-zero wave function that is shown in Fig. 4.13.

Another interesting energy lies just below  $E - E_F = 4$ , where we see a clearly defined peak in the logarithmic determinant (Fig. 4.12), which is not distinctly identifiable in the transmission plot. A vanishing wave function, just like in the other case, can be ruled out since that is only possible if  $E - E_F$  is either -4 or -16. In

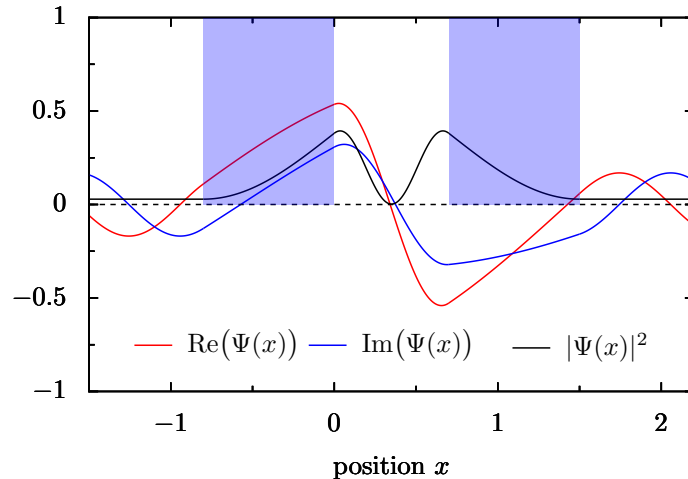


Figure 4.13: Wave function of the double barrier scattering problem in Fig. 4.11, corresponding to the peak in the transmission in Fig. 4.12 slightly above  $E - E_F = -4$ . Blue areas depict the position of the potential barriers.

Fig. 4.14 the wave function for the isolated scattering process is shown. The biggest difference between Fig. 4.13 and Fig. 4.14 can be found in the area between the potential barriers. Here, the probability density in that region is constant which corresponds to the situation where one of the coefficients of the plane waves in that region is zero. In this case it is the coefficient of the left-moving wave, so that the wave function in the area between the two barriers has the same form as in the areas on the left and the right of the barriers. For the areas inside the barriers the parameter  $\kappa$  is complex since the energy of the wave is higher than the potential barrier. The wave function in that area is thus a superposition of plane waves with a non-zero coefficient for each direction. This however is not enough to explain why there is no distinct peak in the transmission at the corresponding energy.

A huge difference between the wave function of Fig. 4.14 and the transmission plot in Fig. 4.10 is the inclusion of the leads. While the wave function was calculated for the isolated scattering region, the transmission used the eigenbasis of the lead's transfer matrix. It is therefore not surprising that the leads have an influence on the visibility of those peaks in the transmission plot. In order to understand why this peak is not clearly visible we need to take into account the wave function that is a right moving solution of the left lead's Schrödinger equation. This wave function is depicted in the left panel of Fig. 4.15 and has to be compared with the wave function of the isolated scattering problem (Fig. 4.14) **and** with the wave function and corresponding isolated scattering problem corresponding to the peak above  $E - E_F = -4$ , which can be found in the right panel of Fig. 4.15 and in Fig. 4.13, respectively. Let us first consider the single peak in the transmission just above  $E - E_F = -4$ . When we look at the wave function of corresponding energy inside

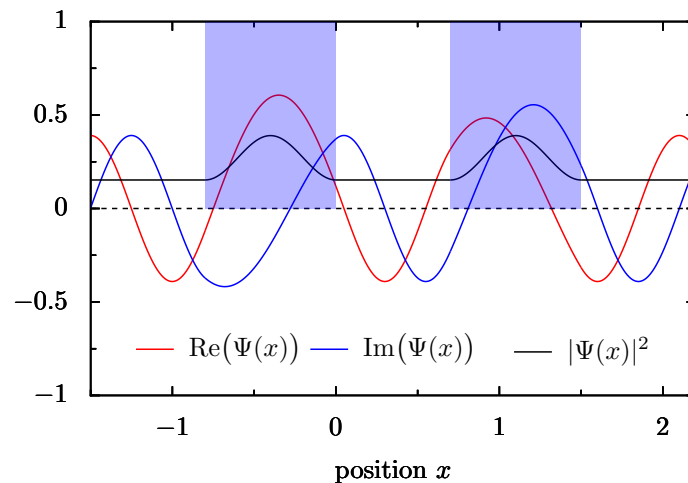


Figure 4.14: Wave function of the double barrier scattering problem in Fig. 4.11, corresponding to peak in the transmission in Fig. 4.12 slightly below  $E - E_F = 4$ . Blue areas depict the position of the potential barriers.

the leads, we see that the probability density is very flat outside the potential barrier (Fig. 4.15, right), which corresponds to the coefficient of the left-moving plane wave being almost zero.

Going back to the setup of the transport problem in Fig. 4.7 we see that this area is the one that makes contact to the scattering region. This means that the wave function that is coming from the left lead has basically the same properties as the wave function that was assumed in the isolated scattering process (Fig. 4.11). This leads to a very high transmission at that specific energy. On the other hand, when we consider the peak in the logarithmic determinant just below  $E - E_F = 4$  the corresponding wave function in the lead (Fig. 4.15, left) has a significant contribution of the left-moving plane wave outside of the potential barrier. This contribution can be seen in the rather strong oscillation of the probability density compared to the picture on the right. The actual wave function that comes from the lead is thus not well described by the isolated scattering problem. Therefore, the transmission is also not as high as in the other case which explains why we do not see a peak in the transmission that goes up to one. We can summarize these findings in the statement that the isolated scattering problem is suitable for predicting peaks in the transmission, but not necessarily their height. This becomes especially clear if the predicted peak falls into a band gap of the leads, where the transmission is always zero. Similar results were lately found by EISENBACH *et al.*, who investigated anomalies in transmission resonances for one-dimensional disordered quantum systems in a tight-binding approximation [92]. They found that resonances in the scatterer can be suppressed, depending on the coupling to the leads.

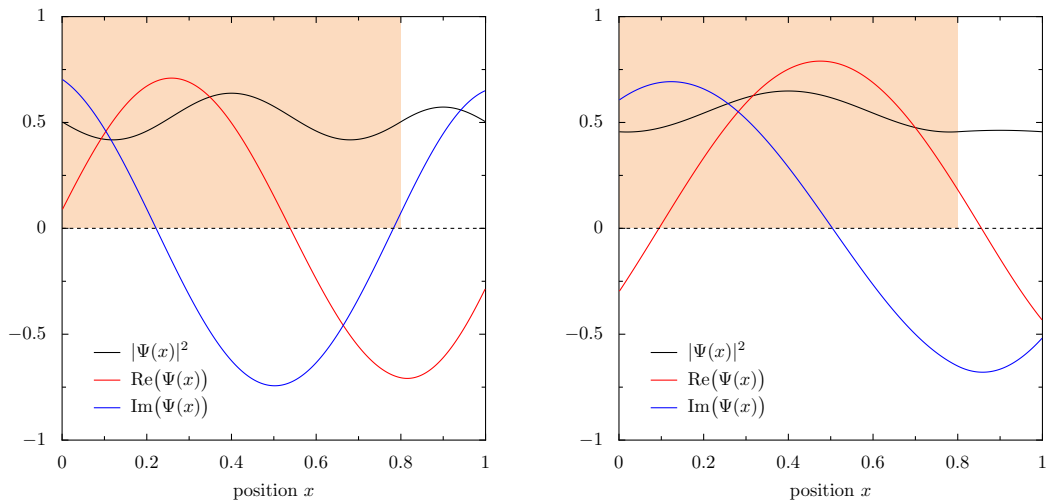


Figure 4.15: Wave functions in the leads corresponding to the energies slightly below  $E - E_F = 4$  (on the left) and slightly above  $E - E_F = -4$  (on the right). The beige area depicts the position of the potential barrier in the leads.

Now that the peaks in the transmission function can be explained, the next step is to add more unit cells to the scattering region in order to determine how strongly the transmission drops in the supposed band gap. In Fig. 4.16 the transmission for both spin channels is shown when there are five unit cells of the “half-metal” in the scattering region. A quick look onto the valence band (the white area left of the Fermi level) of the minority spin channel reveals four peaks. These four peaks correspond to the four potential wells that are formed by five potential barriers, just like the two potential barriers formed a single well corresponding to a single peak. The bulk-like character of the scattering region is now quite pronounced which can especially be seen in the minority spin channel. The transmission in the Fermi gap is much smaller than it was found for two unit cells. Also the transmission for the band gap below the valence band is more suppressed than in the previous case.

The majority spin channel shows similar effects, yet not in the same magnitude. The transmission around the majority spin band gaps around  $E - E_F = -6$  and just below  $E - E_F = 5$  are smaller than in the calculation using only two unit cells, but not nearly as suppressed as for the minority spin channel. A reason for this difference is the size of the band gaps of the two spin channels. Because the majority spin potential barriers in our model were assigned only half the height of the minority spin barriers, the resulting band gap is also much smaller which causes the transmission to drop at a much lower rate with respect to the number of unit cells. The transmission for the majority spin band now also shows four local maxima inside the band around the Fermi level corresponding to the wells between the potential barriers. This is a new observation because for the previous two considered cases,

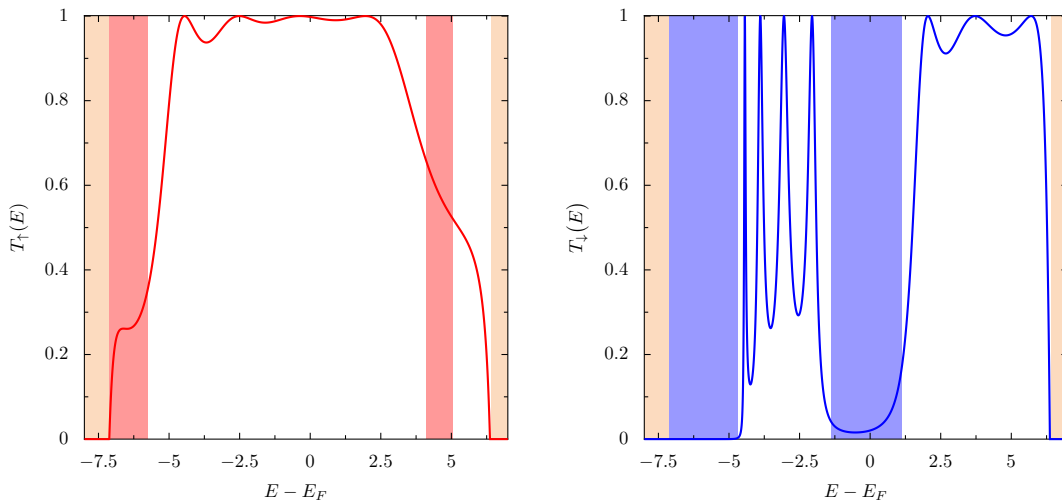


Figure 4.16: Transmission coefficients for the two different spin channels for the case of five unit cells in the scattering region. Coloured areas represent band gaps of the leads (beige) and of the majority (red) as well as the minority (blue) spin channel.

which were given by using one and two “half-metal” unit cells inside the scattering region, the resulting transmission plots looked almost identical, unlike the minority spin channel where suddenly the isolated peak in the transmission appeared.

When the number of unit cells in the scattering region is increased furthermore, the oscillations within the energy bands of the spin channels become stronger, as is shown in Fig. 4.17 for the case of 15 unit cells. For the majority spin channel, we count 14 local maxima within the band around the Fermi level. An interesting observation can be made in the majority spin channel at high energies above  $E - E_F = 5$ , where only one single peak is observed. There, we have the situation that the additional 13 peaks that are expected at least partly fall into the band gap of the lead (beige area) which suppresses their influence on the transmission and simply cuts them away. A similar behavior can be observed for the minority spin channel where in the conduction band above the Fermi level, we count only nine peaks. In both spin channels, slightly below the band edge of the lead we see that the transmission is abruptly changing its monotony. This can be explained with the missing peaks. If the band of the leads did not end at that energy, the transmission would again peak due to the resonance which was found in the isolated scattering problem. However, the band edge of the leads forces the transmission to zero which causes the abrupt change of the slope.

The main question is, if the informations gathered from this toy model also apply in the more sophisticated non-equilibrium Green’s function calculation for real half-metallic compounds. The reason for the model calculations in this chapter is to

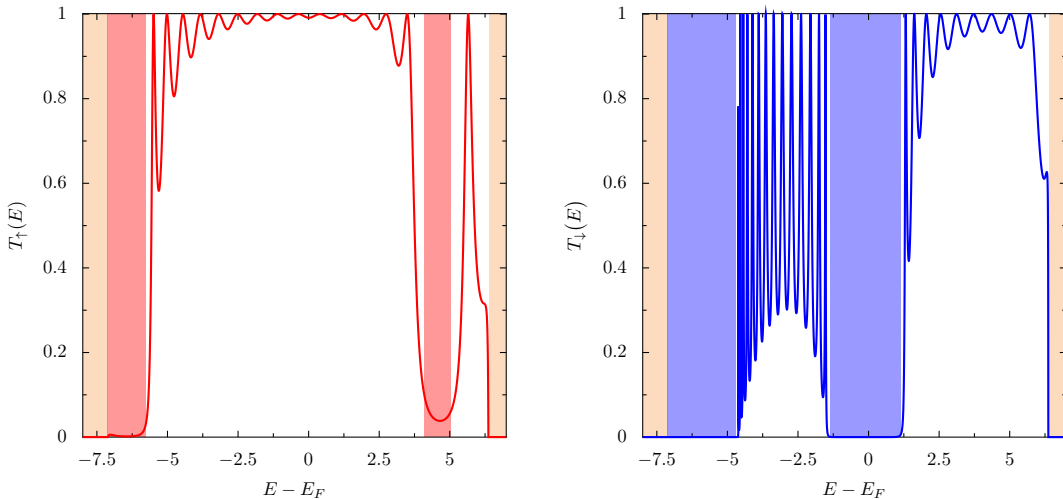


Figure 4.17: Transmission coefficients for the two different spin channels for the case of fifteen unit cells in the scattering region. Now the band gaps of each spin channel are clearly visible in the transmission plot. Some of the peaks now fall into the lead’s band gap.

find out how the minority spin transmission at the Fermi level is influenced by the number of unit cells (potential barriers) within the scattering region.

In Fig. 4.18, the (logarithmic) transmission is depicted, for different sets of parameters. The Fermi level for each set of parameters is defined such that it lies in the middle of the minority spin band gap. The solid curve represents the same parameters as in the last paragraphs ( $U_{\downarrow} = 12$ ,  $E_F = 16$ ,  $\Delta E = 2.64$ ), the dashed curve belongs to a lower potential with a narrower band gap ( $U_{\downarrow} = 10$ ,  $E_F = 14.5$ ,  $\Delta E = 1.84$ ) and the dashed-dotted curve represents a wider gap with a higher potential ( $U_{\downarrow} = 14$ ,  $E_F = 17$ ,  $\Delta E = 3.54$ ). Other parameters such as  $\delta_{\downarrow}$  and  $\alpha$  remained unchanged.

The linear behavior of the logarithmic transmission in the right panel of Fig. 4.18 indicates that the transmission decreases exponentially after the first few unit cells within the scattering region. The number of unit cells, after which the decay is strictly exponential, can be extracted from the kinks in the logarithmic transmission and depends on the size of the band gap  $\Delta E$ . For the narrow band gap, the transmission drops exponentially after five unit cells of the scatterer, whereas for the wide band gap we observe an exponential behavior already after the second unit cell.

The slope of the logarithmic transmission in Fig. 4.18 is determined by the complex band structure of the scattering region's minority spin channel. On one hand, there is Bloch's theorem, Eq. (4.5), and on the other hand, there is the transcendental equation (4.9), derived from Bloch's theorem. In the scheme for calculating the band structure, the third step is to check if the absolute value of the right-hand side

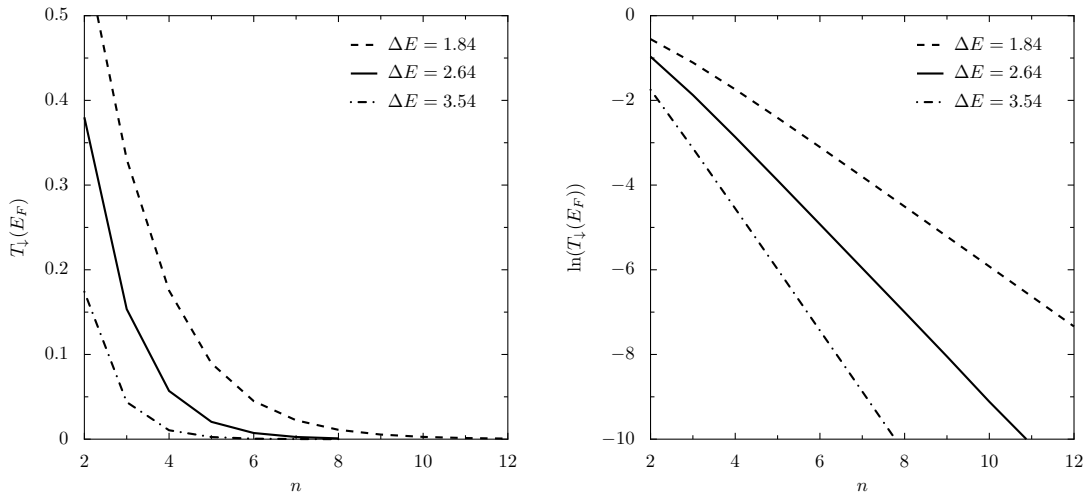


Figure 4.18: Left panel: Transmission coefficient at the Fermi energies for the minority spin channel in dependence of the number of unit cells (potential barriers) within the scattering region. Right panel: The logarithm of the transmission in order to emphasize the exponential decay.

of Eq. (4.9) is smaller or equal to one. Only then, it is possible to find a real  $k$  for the given energy. However, if the absolute value of the right-hand side of Eq. (4.9) is larger than one,  $k$  becomes imaginary (see Fig. 4.19). Inserted into Bloch's theorem, this imaginary  $k$  yields an exponential decay of the wave function. The functional dependence of the logarithmic transmission's slope  $m$  on the imaginary part of  $k$  at the Fermi level is as follows:

$$m = -2\alpha \operatorname{Im}(k(E_F)) \quad (4.36)$$

where  $\alpha$  is the scattering region's lattice constant. The factor 2 originates from the squared absolute value in Eq. 4.30. In our example, the imaginary part of the wave vector at the Fermi level is  $\operatorname{Im}(k(E_F)) \approx 0.347 a_0^{-1}$ , see Fig. 4.19. With a lattice constant of  $\alpha = 1.5 a_0$  we find,

$$m \approx -2 \cdot 1.5 a_0 \cdot 0.347 a_0^{-1} = -1.041. \quad (4.37)$$

This result agrees very well with the fitted slope  $m = -1.04$  that has been obtained from the corresponding numerically calculated logarithmic transmission (see solid line in Fig. 4.18).

At the end of chapter 6, the results of the non-equilibrium Green's function calculation with SMEAGOL will be compared with the results of this Kronig-Penney toy model calculation.

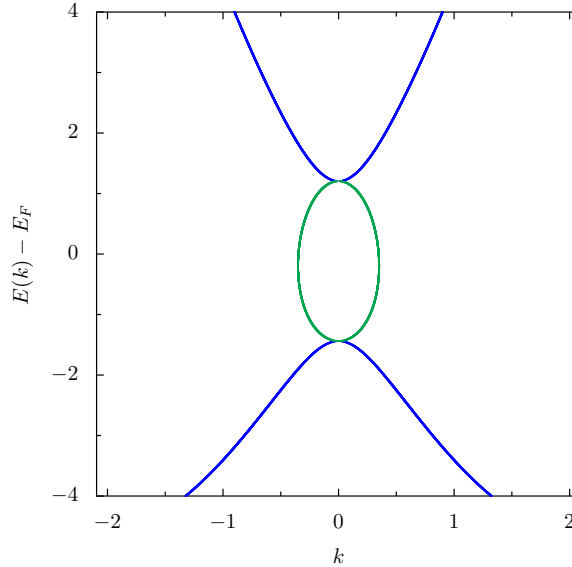


Figure 4.19: Minority spin band structure of the scattering region around the Fermi level. Blue line:  $k$  is real. Green line:  $k$  is imaginary.



# 5 Material and System Setup

## Contents

---

<b>5.1 About Heusler Alloys and NiMnSb . . . . .</b>	<b>67</b>
<b>5.2 The Transport Setup . . . . .</b>	<b>73</b>

---

In the beginning of this chapter a short overview over the structural and electronic properties of NiMnSb is given. The structural properties, especially the lattice constant, are calculated numerically with the SIESTA code and may deviate from experimental findings by a few percent. For the transport calculations, the SIESTA lattice constant was used instead of the experimental value in order to ensure the consistency of the whole calculation. In this context, consistency is seen as the commitment to the *ab initio* method, which must not be confused with the self-consistency inherent to the algorithms of density functional theory.

The topic of the second part of this chapter is the construction of the transport setup, which is then used in all of the calculations in the later chapters. This construction considers various possible interfaces and uses the SIESTA code to determine the most stable configuration.

## 5.1 About Heusler Alloys and NiMnSb

For a better understanding of this section, a short summary of the relevant parts of the introduction follows. Relevant in that sense are the structural properties of Heusler alloys, especially half-Heusler compounds.

As we already mentioned in the introduction, the family of Heusler materials can be divided into two main classes. On one hand, we have the full-Heusler alloys of the formula type  $X_2YZ$ , such as  $Cu_2MnAl$ , and on the other hand we have half-Heusler alloys of the form  $XYZ$  such as NiMnSb, the material whose transport properties are the topic of this thesis.

In the chemical formula  $XYZ$  of half-Heusler alloys, X and Y are transition metals and Z is an element of the III.-V. main-group. The Bravais-lattice of Heusler alloys is always face-centred-cubic (fcc). The crystal structures, which comprises the lattice (set of points) **and** the basis (set of atoms) differ between full and half-Heusler

alloys. For half-Heuslers, the structure consists of three interpenetrated fcc lattices (one for each atom type) and is denoted by  $C1_b$ .

A schematic picture of the unit cell in its cubic as well as primitive form is shown in Fig. 5.1. In that figure, the conventional unit cell according to the work of GALANAKIS *et al.* is presented [14]. Another prominent representation, where the positions of the respective atoms are shifted along the spacial diagonal of the unit cell, originates from the paper of DE GROOT *et. al.* [2].

In this structure positions of the Y and Z atoms are interchangeable which can be nicely seen in the left picture of Fig. 5.1. An exchange of the Y and Z positions is equivalent to a rotation of the structure by  $90^\circ$  around the z-axis, which means that the material and therefore all its properties do not change.

In order to represent the crystal of NiMnSb in a compact way, we choose the primitive lattice vectors, which, for a fcc lattice, are given by:

$$\vec{a} = \frac{a}{2} \begin{pmatrix} 1 \\ 1 \\ 0 \end{pmatrix}, \quad \vec{b} = \frac{a}{2} \begin{pmatrix} 1 \\ 0 \\ 1 \end{pmatrix} \quad \text{and} \quad \vec{c} = \frac{a}{2} \begin{pmatrix} 0 \\ 1 \\ 1 \end{pmatrix}, \quad (5.1)$$

where  $a$  is the lattice constant. One primitive unit cell of a half-Heusler alloy contains 3 atoms, forming the basis of the crystal. The atomic positions are: X  $(0, 0, 0)$ , Y  $(\frac{1}{4}, \frac{1}{4}, \frac{1}{4})$  and Z  $(\frac{3}{4}, \frac{3}{4}, \frac{3}{4})$ .

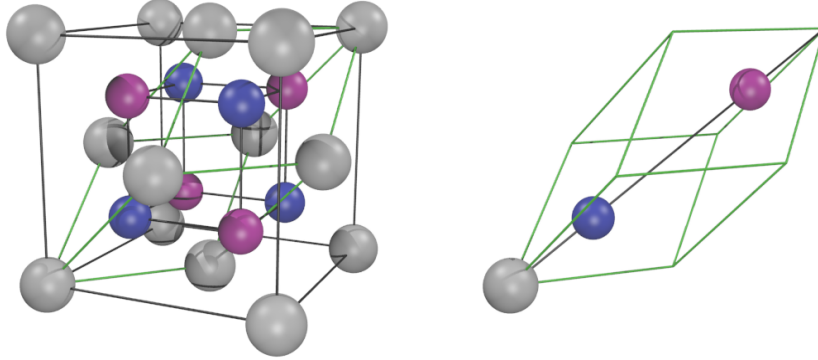


Figure 5.1: Visualization of the crystal structure of half-Heusler alloys. On the left: typical fcc representation as often seen in literature. Grey spheres symbolize X, blue and purple spheres represent Y and Z respectively. For future reference: **grey** = Ni, **blue** = Mn, **purple** = Sb. The primitive unit cell is enclosed by green conjunctions. On the right: isolated primitive unit cell containing only three atoms.

For the case of full-Heuslers there is also an atom of type X at the position  $(\frac{1}{2}, \frac{1}{2}, \frac{1}{2})$ . The volume of a primitive unit cell (which is a parallelepiped) is

$$\Omega = \left| \vec{a} \cdot (\vec{b} \times \vec{c}) \right| = \frac{a^3}{4}. \quad (5.2)$$

Heusler alloys may show some very interesting magnetic properties, for example  $\text{Cu}_2\text{MnAl}$  (full-Heusler) which was featured in HEUSLER'S work from 1903, shows a ferromagnetic behaviour although none of the elements this alloy consists of are ferromagnetic. The material we choose for our research is the half-Heusler alloy NiMnSb, which means we have the atomic positions Ni  $(0, 0, 0)$ , Mn  $(\frac{1}{4}, \frac{1}{4}, \frac{1}{4})$  and Sb  $(\frac{3}{4}, \frac{3}{4}, \frac{3}{4})$ . This material was discussed in detail in the paper by DE GROOT et al. in 1983 [2].

Once the crystal structure is specified, the next step is to determine the lattice constant. This is done by performing several DFT calculations with different lattice constants and comparing the total energy. The equation of state, which is the volume-dependence of the total energy, is fitted with the Murnaghan formula [93]:

$$E(\Omega) = E_0 + \frac{B_0\Omega}{B'_0} \left[ \left( \frac{\Omega_0}{\Omega} \right)^{B'_0} + 1 \right] - \frac{\Omega_0 B_0}{B'_0 - 1}, \quad (5.3)$$

where  $E_0$  is the total energy at equilibrium volume,  $B_0$  the equilibrium bulk modulus,  $\Omega_0$  the equilibrium volume and  $B'_0$  the pressure derivative of the bulk modulus at  $\Omega_0$ . The data points and the fitted Murnaghan curve are shown in Fig. 5.2. The least

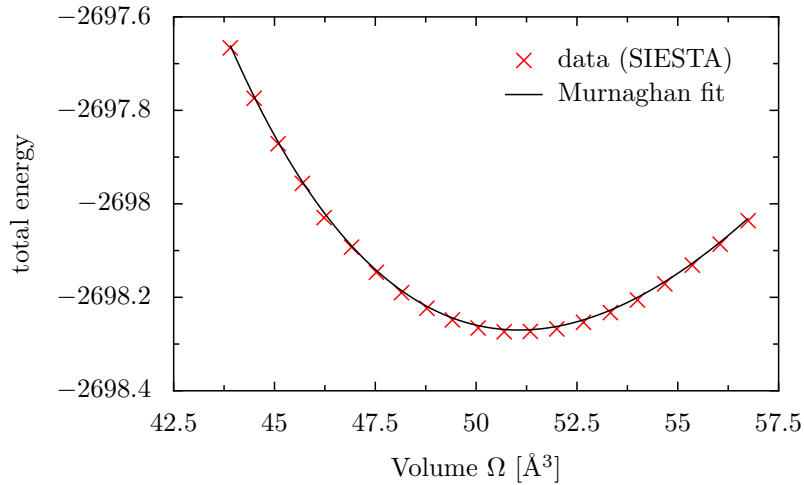


Figure 5.2: Fitting of the Murnaghan equation of state onto the data points obtained by several DFT calculations on a primitive unit cell incorporating different lattice constants.

square fitting procedure was used to estimate the following physical parameters:

$$\begin{aligned} E_0 &= -2698.3 \text{ eV} & B_0 &= 0.9125 \frac{\text{eV}}{\text{\AA}^3} \\ B'_0 &= 4.5032 & \Omega_0 &= 51.060 \text{ \AA}^3 \end{aligned}$$

The equilibrium volume of  $\Omega_0$  corresponds to a lattice constant of  $a = 5.88 \text{ \AA}$ . Experimental results for the lattice constant vary from  $5.904 \text{ \AA}$  to  $5.909 \text{ \AA}$  according to [94]. This lattice constant is the edge length of one cubic unit cell as seen in the left panel of Fig. 5.1. One primitive unit cell of NiMnSb contains three atoms as mentioned beforehand. The valence electron configuration for each atom used for the generation of the pseudopotentials is as follows:

$$\begin{aligned} \text{Ni} & 4s^2 4p^0 3d^8 4f^0 \\ \text{Mn} & 4s^2 4p^0 3d^5 4f^0 \\ \text{Sb} & 5s^2 5p^3 5d^0 4f^0. \end{aligned}$$

By summing up the occupation numbers for each orbital we get find a total number of 22 valence electrons per primitive unit cell. If we take a look at the band structure of NiMnSb in Fig. 5.3, we see that the minority spin band shows semiconducting behavior, as the Fermi level lies within a band gap. At the same time majority spin bands show metallic behavior. This gave rise to the expression ‘‘half-metal’’. Since

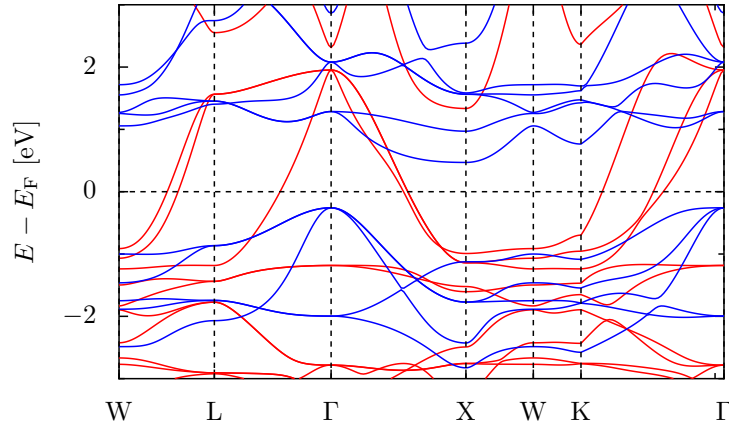


Figure 5.3: Band structure of bulk NiMnSb around the Fermi level. Majority spin bands depicted in red, minority spin bands in blue. Half-metallicity can clearly be seen as no minority spin bands are crossing the Fermi level.

the minority spin bands do not cross the Fermi level, all minority spin bands below  $E_F$  are completely filled. The energy range shown in Fig. 5.3 is too small to see all bands below  $E_F$  but there are in total 9 of them. Since a primitive unit cell of NiMnSb contains a total number of 22 valence electrons, there are 13 electrons left which carry the majority spin direction. The difference of majority and minority spin electrons yields a total magnetization of  $4\mu_B$  per primitive unit cell according to the Slater-Pauling behavior for half-metals [95]. If we take a look at the total density of states (DOS) in Fig. 5.4 we can observe that the DOS for majority spin (spin- $\uparrow$ ) electrons at the Fermi level is finite, whereas for minority spin (spin- $\downarrow$ ) electrons it is zero. The gap in the spin- $\downarrow$  domain is surrounded by two large peaks, which we now analyze using the projected density of states (PDOS)

$$\rho_i(\varepsilon) = \sum_n \langle \Psi_n | i \rangle \langle i | \Psi_n \rangle \delta(\varepsilon - \varepsilon_n), \quad (5.4)$$

where  $i$  is a multi-index containing information about the atom number and the quantum numbers  $n, l, m$  and  $s$ . In Fig. 5.5, we see that the peaks surrounding the minority spin gap come from  $d$  orbitals of Ni and Mn, where the occupied lower energy orbitals are of Ni character, whereas the unoccupied higher energy orbitals are of Mn character. The Ni  $d$ -orbitals are very weakly polarized and thus, contribute little to the magnetic moment, whereas the Mn  $d$ -orbitals are strongly spin polarized due to a large exchange splitting. According to DE GROOT et al. [2] the exchange interaction of Mn  $d$  electrons in combination with hybridization of Sb  $p$  states generate the half-metallic behaviour seen in Figs. 5.3 and 5.4.

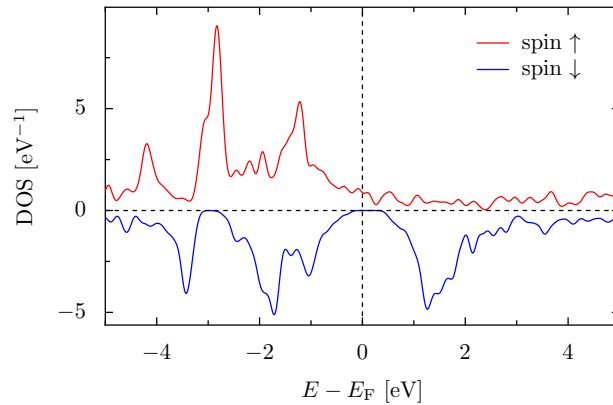


Figure 5.4: Spin resolved total density of states for bulk NiMnSb. Note the vanishing density of states around the Fermi level for the minority spin channel.

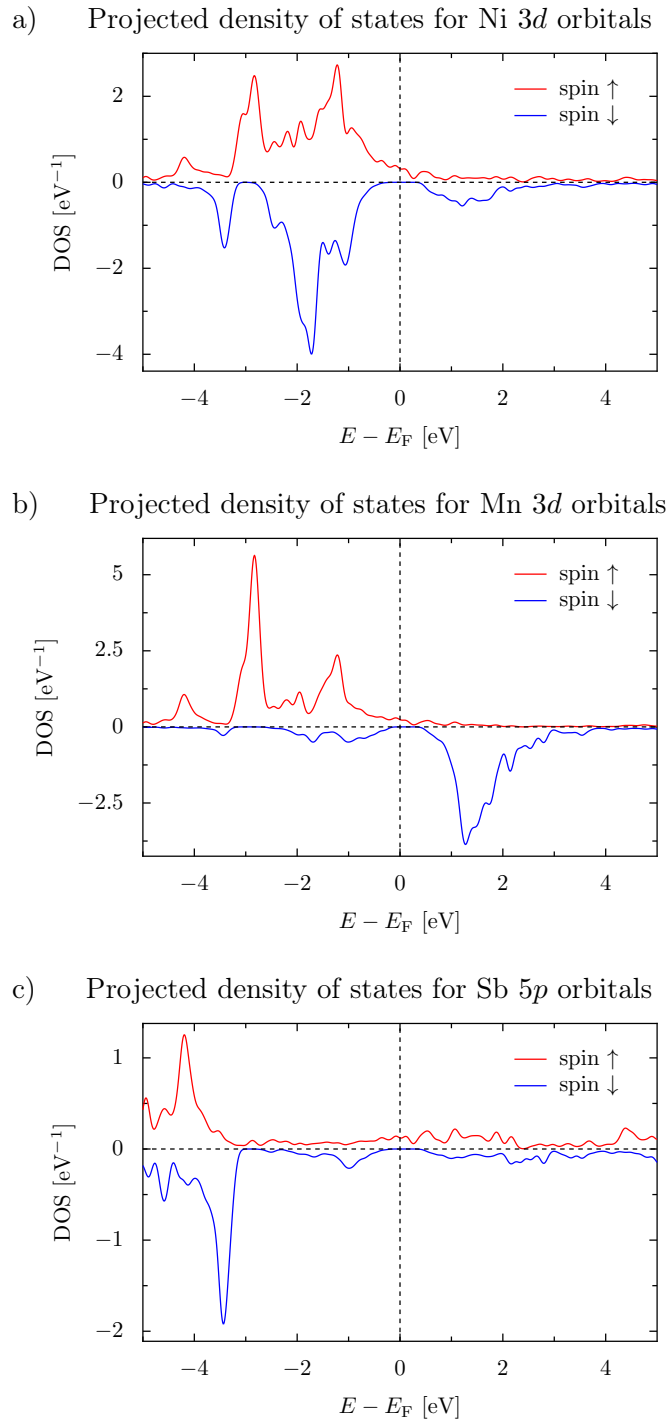


Figure 5.5: Spin resolved projected density of states for bulk NiMnSb. a) Ni 3d orbitals, b) Mn 3d orbitals, and c) Sb 5p orbitals.

## 5.2 The Transport Setup

In order to investigate the transport properties of NiMnSb, it can, for example, be connected to metallic leads. The difficulty in doing so lies in the search for a suitable metal. The metal should be easy to calculate within the methods of DFT and even more important, the lattice constant of the metal should match the lattice constant of NiMnSb which is 5.88 Å, as we found out in the last section. It is important to emphasize that not only the lattice constant is relevant but also the crystal structure. As we know, NiMnSb forms a fcc lattice, so the metal for the leads should also form a cubic or at least tetragonal lattice in order to make a matching perpendicular to the transport direction possible. A pure metal with such a lattice constant is hard to find.

Actinium ( ${}_{89}\text{Ac}$ ) comes close with 5.67 Å but is unfitting for two obvious reasons. On one hand, its atomic number of 89 is too high for SIESTA, and on the other hand it is radioactive and therefore unsuitable for applications. Another possibility is to search for metals with a lattice constant commensurable to that of NiMnSb. Here the most promising ratio is  $\frac{1}{2}$ . Candidates are  ${}_{22}\text{Ti}$  and  ${}_{48}\text{Cd}$  but neither of them forms a cubic or a tetragonal lattice. A third possibility, and also the one we chose, is to search for a metal with a fcc lattice and then rotate the lattice by  $45^\circ$  around the transport axis. The width of the new tetragonal unit cell is equal to the lattice constant divided by  $\sqrt{2}$ . For visualization see Fig. 5.6. The lattice constant of gold is 4.08 Å, which means the lattice mismatch can be calculated to

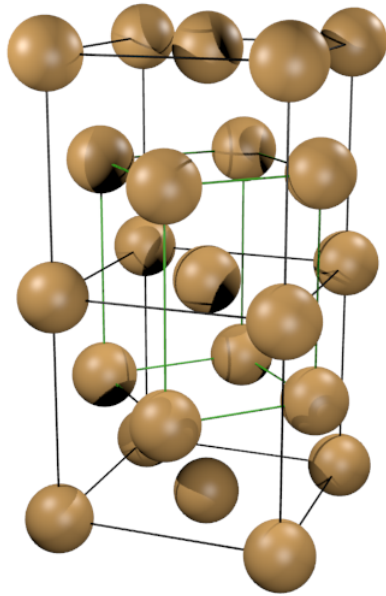


Figure 5.6: Here one can see two fcc unit cells of gold on top of each other. If one connects the eight gold atoms which are positioned in the middle of the faces perpendicular to the x- and y-axis, one gets a new unit cell which is now body centered tetragonal (bct). This bct unit cell is enclosed by the green conjunctions. The footprint of the bct unit cell is half the size of the fcc cell. Now four bct unit cells in a  $2 \times 2$  array match quite well with one cubic unit cell of NiMnSb. This matching can be interpreted as a rotation of the gold leads by  $45^\circ$  around the z-axis.

$$\Delta = \frac{\sqrt{2} \cdot 5.88 \text{Å}}{2 \cdot 4.08 \text{Å}} \approx 1.02, \quad (5.5)$$

which is a satisfying value. The next question that arises is how to contact NiMnSb with the gold leads. We already know that four body centered unit cells of gold in a  $2 \times 2$  array match with a cubic unit cell of NiMnSb, but there are basically four different ways to connect both materials. Regarding the crystal structure of gold, a primitive unit cell contains only one gold atom. In the cubic representation, that is common for fcc lattices, one unit cell contains four atoms. Since the body centered tetragonal cell has only half the volume of the cubic cell, we thus have only 2 atoms per bct unit cell. Therefore, the gold leads in the bct representation have two non-equivalent layers of gold atoms. These different layers are made of a) the atom on the corner of the unit cell, and of b) the atom in the body center of the unit cell.

The cubic unit cell of NiMnSb also contains two different kinds of layers. We have the Ni-layer and the Mn/Sb-layer. Now each of those two layers might end up being connected to either of the two gold layers, resulting in four different possibilities of

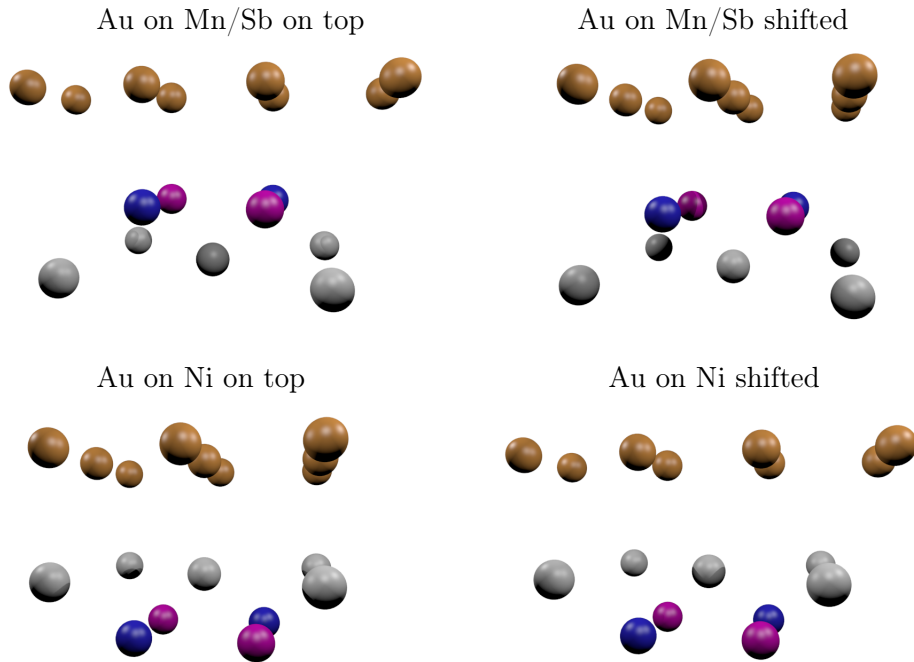


Figure 5.7: Visualization of the four cases of contact geometry. The top left picture shows the Au-on-Mn/Sb contact, where the atoms lie on top of each other. In the top right picture the same contact is shown but with shifted  $x$  and  $y$  coordinates, such that the atoms do not lie on top of each other anymore. The same is true for the two pictures at the bottom only in these cases for the Au-on-Ni contact.

contact geometry. A visualization of those 4 possibilities can be seen in Fig. 5.7. In two of those four cases, the gold atoms and the atoms of the neighboring layer of the Heusler alloy lie directly on top of each other (meaning they have the same  $x$  and  $y$ -coordinate). In the other two cases the  $x$  and  $y$ -coordinates differ by a quarter of the lattice constant of NiMnSb. In order to determine the optimized contact geometry, we had to perform several DFT calculations for each case. The variable in those calculations is the layer distance between the gold layer and the neighboring layer of the Heusler alloy. Here, layer distance simply means the difference in the  $z$ -coordinate of the atoms in the two considered layers. The total energy was plotted against the layer distance and the Murnaghan (Eq. (5.3)) formula was fitted onto the data points.

The results can be seen in Fig. 5.8. Due to the lattice structure of NiMnSb and the chosen transport direction, the energies in Fig. 5.8 cannot be compared. This is because one “unit cell” of NiMnSb with Ni on the outside has 14 atoms, whereas one cell with Mn/Sb on the outside has 16 atoms. The word unit cell was put in quotation marks because a true cubic unit cell of NiMnSb always has 12 atoms (4 Ni, 4 Mn and 4 Sb) but here we are talking about the closed version of a unit cell which ends with the same layer as it started. The reason for this difference in the number of atoms is simply the fact that one layer of Ni contains two atoms and one layer of Mn/Sb contains four atoms. This means that the bottom two curves and the top two curves in Fig. 5.8 belong to structures with a different number of atoms. But since the structure with more atoms still is higher in energy our choice fell on the “Au on Ni shifted” geometry (bottom right picture in Fig. 5.7).

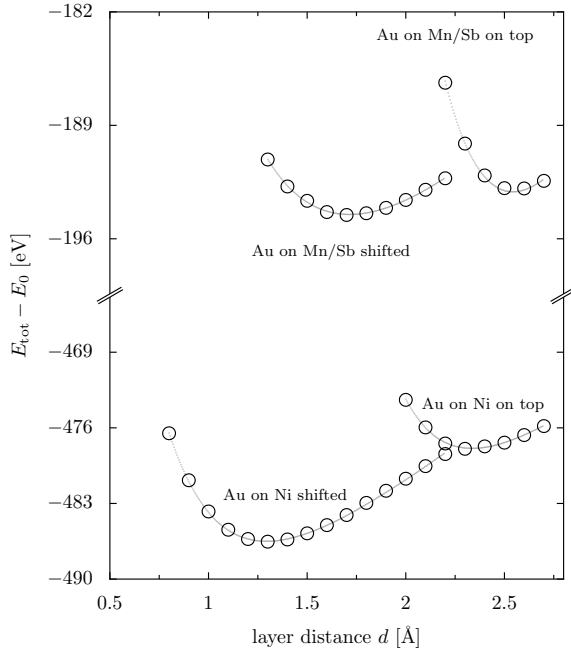


Figure 5.8: Murnaghan fit of total energy vs. layer distance between the Au leads and the NiMnSb scattering region for all four different cases of contact geometries (Fig. 5.7). In this context, layer distance means the difference in the  $z$ -coordinate of atoms in different layers.  $E_0$  is just a generic energy shift in order to avoid large numbers and must not be confused with the Fermi level.

With all the collected information we can now build the transport setup used in the next chapters. A visualization of this setup for one (closed) unit cell NiMnSb in the scattering region is shown in Fig. 5.9. There, the leads at the top and the bottom of the image are  $2 \times 2$  arrays of the green unit cell in Fig. 5.6.

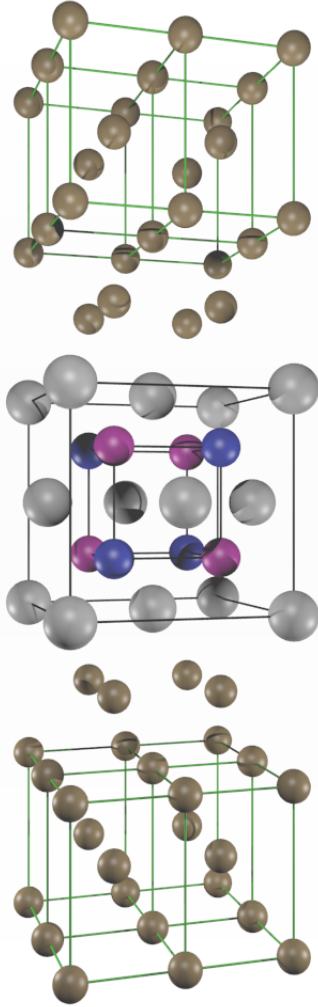


Figure 5.9: Schematic transport setup for one unit cell NiMnSb in the scattering region.

setup by placing the same kind of unit cells on top of each other. The infinite transport setup is then indistinguishable from one created with a symmetric scattering region and two different kinds of gold leads.

The Heusler alloy in the middle of Fig. 5.9 is not only closed in  $z$ -direction, but also in  $x$  and  $y$ -direction, which is why one can count 22 atoms instead of the previously mentioned 14 atoms.

The four gold atoms above and below the Heusler alloy are of the same kind as the ones in the center of the green unit cells in the leads. Their displacement in  $x$  and  $y$ -direction with respect to the Ni atoms is one fourth of the width of the NiMnSb unit cell. The layer distance between Au and Ni is  $1.30 \text{ \AA}$  according to the results depicted in Fig. 5.8 and the layer distance between two gold layers is  $2.04 \text{ \AA}$ .

For the layer distance between a Ni layer and a Mn/Sb layer we get  $1.47 \text{ \AA}$ . This transport setup can be easily extended with more unit cells of NiMnSb. For this thesis we increased the number of unit cells in the scattering region to up to four. The picture in Fig. 5.9 shows a symmetrized version (with closed unit cells) of the transport setup for better understanding of the structure.

In the actual calculation there are no closed unit cells. Since we only wanted to do one single calculation for the leads we chose a non-symmetric scattering region, where the number of gold layers differs on both sides. By doing so it is possible to create the infinite transport

# 6 Transmission Without Defects

## Contents

---

<b>6.1</b>	<b>One Unit Cell NiMnSb</b>	<b>77</b>
<b>6.2</b>	<b>Two Unit Cells NiMnSb</b>	<b>84</b>
<b>6.3</b>	<b>Three Unit Cells NiMnSb</b>	<b>91</b>
<b>6.4</b>	<b>Four Unit Cells NiMnSb</b>	<b>94</b>
<b>6.5</b>	<b>Conclusion</b>	<b>98</b>

---

In this chapter we investigate the transport properties of NiMnSb when connected to gold leads without any lattice defects. We consider both the transport setup exactly as in the last chapter, without relaxation, as well as a full relaxation of the interface region. This full relaxation goes beyond what was done in Fig. 5.8 and includes three translational degrees of freedom per atom in the respective area. A similar analysis is done for different numbers of NiMnSb unit cells within the scattering region.

## 6.1 One Unit Cell NiMnSb

### Unrelaxed Case

First, we start with one cubic unit cell in the scattering region. This cubic unit cell is closed in transport direction ( $z$ -axis) which simply means it has atoms at positions with  $z = 0$  as well as  $z = a$ . In directions perpendicular to the transport direction the cell is open which in return means that there are atoms with  $x = 0$  and  $y = 0$  but not with  $x = a$  and  $y = a$ , respectively. In total, we thus count 14 atoms in the Heusler part of the transport setup. Among those 14 atoms there are 6 Ni, 4 Mn, and 4 Sb atoms. Below and above the Heusler part, with a distance of  $1.30 \text{ \AA}$ , the gold leads begin. The jointed structure of Heusler alloy and a few gold layers is called extended molecule, according to chapter 3.

This extended molecule is sandwiched by Au leads on both sides, consisting of a  $2 \times 2$  array of gold unit cells in the body centered tetragonal representation, as explained in section 5.2. In this specific setup the bct unit cell contains four layers of gold atoms with one atom per layer such that the  $2 \times 2$  array has 4 atoms per gold layer. In total there are 66 atoms in this transport setup. The distribution

of those atoms is as follows: 32 atoms belong to the leads (16 for each side), 20 belong to the gold layers that are part of the extended molecule ( $3 \times 4$  above and  $2 \times 4$  below) and 14 atoms belong to the Heusler alloy itself.

The total number of electrons in this system is 680. In the nonrelaxed case it took 68 iterations to converge. For the k-mesh, the Monkhorst-Pack mesh [96] is used with 15 points for each direction perpendicular to the transport direction. The electronic temperature enters the calculation through the broadening of the Fermi function and is set to 300 K.

The total DOS is shown in Fig. 6.1. The caption of the vertical axis in that figure reads “EMPDOS” in contrast to the captions in Fig. 5.5. The “EM” stands for extended molecule and indicates that this DOS was obtained as part of the transport calculation with SMEAGOL unlike in section 5.1, where normal DFT calculations using SIESTA were done. If one takes a quick look at the scales on the vertical axis of Fig. 6.1 one notices the huge differences in comparison to Fig. 5.5, which is due to the very different number of atoms. The shapes of the spin- $\uparrow$  and spin- $\downarrow$  DOS are also almost identical. The reason for this is simply the distribution of the atoms. Since 52 out of the total 66 atoms in this structure are gold atoms, which are of course non-magnetic, it is not surprising that the total DOS is dominated by the gold atoms. Around the Fermi level no gap can be seen.

There is no reason to expect a half-metallic gap in the total DOS, because the different chemical environment at the interface may destroy the minority spin gap. Therefore, in the next sections, we ignore the total DOS, and instead we consider small subsets of atoms for the DOS calculation. The first of those small subsets

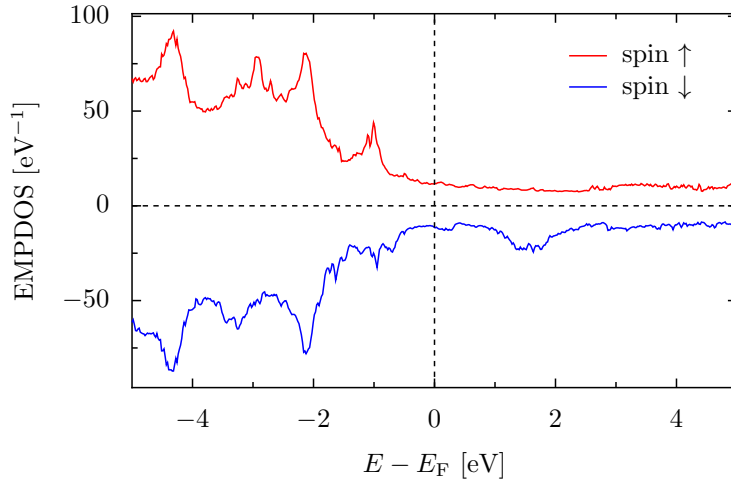


Figure 6.1: Total DOS of the entire transport setup containing 66 atoms. No half-metallic properties can be seen in this picture.

shall be named and defined in the next paragraph.

In order to compare the DOS in the transport setup with the bulk Heusler DOS as seen in Fig. 5.4, it is necessary to remove the gold part of the total DOS in Fig. 6.1. The DOS over all Ni, Mn and Sb atoms is from now on called “reduced density of states” and is shown in Fig. 6.2.

When the reduced density of states is compared with the bulk DOS of NiMnSb, as seen in Fig. 5.4, it is obvious that the scales are quite different. The reason for this is partially the size of the unit cell. In section 5.1 the DOS was calculated for a primitive unit cell of the bulk structure containing only three atoms, whereas this reduced DOS includes 14 atoms. Since this unit cell is closed for symmetry reasons, i.e. capped by two additional Ni atoms, an overemphasis on Ni is to be expected.

Although the gold atoms were removed from the DOS, we do not see a half-metallic gap in the minority spin channel. Obviously the influence of the gold leads destroys the half-metallic properties within the Heusler alloy. Some of the features that were present in the bulk Heusler alloy are still visible here. For example, in the minority spin channel, there are still two peaks visible, one above and the other one (significantly broadened) below the Fermi level. Also for the majority spin channel there are two peaks below the Fermi level at about  $-1$  eV and  $-3$  eV that are also visible in the bulk DOS.

A more detailed analysis of the DOS reveals that the broadening of the minority spin DOS between  $E - E_F = -0.5$  eV and  $E - E_F = -2$  eV originates from the two

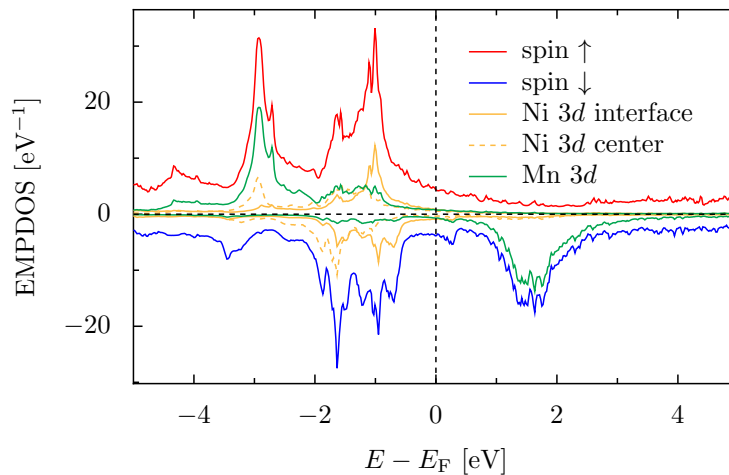


Figure 6.2: Reduced density of states where the gold contribution was removed. Here also no half-metallic gap in the spin- $\downarrow$  DOS can be seen.

different kinds of Ni atoms present. In Fig. 6.2 the dashed yellow line represents the density of the  $3d$  orbitals of the two central Ni atoms, whereas the yellow solid line represents the  $3d$  orbitals of **two** out of **four** remaining Ni atoms at the gold interface. The DOS of the central Ni atoms is comparable with the bulk results, as the peaks are at the right places and around the Fermi level the DOS is much lower compared to the other Ni atoms. The increased DOS for the interface Ni atoms can be explained by the lack of Mn bonding partners. This lack leads to a reduction of the exchange splitting at the Mn sites which is indicated by the peaks that are closer to the Fermi level as usual.

A huge difference between the two different Ni atoms can also be seen in the majority spin channel. The Ni contribution to the peak at  $E - E_F = -3$  eV is almost completely given by the central Ni atoms, whereas the peak at  $E - E_F = -1$  eV is mostly carried by the interface Ni atoms.

Regarding the Mn atoms, a good agreement to the bulk DOS can be found. This can be seen in the majority spin channel at  $E - E_F = -3$  eV and in the minority spin channel above the Fermi level. The reason for this is that no Mn atoms are directly influenced by the gold interface.

Figure 6.3 displays the zero bias transmission, which was calculated using a smoothing parameter  $\delta_T = 10^{-3}$  Ry which is added to the energy as a small imaginary contribution during the calculation of the transmission coefficient. The usage of such a parameter is necessary for producing a smooth EMPDOS, which is calculated as a part of the calculation of the transmission. This has to be done in order to compare the EMPDOS from the SMEAGOL calculation with the PDOS from the SIESTA calculation. It must be mentioned that we use the smoothed transmission for the discussion because it corresponds to the EMPDOS, but we still need the raw

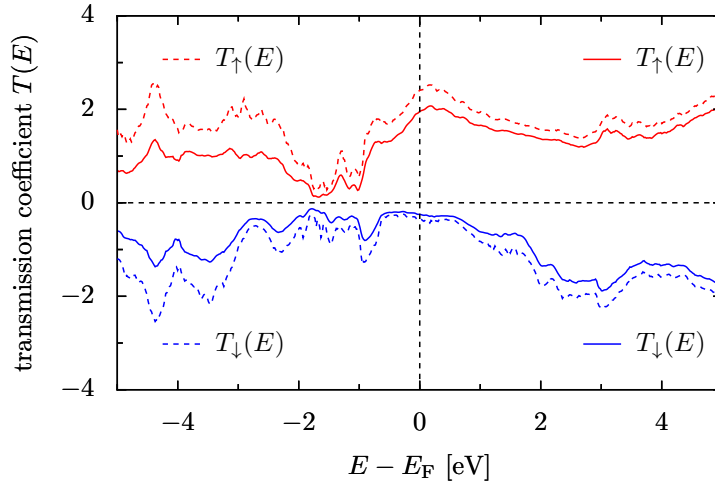


Figure 6.3: Transmission coefficient for one unit cell NiMnSb in the scattering region. Solid line: smoothed transmission, dashed line: raw transmission.

transmission later for comparison of currents. The difference between the smoothed and the raw transmission is basically just a scaling, as is visible in Fig. 6.3. This means that the qualitative results are equivalent. When we compare the transmission around the Fermi level with the reduced density of states in Fig. 6.2, we observe that the difference between the two spin channels in the transmission is much larger than in the EMPDOS. The fact that the values at the Fermi level differ so much for both spin channels leads to the conclusion that the states which are destroying the half-metallicity are not contributing to the transport properties. In order to investigate this result further and to localize these states in real space, it is useful to consider a larger scattering region, which is done in the next section.

### Relaxed Case

In order to quantify the influence of relaxation on the transport properties and the surface states, a total relaxation of the screening region, consisting of the closed NiMnSb unit cell and 5 layers of gold atoms, was done. Total relaxation in this case means that the  $x$ ,  $y$  and  $z$ -coordinate of each atom was varied independently using the conjugate gradient method. The relaxation was done in SIESTA using the Z-Matrix format in its simplest form, where the positions of the atoms were given in Cartesian coordinates and variation was allowed for all three coordinates of each atom.

The result of this full relaxation was that the Ni atoms at the interface with

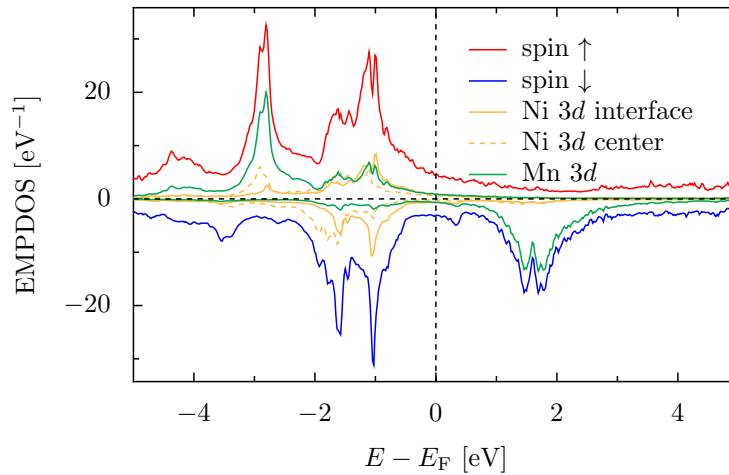


Figure 6.4: Reduced density of states for the relaxed structure. Almost no difference in comparison to the ideal, unrelaxed structure.

gold move slightly inwards, which means that the Ni atoms on the bottom edge of the Heusler unit cell move upwards and the Ni atoms on the upper edge move downwards. Regarding the Au atoms in the interface layer, we can distinguish two different classes of Au atoms. First, we have the Au atoms that are positioned vis-à-vis of the Mn atoms and second, the Au atoms vis-à-vis the Sb atoms. Here, the first kind of Au atoms which was facing the Mn atoms is more attracted to the Heusler alloy than the second kind of Au atoms, facing the Sb atoms. In both of the Mn/Sb layers we can observe a movement of the Sb atoms to the center of the structure as well as a movement of the Mn atoms away from the center.

In Fig. 6.4 the reduced density of states of the 14 Heusler atoms is shown for the relaxed structure. The comparison with Fig. 6.2 of the reduced DOS of the ideal system yields almost no difference. At about 1 eV below the Fermi level the peak in the majority spin DOS became smaller, whereas the peak in the minority spin DOS for the same energy became higher. Responsible for this change in the relaxed DOS is the re-positioning of the Ni atoms at the gold interface, especially the  $3d$  orbitals.

For the Mn atoms a small change in the shape of the peaks can be observed. In the minority spin channel, above the Fermi level, the broad peak now looks more like a narrow double-peak, and for the majority spin channel, the peak at  $E - E_F = -3$  eV now has a slightly different shape. These minor changes are caused by the subtle movement of the Mn atoms and their bonding partners within the Heusler unit cell.

The Ni atoms in the center of the structure are not influenced by the relaxation process. All the differences to the interface Ni atoms that were pointed out in the ideal structure are still valid in the relaxed structure. Overall one can say that the relaxation process does not bring noticeable changes, at least when comparing the DOSs.

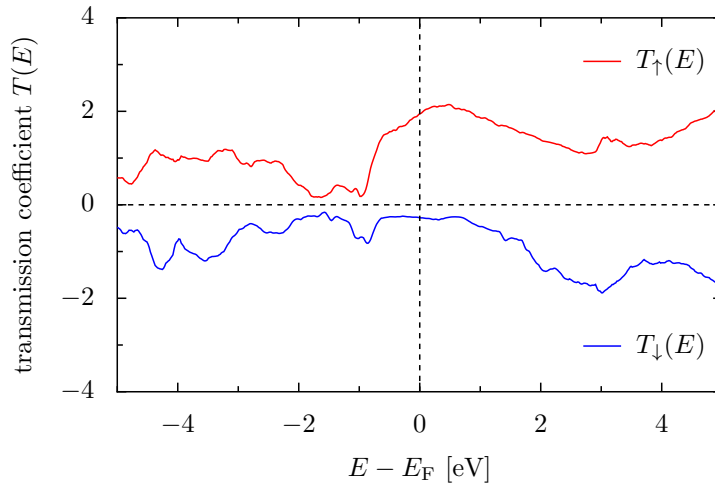


Figure 6.5: Transmission coefficient for one unit cell NiMnSb in the scattering region with relaxation.

If we take a look at the transmission coefficient for the relaxed structure in Fig. 6.5 and compare it to the transmission for the unrelaxed structure in Fig. 6.3 we observe that there is also almost no visible difference. This gives rise to the conclusion that the interface geometry with respect to relaxation does not have a big impact on the transport properties of this structure. There are minor differences in the transmission coefficient over the whole energy range shown in Figs. 6.3 and 6.5. In an energy range that corresponds to room temperature around the Fermi level, they are practically identical. If this trend of robust transport properties (with respect to interface relaxation) persists has to be checked for a larger scattering region.

### Current Calculation

Figure 6.6 shows the current voltage characteristic for one unit cell NiMnSb in the unrelaxed case, calculated according to Eq. (3.52). The current is given in the unit of ampere and is calculated for a rod with a footprint of  $5.88 \times 5.88 \text{ \AA}^2$ . The spin polarization of the current and the spin polarization of the transmission are defined as follows:

$$P_C = \frac{I_\uparrow - I_\downarrow}{I_\uparrow + I_\downarrow}, \quad P_T = \frac{T_\uparrow(E_F) - T_\downarrow(E_F)}{T_\uparrow(E_F) + T_\downarrow(E_F)}. \quad (6.1)$$

The spin polarization of the current has the value  $P_C = 0.747$ , and the spin polarization of the (smoothed) zero-bias transmission is  $P_T = 0.775$ . Those two numbers are very similar, whereas the spin polarization of the DOS (calculated analogous to  $P_T$ ) is almost zero. The calculated value of the current spin polarization of roughly 75% already exceeds the experimental value of SOULEN *et al.* of 58%, measured with a superconducting point contact. There are plenty of possible reasons for this, including disorder, lattice defects and temperature.

In addition to the spin resolved currents from the Landauer formula, Fig. 6.6 also shows the current that is given by a Taylor expansion of the Landauer formula with respect to the voltage  $V$ , from now on called linear response current:

$$I_{L,(\uparrow,\downarrow)} = V \frac{e^2}{h} T_{(\uparrow,\downarrow)}(E_F). \quad (6.2)$$

At this point the smoothing parameter  $\delta_T = 10^{-3} \text{ Ry}$  becomes important. As we know from the transmission plot in Fig. 6.3, the smoothing causes a downscaling of the transmission coefficient. This downscaling is responsible for the deviation of the smoothed linear response current from the NEGF current. If we use the raw transmission value in Eq. (6.2), the difference is much smaller. The fact that the spin dependency of the scaling is negligible leads to a good agreement of the smoothed and raw spin polarization, because the scaling cancels out in essence. In SMEAGOL, the transmission is calculated in two different routines. One of them uses the smoothing parameter and the other one does not. The one that does not is called during the calculation of the current via the Landauer formula in Eq. (3.52) which means that

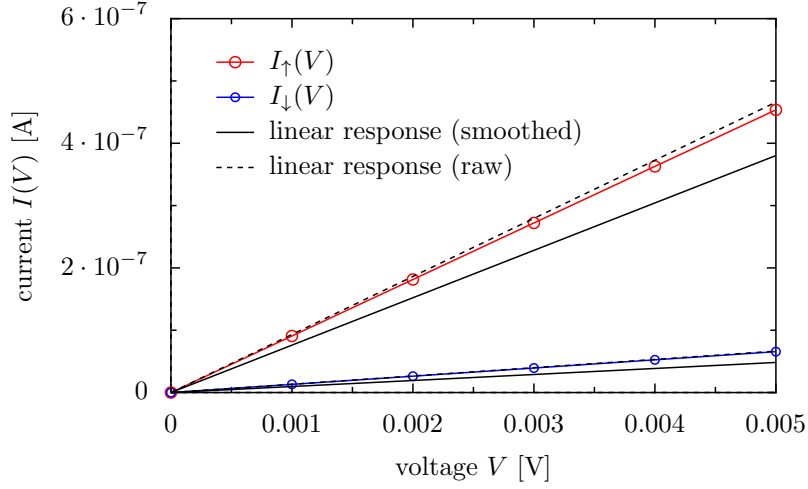


Figure 6.6: Current through one unit cell of NiMnSb in the unrelaxed case. Six data points (circles) were calculated for each spin channel.

the resulting current voltage characteristic is independent of  $\delta_T$ . The remaining deviation of the raw linear response from the NEGF current in Fig. 6.6 can normally be attributed to the shape of the transmission coefficient around the Fermi level and the voltage dependency of the transmission. For low voltages like here, however, the voltage dependence of the transmission is negligible. The differences in this case come from the high electronic temperature of 300 K, which is used to broaden the Fermi distributions, whereas for Eq. (6.2)  $T = 0$  K was assumed.

In order to put the scales of Fig. 6.6 into context, it is important to note that the voltage is very small compared to most electric devices, but due to the small cross-section of the scattering region, the electric fields are extremely high. The resulting current densities are therefore extremely high ( $\approx 10^{13}$  A/m<sup>2</sup>) compared to current-densities realized in experiments. Currents of that magnitude would cause the sample to vaporize immediately.

## 6.2 Two Unit Cells NiMnSb

### Unrelaxed Case

In this section we consider a scattering region that consists of two unit cells of NiMnSb. Here, like in the last section, the Heusler part of the scattering region is closed, which means it begins and ends with Ni atoms. In total we thus have 26 atoms in the Heusler part of this transport setup. Out of these 26 atoms, there are 10 Ni atoms and 8 atoms of each Mn and Sb.

The distance between the outer Ni layer and the neighbouring Au layer is again

1.30 Å. For the additional gold layers on both sides of the Heusler part we chose two layers below and three layers above the Heusler part. These additional gold layers are then again connected to  $2 \times 2$  arrays of the leads on both sides so that in total there are 78 atoms in this transport setup with a total number of 768 valence electrons. For the other parameters such as k-point mesh and the electronic temperature the same values are used as in the last section. This is especially important since the same lead calculation was used. For the ideal unrelaxed case, convergence was reached after 80 iterations.

The reduced density of states is shown in Fig. 6.7. If we compare this DOS with the corresponding plot for one unit cell NiMnSb in the scattering region as seen in Fig. 6.2 we observe that the peaks are located at the same energies but differ in height. Most of the peaks have about twice the height here, compared to the one unit cell case. This comes with no surprise, since the scattering region also contains almost twice the number of atoms. A deviation from this trend is given by the peak at  $E - E_F = -1$  eV for the majority spin DOS. This peak is much smaller than the peak to its left, whereas in Fig. 6.2 it was even slightly higher in comparison. A similar feature, although not as much pronounced, can be seen in the minority spin DOS at the same energy. There, the peak is about the same height as the peak to the right, above the Fermi level. If we now go back to Fig. 6.2 we see that the peak at  $-1$  eV is also slightly higher than the peak to its right. This is even more obvious if we compare Fig. 6.7 with Fig. 6.4 of the relaxed structure.

At this point it is important to note that a comparison of those two densities of states is more suitable to point out similarities than differences. This is due to

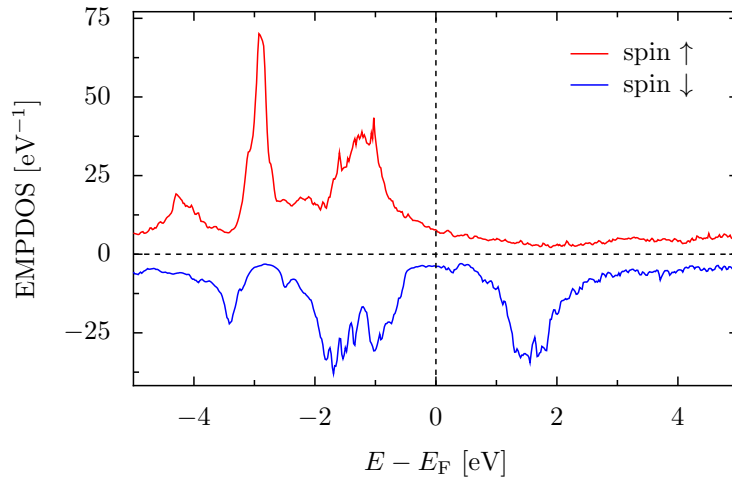


Figure 6.7: Reduced density of states for two unit cells of NiMnSb in the scattering region. No half-metallic gap in the spin- $\downarrow$  DOS can be seen.

the fact that in the case of two NiMnSb unit cells in the scattering region, a few new classes of atoms appear. If we take a look at Fig. 5.9 and especially the Mn/Sb atoms in blue/purple we see that they are all equivalent by symmetry, but if we imagine a second unit cell of NiMnSb we suddenly have Mn/Sb atoms with a different surrounding area and therefore a different chemical behaviour.

In the last section, for the non-relaxed case, we had two classes of Ni atoms and one class of each Mn and Sb atoms. Here, in the non-relaxed two-unit-cell case, we have three classes of Ni atoms and two classes of each Mn and Sb atoms. Among the three classes of Ni atoms we have the ones in the contact layer next to the gold atoms, the ones in the central layer with equal distances to the gold layers at both sides, and the Ni atoms in the two intermediate layers, where the distance to one of the gold layers is smaller than the distance to the other one. Regarding the Mn and Sb atoms, the two classes that can be found in this structure are defined by the distance their layer has to the center of the structure (or to the gold atoms). The two Mn/Sb layers that are directly above and below the central Ni layer are equivalent.

Although none of the new classes which are found in the structure with two NiMnSb unit cells, have an equivalent counterpart in the one-unit-cell case, there are some classes which are similar enough to be compared. The Ni atoms at the interface, for example, show almost an identical DOS for both cases, of course only for the unrelaxed structure. This does not hold for the two Ni atoms in the center of each structure. In the two-unit-cell case, the DOS for those two Ni atoms shows a half-metallic behaviour, i.e., the DOS around the Fermi level for minority spin

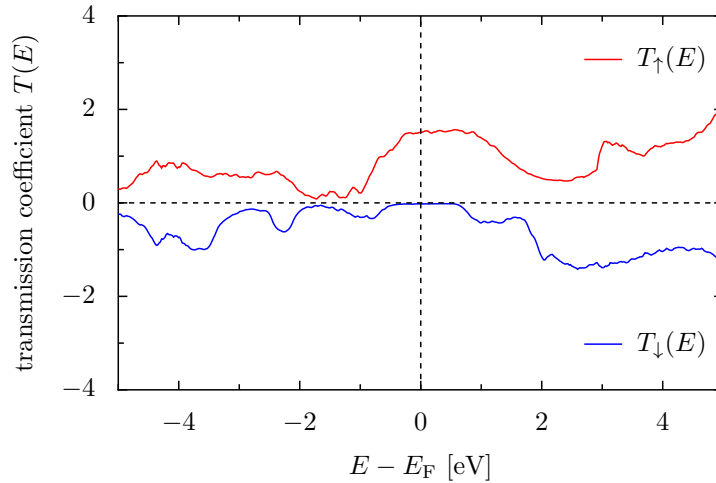


Figure 6.8: Transmission coefficient for two unit cells NiMnSb in the scattering region. Although the reduced density of states still contradicts a half-metallic behaviour, the transmission around the Fermi level shows a significant spin polarization.

electrons drops to (almost) zero, whereas the DOS for majority spin electrons stays finite. A similar behaviour was not visible for one unit cell NiMnSb in the scattering region. This tells us that one unit cell of NiMnSb is just too thin to provide a half-metallic transport if connected to gold leads, which destroy the half-metallic properties at the interface. Two unit cells of NiMnSb, on the other hand, are thick enough to preserve the bulk-like half-metallicity in the center of the structure. This is mirrored in the plot for the transmission coefficient in Fig. 6.8. There, a strong spin polarization at the Fermi level is clearly visible.

If compared to the transmission for one unit cell NiMnSb in Fig. 6.3 (the unrelaxed one), it is obvious that the transmission is generally lower here, which can be explained by the longer scattering region. To conclude, as an interim result, we can say that although half-metallicity is destroyed at the interface by the presence of the gold leads (states within the supposed gap), the relevant part of the transmission coefficient around the Fermi level is highly spin-polarized even for a small layer thickness of 2 unit cells, which corresponds to less than 12 Å.

### Relaxed Case

Next, we take a look at the relaxed structure. A full relaxation was done incorporating Au layers as well as the two NiMnSb unit cells in the scattering region. The result of the relaxation process is that the Mn and Sb atoms in the two layers around the center of the structure barely move at all, whereas the Mn and Sb atoms in the two outer layers move slightly similar to the last section. The other atoms follow the pattern of the one-unit-cell case, such as the Ni atoms in the outer layers, which move towards the center.

The reduced density of states shows almost no difference compared to the non-relaxed DOS, which is consistent with the results of the previous section for one unit cell NiMnSb in the scattering region. At this point the new term “inner unit cell” shall be defined. The inner unit cell is used in the case of two NiMnSb unit cells (also in the next chapter including defects) and is built by joining the upper half of the bottom unit cell with the bottom half of the upper unit cell (also see Fig. 6.10). In Fig. 6.9 the DOS for this inner unit cell is shown, which comes close to the DOS of the bulk as in Fig. 5.4, including the (almost) vanishing minority spin DOS around the Fermi level.

This half-metallic DOS of the inner cell, which was not obtained in the previous section, is responsible for the significant spin polarization in the transmission coefficient. Now we want to visualize the spacial distribution of the states that contribute to the finite DOS for the minority spin channel around the Fermi level in the reduced density of states. Therefore, we use the concept of the local density of states (LDOS):

$$\rho(\mathbf{r}, \varepsilon) = \sum_n \langle \Psi_n | \mathbf{r} \rangle \langle \mathbf{r} | \Psi_n \rangle \delta(\varepsilon - \varepsilon_n), \quad (6.3)$$

where the  $|\Psi_n\rangle$  are the Kohn-Sham eigenstates. In the SIESTA implementation one has to define an energy range in which the LDOS is integrated. This range was chosen to be  $E_F \pm 30\text{meV}$ , which corresponds to room temperature and thus confines the energy to a small window around the Fermi level. We therefore only visualize the states that are closing the half-metallic gap.

In Fig. 6.10 the LDOS is shown for a structure consisting of a closed two unit cell block of NiMnSb and five layers of gold atoms (the gold layer on the bottom/top edge is printed twice). The red/blue cloud-like structures are isosurfaces for the energy integrated LDOS. Two different directions are shown, namely the view from the 100 direction in a), and the view from the 110 direction in b). The crystal structure in Fig. 6.10 belongs to the unrelaxed case. The isovalue, which is represented by the isosurface, is chosen rather small (0.35% of the maximum value) in order to create isosurfaces large enough to be interpreted. One may notice that there is a clear spacial distribution of the LDOS regarding the spin channel.

The blue isosurfaces, which belong to the minority spin channel, are mainly located at the Au-Ni interface and partially in the gold region of the structure, but are nowhere to be found in the central part of the scattering region. This central part, previously labeled inner unit cell, is the same area the DOS in Fig. 6.9 was calculated for. If compared to the results shown in Fig. 6.9, there is a good agreement in terms of the absence of minority spin states in a small energy range around the Fermi level. It is also important to point out that the data which was used to create

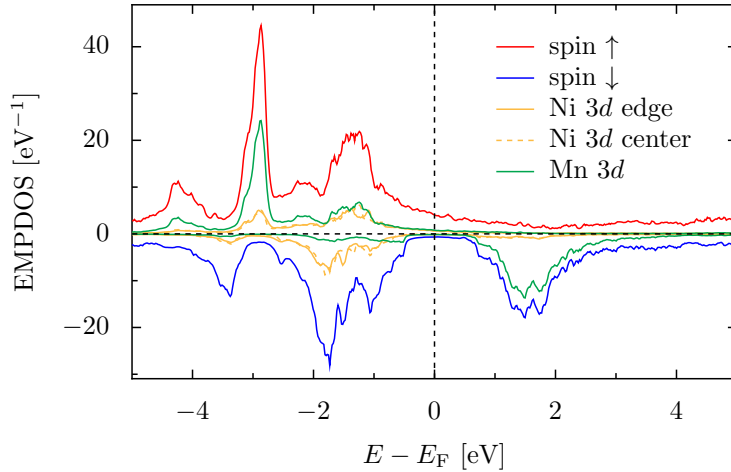


Figure 6.9: Total density of states for the closed inner unit cell of NiMnSb. This inner unit cell consists of the upper half of the bottom unit cell and the bottom part of the upper unit cell. Here a clear tendency to half-metallicity is observed, although not as strong as in the bulk.

Figures 6.9 and 6.10, respectively, was not obtained in the same calculation. The data which led to the LDOS in Fig. 6.10 was obtained using only SIESTA, whereas the data for the EMPDOS in Fig. 6.9 was obtained during a transport calculation using SMEAGOL (hence the additional “EM”).

What we can learn from this is that the states that are “destroying” half-metallicity are indeed localized at the interface between gold and the Heusler alloy, and thus do not contribute to the transport properties if the scattering region is large enough to separate those states.

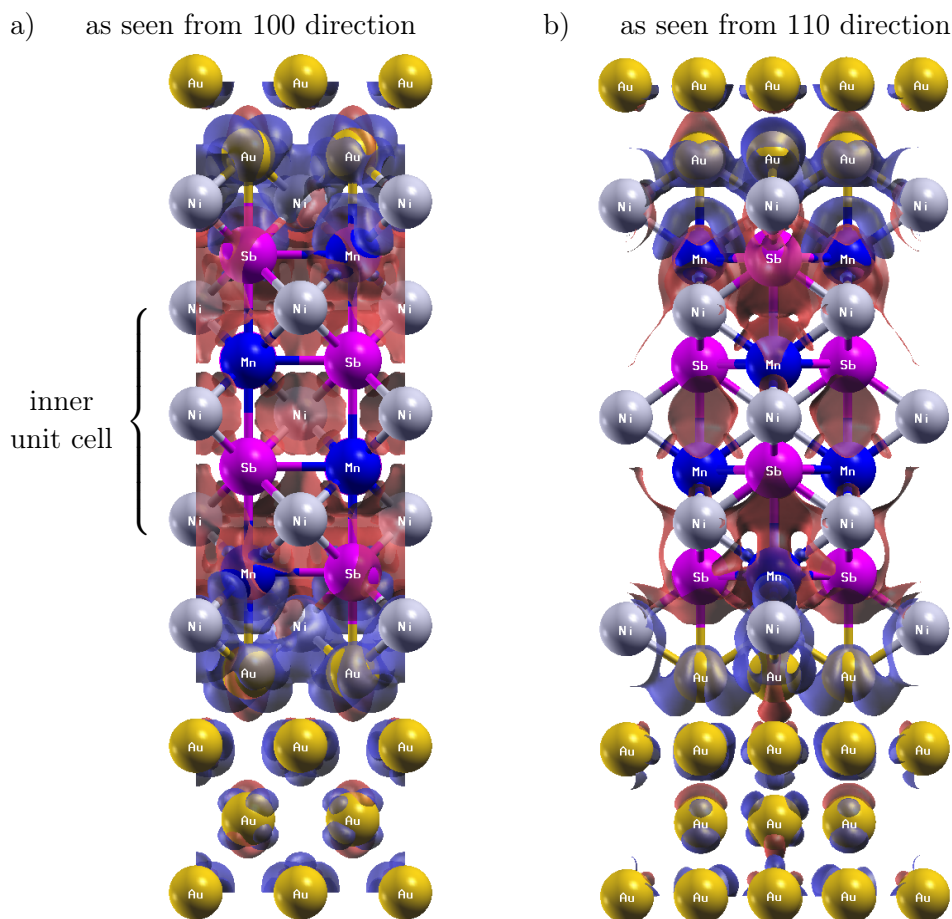


Figure 6.10: Spin resolved LDOS, energy-integrated  $\pm 30$  meV around the Fermi level. Red isosurfaces represent spin- $\uparrow$  states and blue isosurfaces represent spin- $\downarrow$  states.

## Current Calculation

The calculated spin resolved currents, as seen in Fig. 6.11, reflect the results that were already visible in the transmission. The spin polarization of the current is  $P_C = 0.964$ , and the polarization of the transmission is  $P_T = 0.972$ . For the majority spin channel, similar to the one-unit-cell case, we again observe a small deviation from the SMEAGOL current and the linear response current due to the high temperature and the non-constant transmission around the Fermi level. As in the previous section, we observe a large deviation from the smoothed linear response from the NEGF current, again resulting from the scaling of the transmission. While the current for the majority spin channel decreased by 18.6%, compared to the one-unit-cell case, the minority spin current on the other hand drastically diminished by 89.6%.

The increased spin polarization can be attributed to the formation of the half-metallic inner unit cell. In the previous section the scattering region was too small to provide a truly half-metallic intermediate region, resulting in a relative large transmission at the Fermi level in the minority spin channel.

For two unit cells of NiMnSb in the scattering region on the other hand, a half-metallic intermediate region was formed that prevents minority spin electrons from passing through the structure, hence resulting in an almost vanishing transmission coefficient at the Fermi level. This means that, according to the calculated current in Fig. 6.11, a relatively thin layer of two NiMnSb unit cells, which is less than 12 Å thin, is already enough to create a spin filter with over 96.4% accuracy.

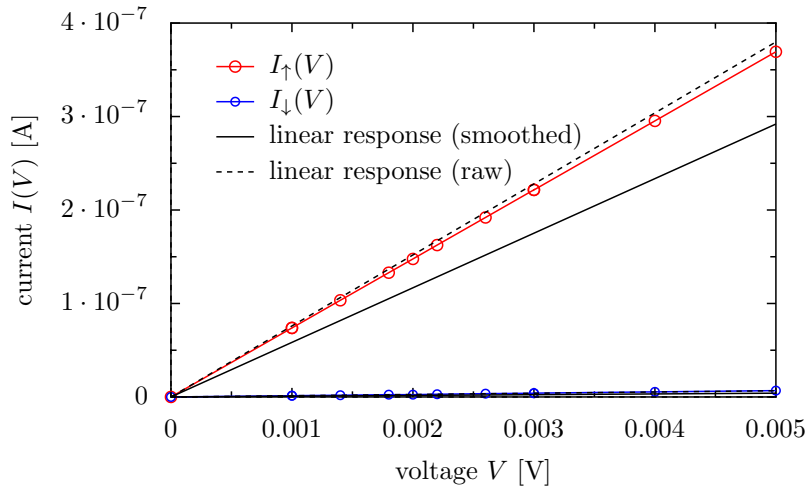


Figure 6.11: Current through two unit cells of NiMnSb in the unrelaxed case. Nine data points (circles) were calculated for each spin channel

### 6.3 Three Unit Cells NiMnSb

In this section we consider a scattering region consisting of three cubic unit cells of NiMnSb, again with two additional Ni atoms for symmetry reasons. For simplicity, we spare a detailed analysis of the relaxed structure, because according to the previous sections, relaxations have hardly any influence on the transport properties. A detailed analysis of the DOS shall only be given for the ideal structure, and the differences to the relaxed structure shall only be demonstrated by comparison of the resulting transmission coefficients.

Including the leads, the whole transport setup contains 90 atoms, of which 14 are Ni, 12 are Mn, another 12 are Sb, and the remaining 56 atoms are Au. The total number of valence electrons in this system is 856. In order to ease the convergence of the transport calculation a regular DFT calculation was performed in order to provide an already converged electron density. In that calculation, self-consistency was reached after 51 iterations.

Regarding the electronic structure of the system, Fig. 6.12 shows the zero-bias DOS for the central unit cell of NiMnSb. The general shape of the DOS is very similar to the respective DOS plots in the previous sections, however, the half-metallic gap in the minority spin channel is even more pronounced. The differences between the two Ni layers displayed became even smaller compared to the last section, indicating a bulk-like electronic structure in the central part of the scattering region.

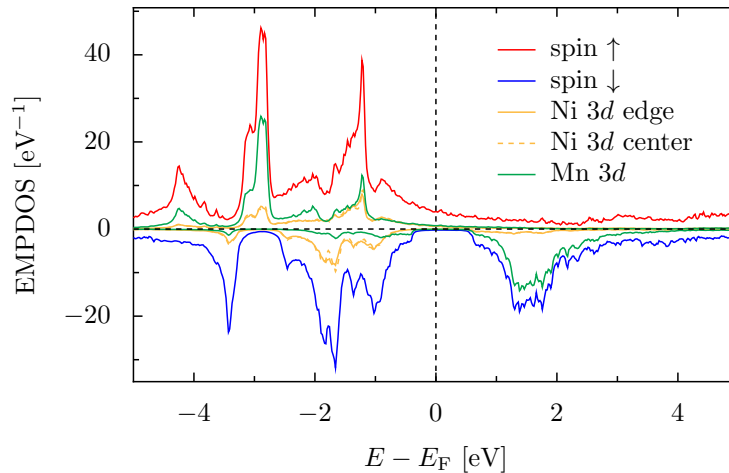


Figure 6.12: Density of states for the central NiMnSb unit cell. There is almost no difference between the central Ni atoms and the one at the edges of the central unit cell.

An observed difference of the DOS compared to the DOS in Fig. 6.9 is the sharpness of the peak in the majority spin channel at  $E - E_F \approx -1$  eV, which is caused by Ni and Mn  $3d$  orbitals.

Beyond that, no big differences to the last section is found. This is not surprising since the two-unit-cell case already showed an almost bulk-like behaviour.

The transmission coefficients for this setup are shown in Fig. 6.13. Besides the transmission coefficient for the ideal unrelaxed structure, this figure also shows the transmission for the relaxed case in order to visualize how small the differences are. The values are, for both spin channels and over most parts of the considered energy range, smaller than in the previous two sections, which further supports the idea that longer scattering regions result in smaller transmissions. Deviations from this trend can be found at high energies beyond  $E - E_F = 2$  eV, compared to Fig. 6.8. These differences can be partly assigned to the relaxation of the structure in the two-unit-cell case. A comparison with the non-relaxed transmission for two unit cells (not shown here) gives much less differences in the energy range beyond  $E - E_F = 2$  eV.

For the unrelaxed case, the spin polarization of the transmission is  $P_T = 0.994$ , which is slightly higher than the spin polarization in the last section where a value of  $P_T = 0.972$  was found. The transmission of the relaxed structure yields a polarization of  $P_T = 0.996$ , which exceeds the unrelaxed polarization by a small margin. The minority spin transmission for the unrelaxed case at  $E_F$  is twice as large as the one for the relaxed case, yet still very low compared to the majority spin channel. Regarding the majority spin transmission at  $E_F$ , we can see that in the relaxed case the transmission is slightly higher, which explains the minimally increased spin polarization.

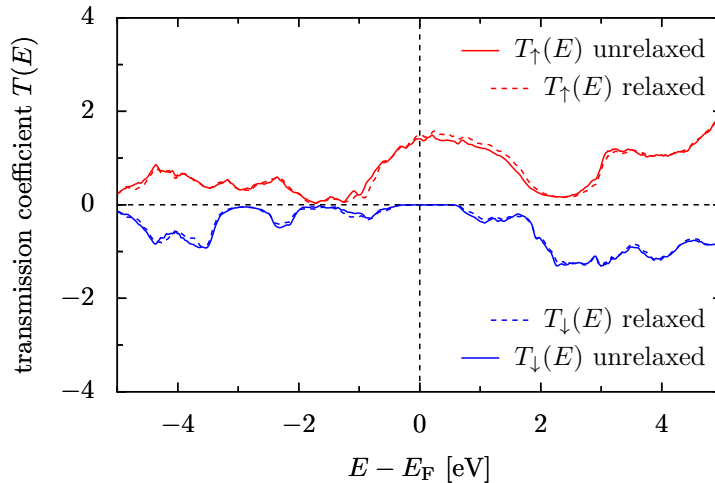


Figure 6.13: Transmission coefficient for the three-unit-cell case. The differences between relaxed and unrelaxed structures are negligible.

### Current Calculation

The calculated spin resolved currents are displayed in Fig. 6.14. Regarding the majority spin channel, we find an almost identical behavior compared to the two-unit-cell case. For the minority spin channel, on the other hand, a significant reduction of the current compared to the previous case is observed. The spin polarization of the current is  $P_C = 0.991$ , which is also higher than the corresponding value of the two-unit-cell case ( $P_C = 0.964$ ). Here again the spin polarization of the current is lower than the polarization of the transmission, however, the difference becomes smaller as the thickness of the scattering region increases.

The deviation in the majority spin channel of the NEGF current, provided by SMEAGOL, from the linearized current, which uses the zero bias transmission, is bigger in the three-unit-cell case than it was in the previous section. Since the voltage dependence of the transmission is negligible, a possible reason for this finding is the strong energy dependence of the transmission around the Fermi level. In the last section, the slope of the transmission around  $E_F$  varied to a much smaller degree. This implies that the transmission at  $E_F$  can not be simply extracted from the data, but has to be calculated as an arithmetic average over several data points around the Fermi level and is therefore prone to some errors.

The large electronic temperature of  $T = 300$  K also contributes to the deviation, since a requirement for the validity of the linearised current formula in Eq (6.2) is the assumption, that the derivative of the Fermi distribution has the shape of a Dirac  $\delta$ -distribution, which is only the case for  $T = 0$  K.

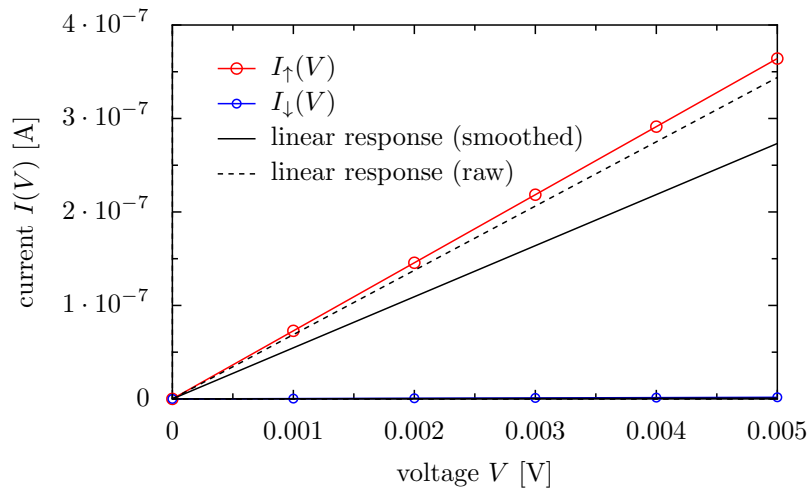


Figure 6.14: Spin-resolved current for the three-unit-cell case.

## 6.4 Four Unit Cells NiMnSb

In this section we want to consider the structure with four unit cells of NiMnSb in the scattering region in order to see if the tendencies we discovered in the previous two sections prevail. The geometry of the unit cell is the same as before with a total number of five gold layers, where two layers were located below and three were located above the Heusler part. Like in section 6.3, we only consider the non-relaxed ideal structure since the relaxation does not influence the transport properties (see Fig. 6.13). The total number of atoms in this setup is 102, among which are 52 gold atoms. Among the remaining 50 atoms, there are 18 Ni atoms and 16 atoms of each Mn and Sb. The total number of electrons in this calculation is 944.

In order to achieve convergence for this large structure, a non-transport calculation was performed in SMEAGOL to obtain an initial charge density which was used for the transport calculation. During this non-transport calculation, SMEAGOL calls a SIESTA routine which performs a standard DFT calculation on the system. With this method, convergence was achieved after 54 iterations.

At first we take a look at the EMPDOS of the scattering region. Figure 6.15 depicts the DOS for the inner unit cell. Analogous to the two-unit-cell case the inner unit cell is located in the center of the scattering region. In this case, it consists of the upper half of the second unit cell and the bottom part of the third

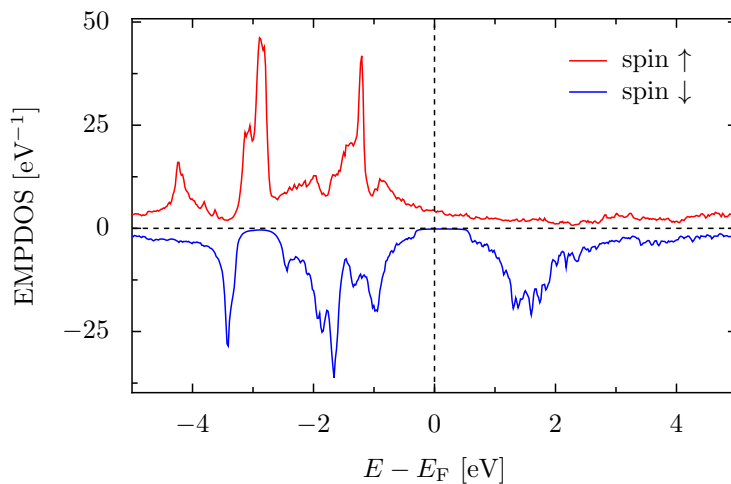


Figure 6.15: Density of states for the inner unit cell of the scattering region. Since the total number of unit cells is even, the inner unit cell consists of the upper half of the second cell and the lower half of the third cell.

unit cell. The half-metallic gap in the minority spin channel is clearly visible and much more pronounced than in the previous cases. With the vanishing DOS around 3 eV below the Fermi level, the EMPDOS of the inner unit cell looks very similar to the DOS of a bulk unit cell of NiMnSb as given in Fig. 5.4. If one compares this with Fig. 6.9 of the relaxed two-unit-cell case, one sees that the peaks in the DOS are at the same positions but differ in height and shape. This can be explained with the increased distance to the gold layers in the four-unit-cell structure.

It is possible to create a DOS plot almost identical to the one in Fig. 6.9 with the data obtained in the four-unit-cell case by combining the corresponding layers. This means if we combine the upper part of the first unit cell with the bottom part of the fourth unit cell, we get an effective unit cell very similar to the inner cell of the two-unit-cell case because the distance to the gold layers on both sides is the same.

Both, the DOS of the inner unit cell in the two-unit-cell case, and the DOS of the effective unit cell in the four-unit-cell case are presented in Fig. 6.16. The small differences between the two densities of states can be explained with the different chemical environment in those two cases. In the four-unit-cell case, the atoms in the upper part of the first unit cell have a more half-metallic surrounding due to the extended bulk-like structure in between the two gold interfaces. The good over-all agreement of the two DOS plots does speak for a high transferability of the results of sections 6.1 to 6.4.

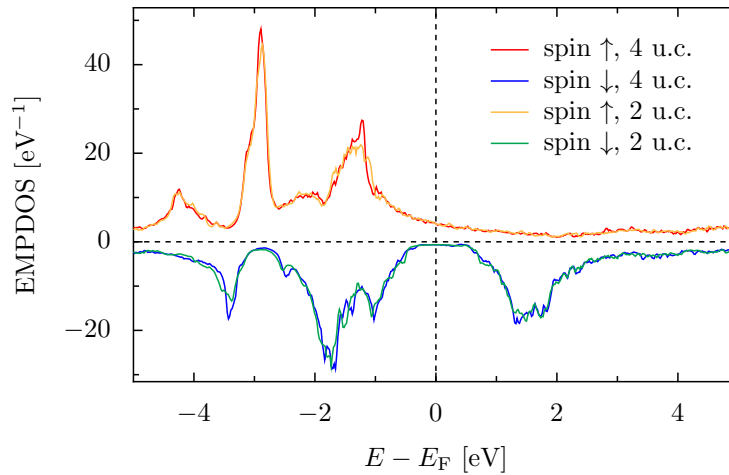


Figure 6.16: Projected density of states for the inner unit cell of the two-unit-cell case and the artificially constructed effective unit cell in the four-unit-cell case.

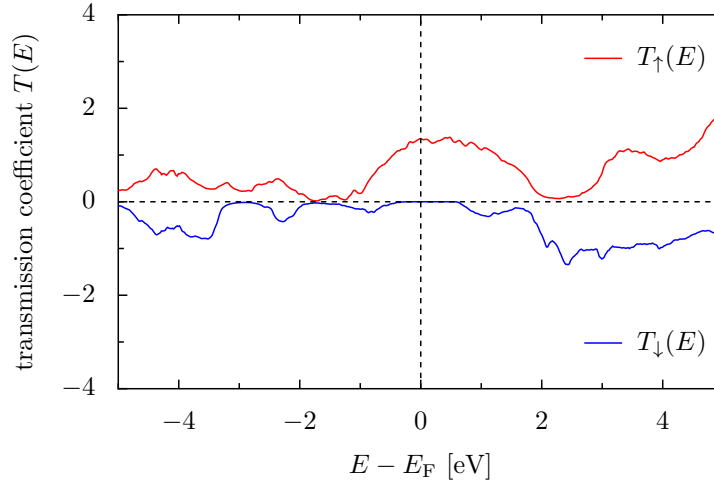


Figure 6.17: Transmission coefficient for four unit cells NiMnSb in the scattering region.

Regarding the transmission coefficients in Fig. 6.17, we also see a half-metallic gap in the minority spin channel. Unsurprisingly the gap is more pronounced in this case as well, which agrees with the results of the DOS. Comparison of the transmission coefficients with the other three cases yields that the absolute value of the transmission coefficient shrinks with increasing layer thickness of the Heusler alloy. This is exactly what was to be expected in view of the results of the Kronig-Penney toy model in section 4.3. The corresponding figure can be found in section 6.5 (Fig. 6.22). This means that a higher value of spin polarization of the current has to be paid with a lower transmission rate.

## Current Calculation

The current-voltage plot is displayed in Fig. 6.18. Due to the size of the system and the thus increased computation time, only four data points were calculated instead of the previously calculated five. We find that the spin polarization of the current,  $P_C = 0.999$ , agrees with the spin polarization of the transmission,  $P_T = 0.999$ .

A comparison of the majority spin current for the four different cases (one to four unit cells within the scattering region) yields a similar order of magnitude. Regarding the minority spin currents, on the other hand, we find a drastic drop with each additional layer. This is displayed in Fig. 6.19, where all currents are depicted on a logarithmic axis. The majority spin currents, with exception of the one-unit-cell case, are very similar. The exception of the one-unit-cell case compared to the other three implies that a direct lead-to-lead tunneling strongly influences the transmission. For larger scattering regions, this tunneling becomes irrelevant with the result that, at the given scale, the majority spin currents for two, three, and

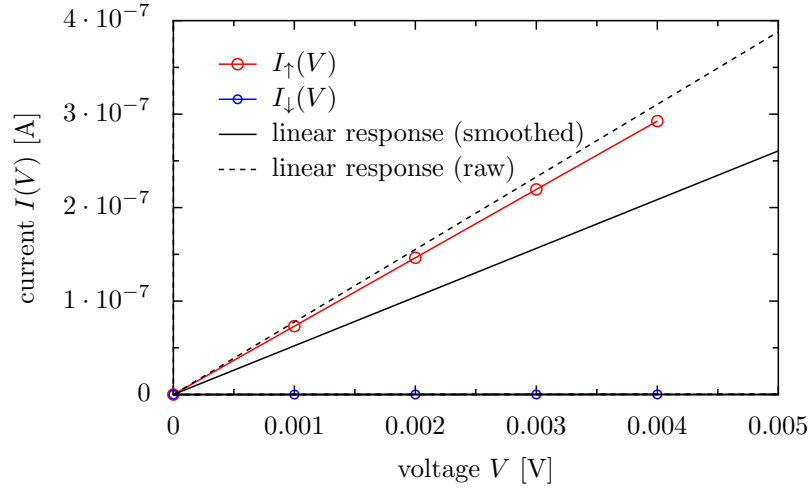


Figure 6.18: Spin-resolved current for the four-unit-cell case.

four NiMnSb unit cells are visually indistinguishable. The minority spin currents, however, differ by a rather large factor, which results in a constant shift of the curves on a logarithmic scale. The dependence of the minority spin transport properties on the size of the scattering region will be quantified (using the transmission coefficient and the Kronig-Penney toy model) in the conclusion of this chapter in section 6.5.

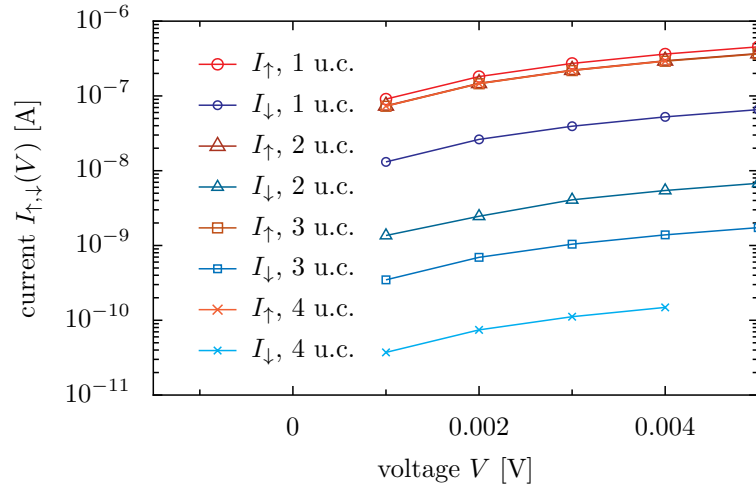


Figure 6.19: Spin resolved  $I$ - $V$  curves for up to four unit cells NiMnSb. The size of the scattering region only influences the minority spin currents, as is visible in the distance between the curves. Majority spin currents, with exception of the first, are nearly identical.

## 6.5 Conclusion

According to the previous four sections, the results of this chapter can be summarized as follows:

1. At the interface with the gold leads, the half-metallicity of the Heusler alloy NiMnSb, is always destroyed. This can be seen in the reduced density of states (which is the sum of the DOS over all Ni, Mn and Sb atoms) in Figs. 6.2, 6.4, and 6.7.
2. Although half-metallicity is lost at the interface, the transmission is highly spin polarized for more than one unit cell NiMnSb in the scattering region, and already for one unit cell it exceeds 77%, as seen in Fig. 6.20. This high spin polarization is attributed to the formation of a half-metallic area inside the scattering region.

The spacial separation of the non-half-metallic interface regions is a crucial factor which influences the spin polarized transmissions ( $P_T \geq 0.95$ ).

3. The transmission decreases with an increasing number of NiMnSb unit cells within the scattering region. This is also visible in Fig. 6.20, where the one-unit-cell transmission is generally larger than the two-unit-cell transmission and so on.

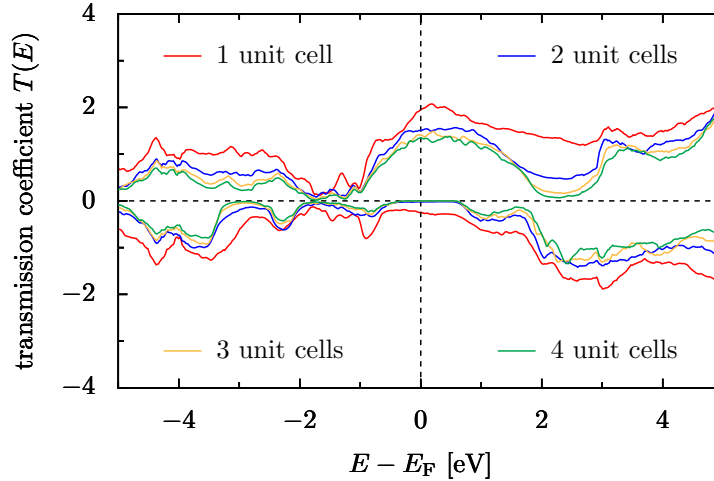


Figure 6.20: Comparison of the transmissions for different numbers of NiMnSb unit cells in the scattering region. Colors indicate number of cells. Positive transmission means majority spin, negative transmission means minority spin.

4. The voltage dependence of the transmission coefficient is negligible. The chosen voltage range for the current calculation goes from zero to 0.005 eV. High-voltage results for different transmissions are shown in Fig. 6.21. We observe only small changes even though the voltage exceeds the values from the previous calculations by a factor of 80.
5. Atomic relaxation plays only a minor role for transport properties. In the cases of one and two unit cells of NiMnSb in the scattering region, we tested different methods of atomic relaxation. One method included only a relaxation of the Heusler part of the scattering region, and the other also included the interface gold layers.

Although we found a considerable movement of the atoms, the electronic structure (as seen in the DOS Figs. 6.2, 6.4) and also the transmission (Fig. 6.13) show almost no difference.

This is a surprising result considering how huge differences with respect to the relaxation technique can be, which was investigated for the MgO/NiMnSb interface by ZHANG *et al.* [97] in an *ab initio* electronic structure analysis (no transport properties).

This is, however, consistent with our results. One reason for this is that a MgO/NiMnSb interface cannot be compared with a Au/NiMnSb interface since MgO is an insulator and Au is a metal. Another reason is that the interface properties do (almost) not contribute to the transmission as was seen in section 6.2 and the following.

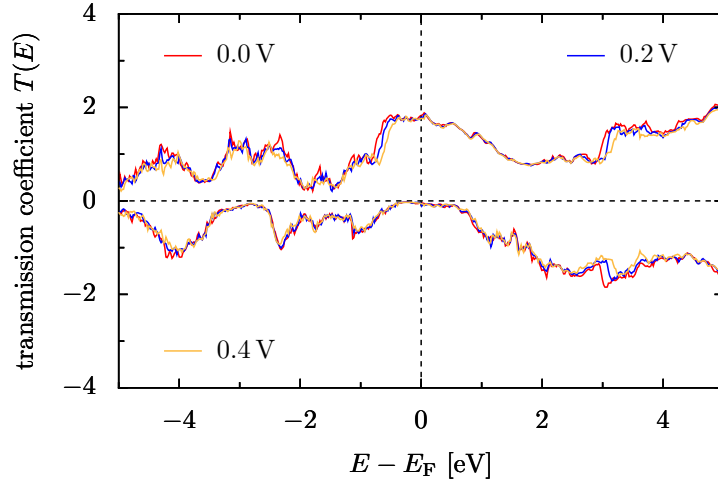


Figure 6.21: Comparison of the transmissions for two unit cells NiMnSb for different voltages. The transmission coefficients depend only weakly on the voltage, even though 0.2 V and 0.4 V are extremely high values compared to the values used throughout this chapter.

6. The transmission at the Fermi level for the minority spin channel decays exponentially with respect to the thickness of the scattering region. In Fig. 6.22 the logarithm of the minority spin transmission is plotted against the number of barriers for the Kronig-Penney model (section 4.3) (solid black line), and against the number of Mn/Sb (or Ni) layers in the scattering region of the SMEAGOL calculation, respectively. Note that the number of Mn/Sb layers is twice the number of cubic NiMnSb unit cells, so that a plot of the logarithmic transmission versus the number of cubic unit cells would yield a line with a slope twice as large.

The data from the SMEAGOL calculations can be fitted with linear regression (solid red lines). The resulting slopes of the fit lines ( $m_{S,\text{smooth}} = -1.06 \pm 0.10$ ,  $m_{S,\text{raw}} = -0.99 \pm 0.06$ ) are very similar to the one that belongs to the transmission in the Kronig-Penney model ( $m_K = -1.04$ ) in section 4.3, with a band gap of  $\Delta E = 2.64 E_H$ .

The agreement of the slopes is coincidental, but the exponential decay itself matches very well with the prediction from the Kronig-Penney model.

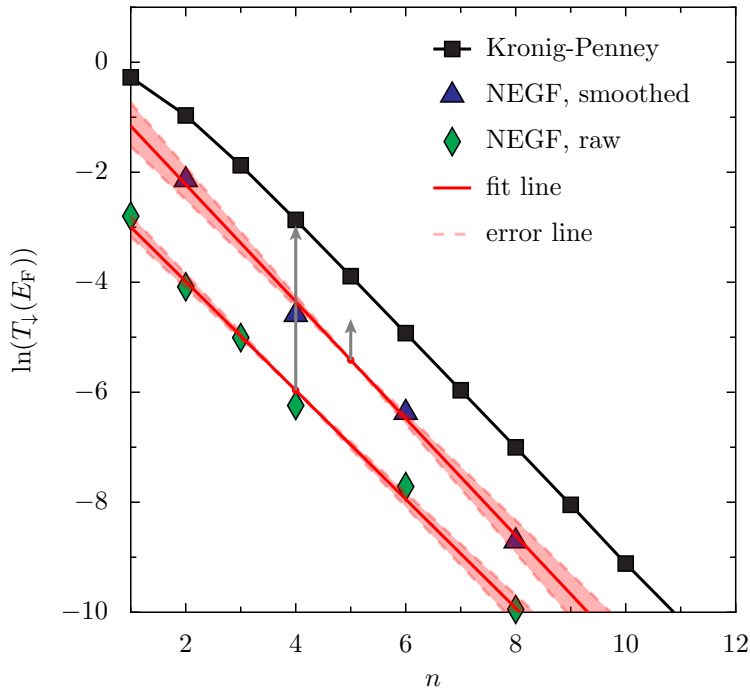


Figure 6.22: Logarithmic transmission at the Fermi level plotted against the number  $n$  of barriers (Kronig-Penney), or the number  $n$  of Mn/Sb layers (SMEAGOL, NEGF), respectively. Band gap size of the Kronig-Penney calculation is  $\Delta E = 2.64$ . The SMEAGOL data is shifted for visibility's sake. Arrows indicate the original positions.

# 7 Transmission with Defects

## Contents

---

<b>7.1 Vacancy at Ni site</b> . . . . .	<b>101</b>
<b>7.2 Unexpected Antiparallel Ordering</b> . . . . .	<b>110</b>
<b>7.3 Swapping of Mn and Ni</b> . . . . .	<b>114</b>
<b>7.4 Conclusion</b> . . . . .	<b>126</b>

---

In this section we consider lattice defects in the scattering region and their influence on the transport properties of the structure. The lattice defects were placed in a scattering region consisting of two unit cells NiMnSb, where the number of atoms is still relatively small but the scattering region is already large enough to create half-metallic transport properties. Among possible lattice defects one can distinguish between a) vacancies, b) additional atoms, and c) swapping of atoms. In this chapter examples for the first and for the third category are given. Representative for the first category we are examining the effects of a vacancy at a Ni site, and for the third category the example is a swapping of a Ni and a neighboring Mn atom. Unfortunately only preliminary results on other defects, such as vacancies at Mn or Sb sites or swapping of different elements are obtained (not shown). This is still under investigation. The procedure to incorporate lattice defects starts with the relaxation of the Heusler part of the scattering region using SIESTA only. Then a relaxation of the whole scattering region was done using SIESTA's Z-matrix formalism. When convergence for the structure relaxation was achieved, the relaxed structure was connected to the gold leads.

## 7.1 Vacancy at Ni site

### First Relaxation Method

At first we consider a vacancy at a Ni site. The vacated Ni site is positioned in the central (third) Ni layer in order to obtain a defect with a high level of symmetry. In the ideal structure the considered Ni layer has two atoms at positions  $(0, 0, z)$  and  $(\frac{a}{2}, \frac{a}{2}, z)$ . The atom at  $(0, 0, z)$  was removed. Therefore, the total number of atoms in the transport setup is reduced to 77. The total number of electrons is 758. For

the structure relaxation, which cannot be neglected in the case of lattice defects, especially for an invasive defect like a vacancy, two different approaches were made.

In the first approach, two cubic unit cells of NiMnSb were defined in a SIESTA calculation. Furthermore four of the remaining Ni atoms at the bottom and at the top of this two-unit-cell block were held fixed. A visual representation of the results of this relaxation process is shown in Figure 7.1. Since the missing Ni atom was positioned at the edge of the unit cell and the visual representation is for a closed cell, the vacancy is replicated four times, so that there are four vacancies in each picture. The green vectors depicted in Figure 7.1 represent the displacement of the atoms after the relaxation process. They are all normalized in order to be able to visualize various displacements of different magnitude. The actual length of each vector can be found in Tab. 7.1.

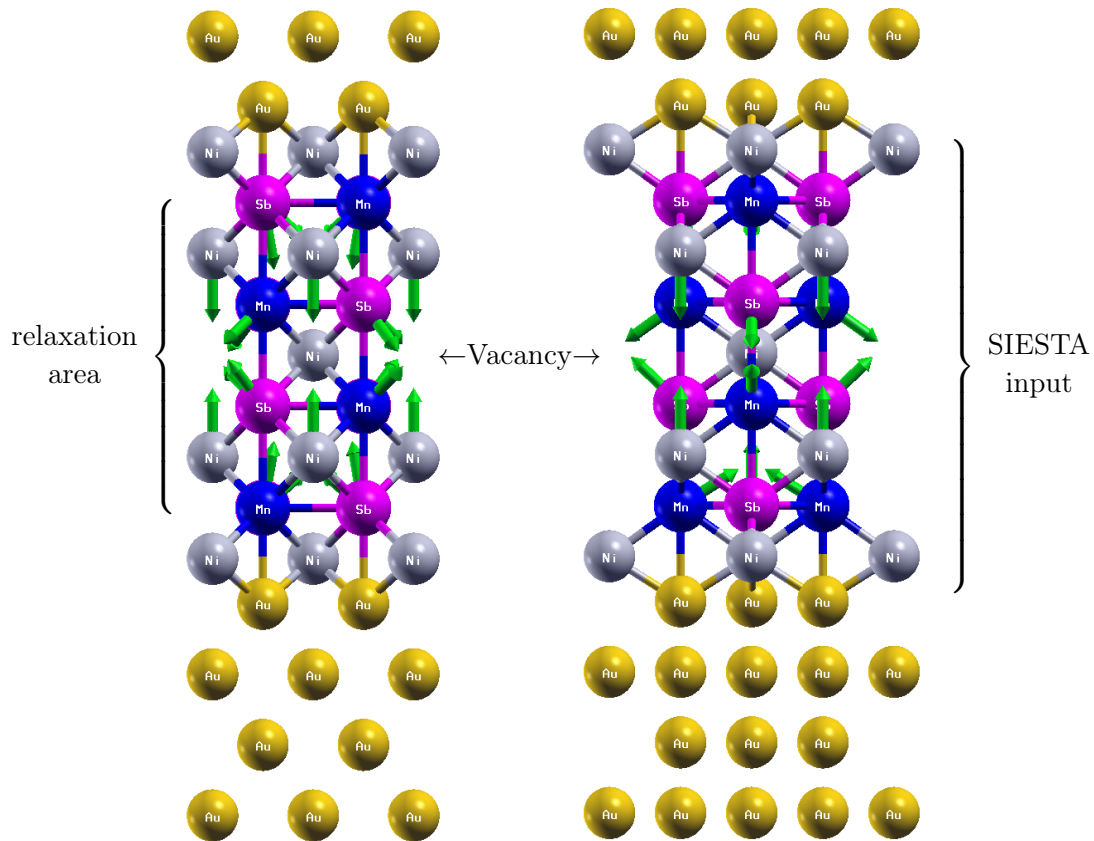


Figure 7.1: Displacement of atoms for the first relaxation method from the [100] (left) and [110] (right) view. Due to the closed representation there are four vacancies in each picture instead of one. For absolute values see Tab. 7.1.

The most drastic movement was observed for the Mn atoms in the two layers next to the defect with a total displacement of 0.085 Å. The direction of the displacement points directly to the vacated Ni site as seen in the picture. The second largest displacement with a value of 0.012 Å was observed for the Mn atoms in the first and fourth Mn/Sb layer. Opposing to the Mn atoms in the other two layers, these Mn atoms move away from the vacancy, which can be seen best in the first (from the bottom) Mn/Sb layer in the right picture of Figure 7.1, where the [110] view on the structure is shown. The third furthest movement with a total distance of 0.007 Å was found for the Sb atoms in the second and third Mn/Sb layer next to the defect. Following the behaviour of their neighbouring Mn atoms, the Sb also move towards the vacancy which can be seen in the [100] as well as the [110] view. The Ni atoms in the second and fourth Ni layer are moved only by a small distance of 0.003 Å.

If one looks at the structure from the [100] view (left panel) one might assume that the Ni atoms are displaced towards the vacated Ni site in the central Ni layer. However, this is not true as can be seen in the right picture showing the [110] view. The Ni atoms in the second Ni layer simply move straight upwards, and the Ni atoms in the fourth layer move straight downwards. The wrong impression from the [100] view comes from the difference in the  $y$ -coordinate of the vacancy and the Ni

Layer	Atom	Relative (x,y)-positions	Displacement
Interface Ni layer	Ni	$(0, 0), (\frac{1}{2}, \frac{1}{2})$	fixed
1st Mn/Sb layer	Mn	$(\frac{1}{4}, \frac{1}{4}), (\frac{3}{4}, \frac{3}{4})$	0.012 Å
	Sb	$(\frac{1}{4}, \frac{3}{4}), (\frac{3}{4}, \frac{1}{4})$	0.001 Å
2nd Ni layer	Ni	$(0, \frac{1}{2}), (\frac{1}{2}, 0)$	0.003 Å
2nd Mn/Sb layer	Mn	$(\frac{1}{4}, \frac{3}{4}), (\frac{3}{4}, \frac{1}{4})$	0.085 Å
	Sb	$(\frac{1}{4}, \frac{1}{4}), (\frac{3}{4}, \frac{3}{4})$	0.007 Å
Central Ni layer	Ni	$(0, 0)$	removed
	Ni	$(\frac{1}{2}, \frac{1}{2})$	0.000 Å
3rd Mn/Sb layer	Mn	$(\frac{1}{4}, \frac{1}{4}), (\frac{3}{4}, \frac{3}{4})$	0.085 Å
	Sb	$(\frac{1}{4}, \frac{3}{4}), (\frac{3}{4}, \frac{1}{4})$	0.007 Å
4th Ni layer	Ni	$(0, 0), (\frac{1}{2}, \frac{1}{2})$	0.003 Å
4th Mn/Sb layer	Mn	$(\frac{1}{4}, \frac{3}{4}), (\frac{3}{4}, \frac{1}{4})$	0.012 Å
	Sb	$(\frac{1}{4}, \frac{1}{4}), (\frac{3}{4}, \frac{3}{4})$	0.001 Å
Interface Ni layer	Ni	$(0, 0), (\frac{1}{2}, \frac{1}{2})$	fixed

Table 7.1: Total displacement of each atom in the Heusler part of the scattering region. The high symmetry of the defect is reflected in the symmetric distribution of displacements.

atoms in the neighboring Ni layers that is not visible in that perspective.

The smallest movement of all atoms in the relaxation area was observed for the Sb atoms in the first and fourth Mn/Sb layer with a total displacement of less than  $0.001 \text{ \AA}$ . These Sb atoms, just like their neighboring Mn atoms, move towards the center of the structure, where the remaining Ni atom is located. A difference to the movement in the inner Mn/Sb layer lies in the angle in which the specific atoms move. While for the inner two layers, the angles for Mn and Sb are approximately the same, this does not hold for the outer two layers. There, the movement of the Sb atoms is considerably steeper than the movement of Mn atoms.

In this paragraph the results of the transport calculation shall be discussed. For the relaxed structure, convergence in the transport calculation was achieved after 112 iterations. The EMPDOS, provided by SMEAGOL, for the inner unit cell as defined in Fig. 6.10 is shown in Fig. 7.2. This DOS looks very similar to the DOS of the inner unit cell for the case without a lattice defect (Fig. 6.9). An interesting difference is the size of the “gap”, which shrank from about  $0.7 \text{ eV}$  in the clean system to only  $0.4 \text{ eV}$  in this case. A closer look into the PDOS of the inner unit cell reveals that the Mn atoms in the layers next to the defect as well as the Ni atoms in the neighboring Ni layers are responsible for the closing of the gap.

As we learned in the previous paragraph, the Mn atoms are moving towards the empty space created by the vacancy, thus increasing the distance to the neighboring Ni atoms in the central as well as to the other neighboring layer. A crucial factor

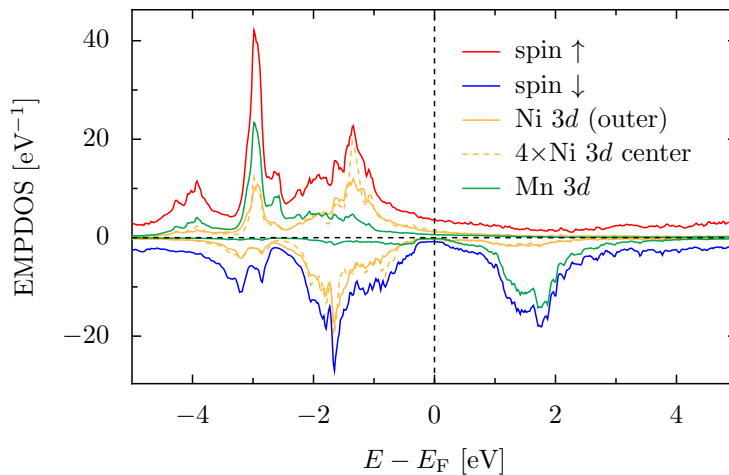


Figure 7.2: EMPDOS for the inner unit cell containing the lattice defect. Although the DOS does not vanish around the Fermi level, the polarization is still very high.

for the half-metallicity in NiMnSb is the bonding (antibonding) of Ni with Mn since the  $d$ -orbitals of Ni are lowered, and the  $d$ -orbitals of Mn are increased in energy. Each Mn atom has four neighboring Ni atoms and thus the considered vacancy has a huge influence on the Ni-Mn bonding.

Considering the transmission coefficient as seen in Fig. 7.3 we see, that around the Fermi level the spin polarization is, with a value of  $P_T = 0.95$ , still very high. A comparison with the transmission of the clean structure (Fig. 6.8) shows that the majority spin channel is less affected by the vacancy. In the minority spin channel the gap in the transmission is smaller than the gap in the clean structure, thus following the trend that was already visible in the DOS for the inner unit cell. Another difference between these two transmissions can be found around 2 eV below the Fermi level, there the transmission in the case of the vacancy is considerably smaller than in the clean case. However, since this difference is far away from the Fermi level compared to an energy range defined by room temperature (30 meV), its influence on transport properties is negligible.

Thus, we can summarize that, under the specific relaxation process described at the beginning of this section, that a vacancy at a Ni site does not destroy half-metallic transport. It is important to point out that the defect was placed in the central region of the scattering region where the half-metallic, bulk-like electronic structure was formed. This result is promising with respect to possible applications, since the influence of the interface region is neglectable as long as a half-metallic behaviour in the center can be found.

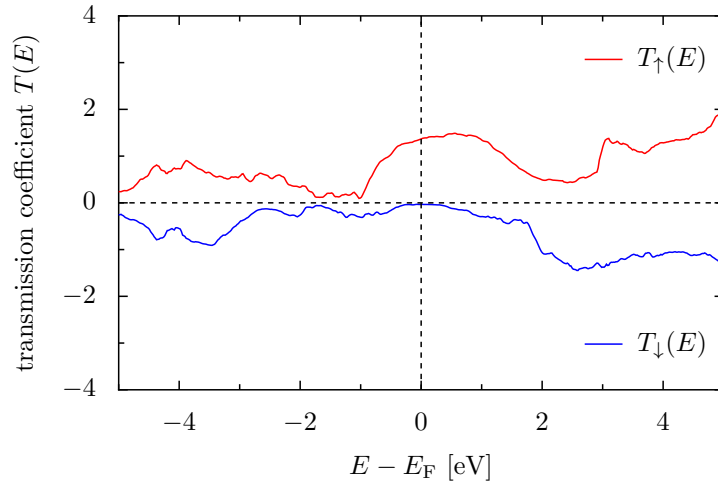


Figure 7.3: Transmission coefficient for two NiMnSb unit cells in the scattering region with a vacated Ni site in the central Ni layer. For the minority spin channel the transmission has a gap around the Fermi level.

## Second Relaxation Method

The second method of relaxation also contains the gold layers at the interface. The supercell for the SIESTA input consisted of two unit cells NiMnSb and additionally five layers of gold. Three of those gold layers were fixed and the two layers at the interface were free to move in any direction. In order to maintain a high level of symmetry, the central Ni atom was also fixed in its  $z$ -coordinate.

In this relaxation process the hierarchy of furthest movement differs from the previous relaxation method. The directions of the specific movements can be seen in Fig. 7.4 and the absolute values of the displacement can be found in Tab. 7.3.

The largest displacement can now be found for the Ni atoms in the interface layers. However, not the Ni atom that lies directly above (or below) the vacancy

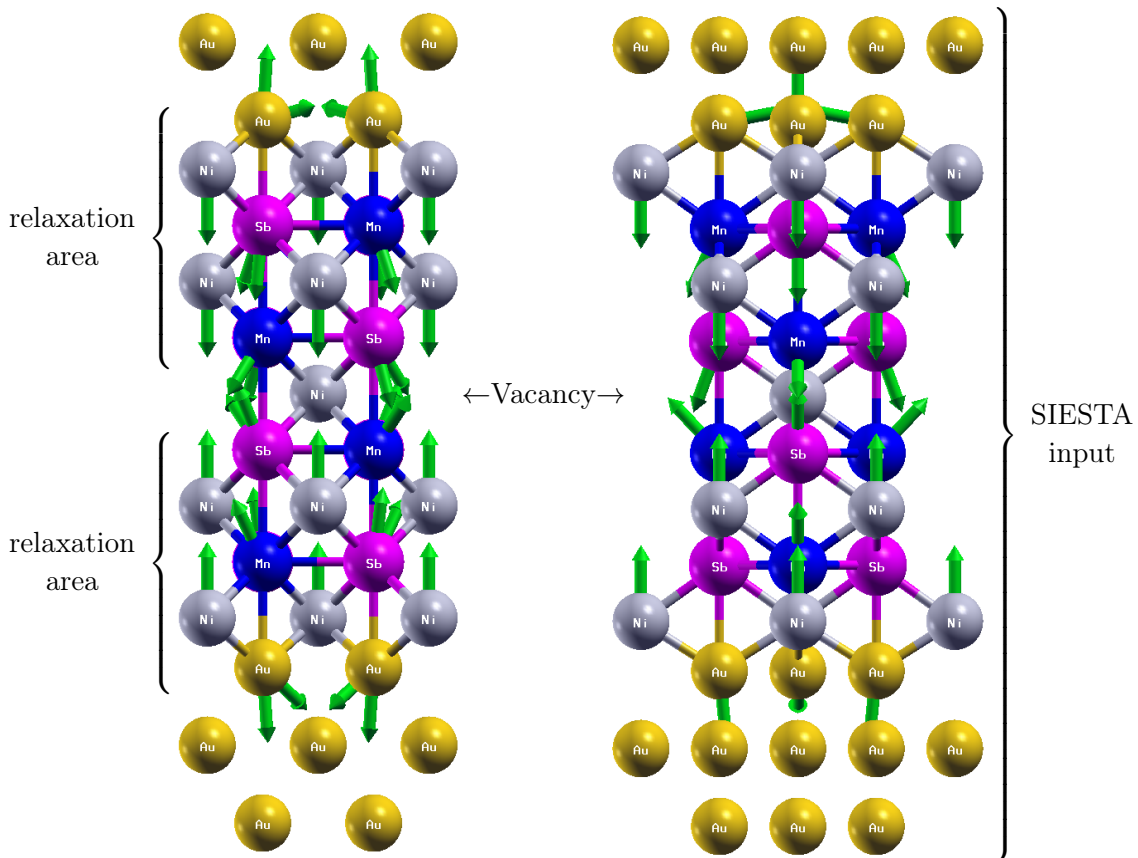


Figure 7.4: Displacement of atoms for the second relaxation method from the [100] (left) and [110] (right) view. Due to the closed representation there are four vacancies in each picture instead of one.

has the largest displacement, but the other Ni atom that lies vis-à-vis the central remaining Ni atom with a movement of 0.20 Å. The other Ni atom in that layer (the one that lies above (or below) the vacancy) is also moving a lot, with a total displacement value of 0.10 Å. The direction of their movement is again straight downwards (or upwards) as can be seen in Figure 7.4, a behaviour which we already know from the last method. If we take a look at the Mn/Sb layers next to the lattice defect, we see a very similar behaviour compared to the one observed with the last method. The Mn atoms move towards the vacancy and thus are displaced by 0.12 Å, which is more than last time. The Sb atoms in this layer also move towards the vacancy but only travel a distance of roughly 0.03 Å.

Although also here the Sb distance is smaller than the Mn distance, the relation between the distances differs significantly. In the last method, the Mn atoms moved

Layer	Atom	Relative (x,y)-positions	Displacement
Interface Au layer	Au	$(\frac{1}{4}, \frac{1}{4}), (\frac{3}{4}, \frac{3}{4})$	0.018 Å
	Au	$(\frac{1}{4}, \frac{3}{4}), (\frac{3}{4}, \frac{1}{4})$	0.111 Å
Interface Ni layer	Ni	(0, 0)	0.105 Å
	Ni	$(\frac{1}{2}, \frac{1}{2})$	0.203 Å
1st Mn/Sb layer	Mn	$(\frac{1}{4}, \frac{1}{4}), (\frac{3}{4}, \frac{3}{4})$	0.039 Å
	Sb	$(\frac{1}{4}, \frac{3}{4}), (\frac{3}{4}, \frac{1}{4})$	0.067 Å
2nd Ni layer	Ni	$(0, \frac{1}{2}), (\frac{1}{2}, 0)$	0.077 Å
2nd Mn/Sb layer	Mn	$(\frac{1}{4}, \frac{3}{4}), (\frac{3}{4}, \frac{1}{4})$	0.129 Å
	Sb	$(\frac{1}{4}, \frac{1}{4}), (\frac{3}{4}, \frac{3}{4})$	0.032 Å
Central Ni layer	Ni	(0, 0)	removed
	Ni	$(\frac{1}{2}, \frac{1}{2})$	fixed
3rd Mn/Sb layer	Mn	$(\frac{1}{4}, \frac{1}{4}), (\frac{3}{4}, \frac{3}{4})$	0.119 Å
	Sb	$(\frac{1}{4}, \frac{3}{4}), (\frac{3}{4}, \frac{1}{4})$	0.021 Å
4th Ni layer	Ni	$(0, 0), (\frac{1}{2}, \frac{1}{2})$	0.064 Å
4th Mn/Sb layer	Mn	$(\frac{1}{4}, \frac{3}{4}), (\frac{3}{4}, \frac{1}{4})$	0.030 Å
	Sb	$(\frac{1}{4}, \frac{1}{4}), (\frac{3}{4}, \frac{3}{4})$	0.057 Å
Interface Ni layer	Ni	(0, 0)	0.092 Å
	Ni	$(\frac{1}{2}, \frac{1}{2})$	0.190 Å
Interface Au layer	Au	$(\frac{1}{4}, \frac{1}{4}), (\frac{3}{4}, \frac{3}{4})$	0.116 Å
	Au	$(\frac{1}{4}, \frac{3}{4}), (\frac{3}{4}, \frac{1}{4})$	0.020 Å

Table 7.2: Total displacement of each atom in the relaxation area of the scattering region. This method shows a lower symmetry.

ten times further than the Sb atoms, but in this method the factor is only 4. The Ni atoms in the second and fourth Ni layer moved about  $0.07 \text{ \AA}$  which is also significantly more than what was observed with the other method.

If we look at the first and fourth Mn/Sb layer near the interface, we can observe a opposing behaviour compared to the first relaxation process. While in that method the Mn and Sb atoms moved towards the center, away from the vacancy, here the atoms move towards the vacancy. Like in the first method, the Mn atoms with  $0.06 \text{ \AA}$  moved more than the Sb atoms with only  $0.03 \text{ \AA}$ .

For the Au atoms at the interface we can observe two different movement types. The Au atoms that are closer to the Sb atoms show a larger displacement of about  $0.11 \text{ \AA}$  and move away from the Heusler alloy, whereas the Au atoms lying near the Mn atoms move only about  $0.02 \text{ \AA}$ . The direction of their movement points more towards the symmetry axis of the structure.

Although some atoms show a completely different movement pattern in the second relaxation method, the DOSs for the inner unit cell are extremely similar, as is seen in Fig. 7.5. Especially around the Fermi level and in particular for the minority spin channel both DOSs are almost identical.

The transmission coefficients for both relaxation methods are shown in Fig. 7.6 where more emphasis was put on the energy range around the Fermi level. For the majority spin channel minor differences are visible but the overall behavior is the same. The minority spin channel, which is even more interesting with regard to spin-polarization and half-metallic transport, shows even less differences. At the Fermi level, both transmissions are flat and extremely small, although not numerically

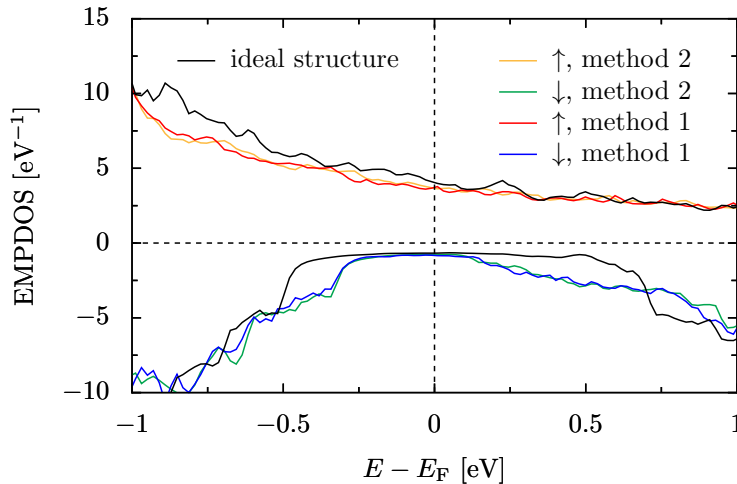


Figure 7.5: Projected density of states of the inner unit cell for both relaxation methods. Almost no difference is seen.

zero. For the majority spin channel, at the Fermi level, the second method yields a transmission that shows an almost linear behaviour which makes this method more suitable to calculate transport coefficients, like Peltier or Seebeck-coefficients, because the slope of the transmission at the Fermi level is more well defined. The difference in the total energy between the two methods is 1.36 eV, with method 2 resulting in the more stable structure. This is a huge value compared to thermal fluctuations, but still the electronic structure and also the transport properties seem to be unaffected by these changes in the crystal structure.

Regarding the spin polarization of the transmission, we find a value of  $P_T = 0.948$  for the first relaxation method and a value of  $P_T = 0.952$  for the second method. The differences between those values are rather small if one considers the majority spin channels at the Fermi level. The transmission spin polarization is even slightly higher for the first relaxation method although the majority spin transmission is higher for the second method. The difference to the transmission polarization of the ideal structure, which is  $P_T = 0.972$ , is very small.

The results so far support the findings of the last chapter in the sense that structure relaxation does not play a major role when it comes to transport properties. Summarizing, we can say that Ni vacancies, even for an immense concentration of 50% of the atoms in a specific layer, do not diminish the spin polarization of the transmission by a large margin. Regarding the relaxation process, method 2 is preferred because it yields the more stable structure.

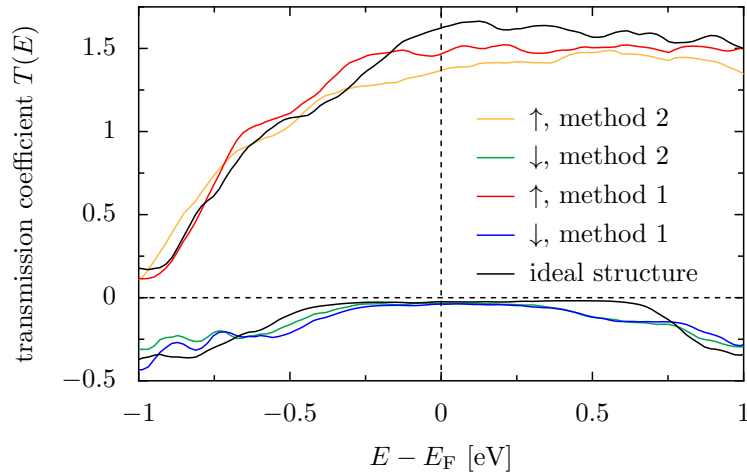


Figure 7.6: Transmission coefficient around the Fermi level for both relaxation methods. For the minority spin channel, especially around the Fermi level, both methods yield the same results.

## 7.2 Unexpected Antiparallel Ordering

In this section we want to present a calculation on the vacated Ni lattice defect. Although convergence was achieved after 12 iteration, a comparison of the resulting total energy with the previous calculation in sec. 7.1 shows that in this case the resulting electronic structure belongs only to a local energy minimum. This means that the result corresponds to a meta-stable state in reality. However, this state exhibits some interesting features that should be discussed nevertheless.

In the last few sections we first considered the DOS and thereafter the transmission coefficient. In this section, however, we present the transmission first, as the oddity of this calculation is already clearly visible in the transmission and shall then be explained using the DOS.

In Fig. 7.7 the transmission for this specific calculation is shown. A comparison with the transmission in Fig. 7.3 for the same defect shows a very similar transmission for energies far away from the Fermi level. For energies in a quite large range around the Fermi level however, both figures differ significantly. Regarding the majority spin channel, we can see that the transmission is drastically reduced within this energy range. For the minority spin channel on the other hand, we can observe an increase of the transmission coefficient, at least in a small energy range around the Fermi level of about  $\pm 0.50$  eV. The shape of the transmission curve for these energies is reminiscent of the minority spin transmission without lattice defect for only one unit cell of NiMnSb inside the scattering region (see Fig. 6.5). In order to see if there is any connection between these two different calculations it is important to learn more about the electric and magnetic structure that was established in this specific case.

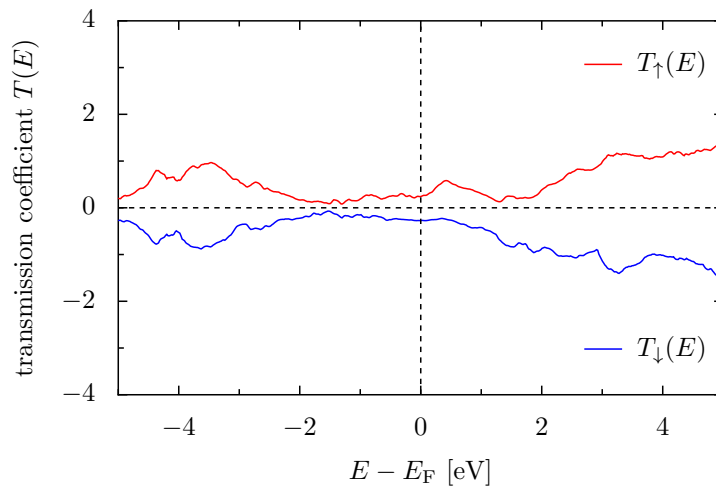


Figure 7.7: Transmission coefficient for the unexpected antiparallel ordering in the Ni vacated structure.

This can, of course, only be done by considering the PDOS of the scattering region. The PDOS for the inner unit cell, which also contains the vacancy, is shown in Fig. 7.8. When this DOS is compared to the corresponding plot in Fig. 7.2 for the same defect, it is obvious that the differences are very subtle.

For the majority spin channel, all the relevant peaks can be found in both cases at the same energies, and for the minority spin channel the same is true. The most significant difference between this calculation and the previous one can be found around the Fermi level in the minority spin channel, where the band gap not only shrunk, but is now completely closed.

A more detailed analysis of the DOS can be seen in Fig. 7.9, where the PDOS of the four Mn/Sb layers is shown and compared with the clean structure's DOS. In a) and d) the DOS plots of the outer two Mn/Sb layers are shown. There, the biggest difference between this calculation and the clean structure is visible. The black curves for the clean structure have almost the same shape as the coloured curves for this case but for the respective other spin channel. This means that the magnetic moment of these layers have a different sign as in the clean structure and also, as is shown in b) and c), a different sign as for the inner two Mn/Sb layers. When the DOS for the inner two layers is compared to the DOS for the clean structure, we can see that the magnetic moment is roughly the same. Unlike the clean structure, the vacated Ni structure shows a large DOS around the Fermi level, which indicates that in this structure there is no half-metallic inner unit cell.

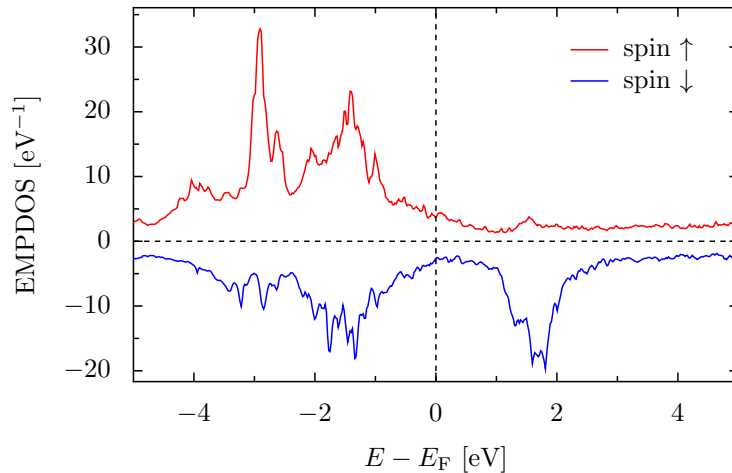


Figure 7.8: Projected density of states for the inner unit cell of the antiparallel ordered vacated Ni structure.

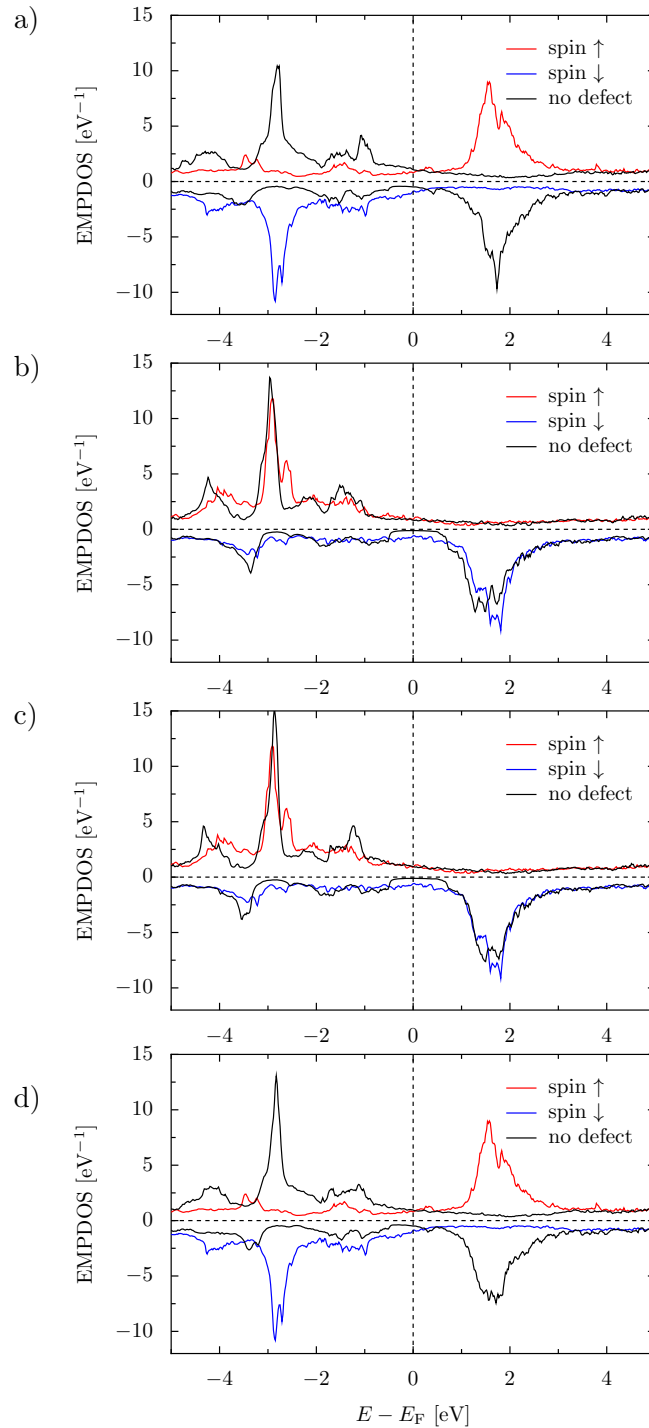


Figure 7.9: Projected density of states of the four Mn/Sb layers. a) shows the first layer, b) the second, c) the third, and d) the fourth.

A key finding of the last chapter was that a half-metallic inner unit cell is necessary for developing a strongly spin-polarized transmission. The lack of that feature in this structure can explain the relatively high transmission around the Fermi level in the minority spin channel. The unusually small transmission for the majority spin channel however, cannot be explained by that.

There is, however, an interpretation of the data that explains the resulting transmission. As we saw in Fig. 7.9, the magnetic moment of the inner unit cell has the same sign as we would expect from previous calculations. The rest of the Heusler part of the scattering region, on the other hand, is polarized in the opposite direction. This means that in essence, there are two unit cells of NiMnSb, which act as spin filter, but with different polarization. The inner unit cell suppresses the minority spin transmission and the bottom half of the first, as well as the top part of the second unit cell, on the other hand, suppress the minority spin transmission. That way, the transmission is relatively low for both spin channels, comparable with the minority spin transmission for only one unit cell NiMnSb.

In Fig. 7.10 the spin-polarized current for this configuration is depicted. We observe that the two currents are almost identical. This reflects the low spin polarization that was already visible in the transmission plot in Fig. 7.7. In addition to the spin resolved currents of this configuration, the minority spin current of the ideal one-unit-cell case is also depicted (black line). The similarity of the three  $I$ - $V$  plots furthermore underlines the interpretation that this configuration acts like a series of two spin filters with different polarization and therefore agrees with the informations from the transmission coefficient. Although the configuration itself may not be physically relevant, this result fits into the picture we drew of NiMnSb in the last chapters.

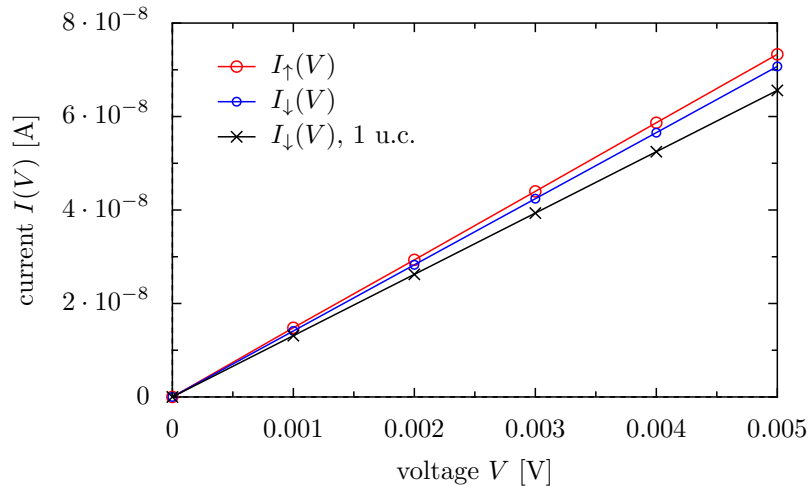


Figure 7.10: Spin-resolved current for the antiparallel ordered structure and minority spin current for the ideal one-unit-cell case.

### 7.3 Swapping of Mn and Ni

In this section, the defect under consideration is the swapping of atomic positions of adjacent Ni and Mn atoms. Due to the similarity of their respective atomic numbers, 28 for Ni and 25 for Mn, this swapping is more likely to happen than other constellations with the much larger Sb (atomic number 58). In the following example the implementation of this specific defect was done in a scattering region that contained two cubic unit cells of NiMnSb. The defect was located in the central part of the scattering region, as one Ni atom in the central third Ni layer was exchanged with a neighboring Mn atom in the layer below. The relaxation of the structure was done with method 2 introduced in sec. 7.1, i.e. including the first gold layers next to the Heusler alloy to the relaxation area.

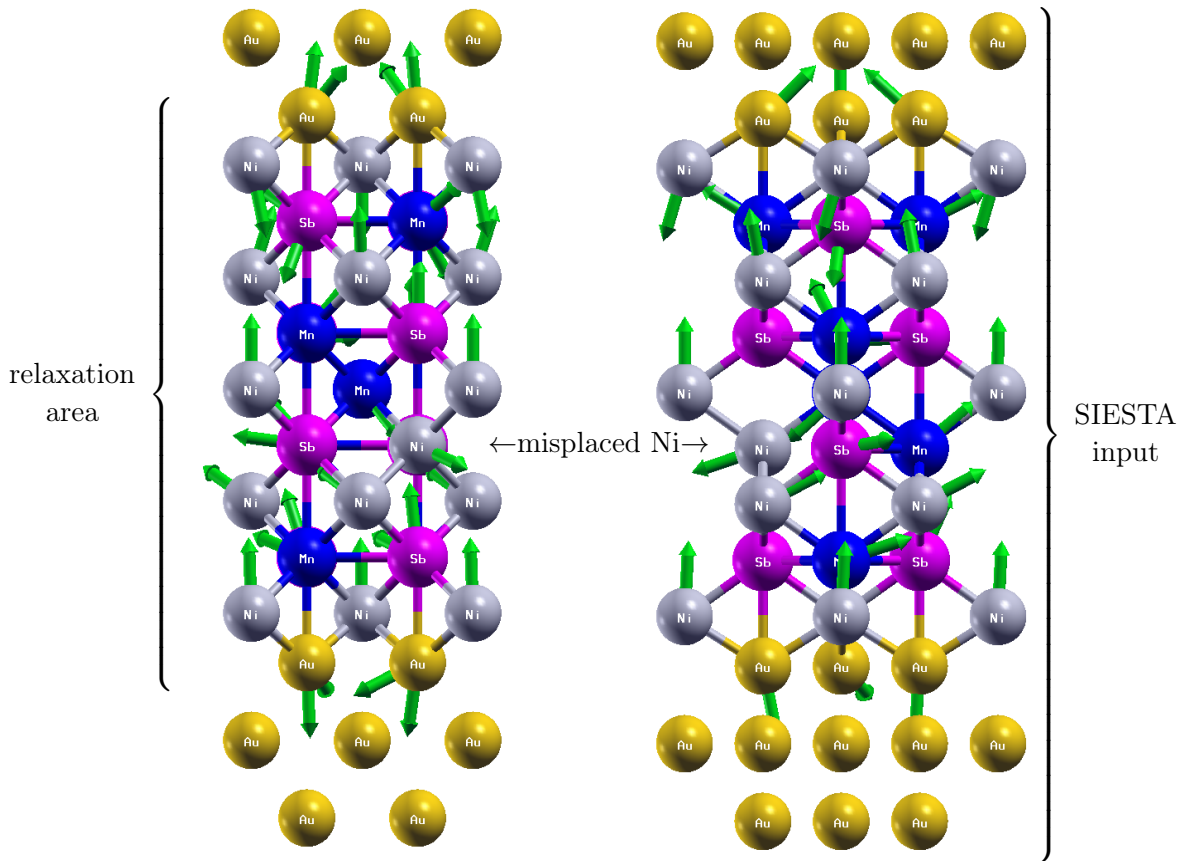


Figure 7.11: Displacement of atoms for the second relaxation method from the [100] (left) and [110] (right) view. The misplaced Mn atom lies in the layer above the (marked) misplaced Ni atom.

The movement of the atoms is depicted in Fig. 7.11. The furthest movement was observed in the central Ni layer, where one Ni atom was exchanged with manganese. The remaining Ni atom showed a movement of 0.24 Å that was directed “upwards”, i.e. away from the misplaced Ni atom in the Mn/Sb layer below.

The misplaced Mn atom in the Ni layer moved towards its old position by a distance of also 0.24 Å. The misplaced Ni atom in the adjacent Mn/Sb layer moves approximately in the same direction, i.e. slightly downwards and outwards but with a distance of 0.15 Å not as much as the other misplaced atom.

In the second and fourth Ni layer the movement is already much smaller than in the central one. For the second Ni layer, which is closer to the defect, the displacement is

Layer	Atom	Relative (x,y)-positions	Displacement
Interface Au layer	Au	$(\frac{1}{4}, \frac{1}{4}), (\frac{3}{4}, \frac{3}{4})$	0.050 Å
	Au	$(\frac{1}{4}, \frac{3}{4}), (\frac{3}{4}, \frac{1}{4})$	0.130 Å
Interface Ni layer	Ni	(0, 0)	0.006 Å
	Ni	$(\frac{1}{2}, \frac{1}{2})$	0.202 Å
1st Mn/Sb layer	Mn	$(\frac{1}{4}, \frac{1}{4}), (\frac{3}{4}, \frac{3}{4})$	0.046 Å
	Sb	$(\frac{1}{4}, \frac{3}{4}), (\frac{3}{4}, \frac{1}{4})$	0.030 Å
2nd Ni layer	Ni	$(0, \frac{1}{2}), (\frac{1}{2}, 0)$	0.025 Å
2nd Mn/Sb layer	Mn	$(\frac{1}{4}, \frac{3}{4}), (\frac{3}{4}, \frac{1}{4})$	0.056 Å
	Sb	$(\frac{1}{4}, \frac{1}{4}), (\frac{3}{4}, \frac{3}{4})$	0.101 Å
Central Ni layer	Ni	(0, 0)	0.240 Å
	<b>Mn</b>	$(\frac{1}{2}, \frac{1}{2})$	0.239 Å
3rd Mn/Sb layer	Mn	$(\frac{1}{4}, \frac{1}{4})$	0.106 Å
	<b>Ni</b>	$(\frac{3}{4}, \frac{3}{4})$	0.150 Å
	Sb	$(\frac{1}{4}, \frac{3}{4}), (\frac{3}{4}, \frac{1}{4})$	0.180 Å
4th Ni layer	Ni	$(0, 0), (\frac{1}{2}, \frac{1}{2})$	0.144 Å
4th Mn/Sb layer	Mn	$(\frac{1}{4}, \frac{3}{4}), (\frac{3}{4}, \frac{1}{4})$	0.084 Å
	Sb	$(\frac{1}{4}, \frac{1}{4}), (\frac{3}{4}, \frac{3}{4})$	0.110 Å
Interface Ni layer	Ni	(0, 0)	0.093 Å
	Ni	$(\frac{1}{2}, \frac{1}{2})$	0.192 Å
Interface Au layer	Au	$(\frac{1}{4}, \frac{1}{4}), (\frac{3}{4}, \frac{3}{4})$	0.104 Å
	Au	$(\frac{1}{4}, \frac{3}{4}), (\frac{3}{4}, \frac{1}{4})$	0.021 Å

Table 7.3: Total displacement of each atom in the relaxation area of the scattering region. Since the defect does not respect the symmetry of the ideal structure, the displacements also do not reflect any symmetry.

about  $0.14 \text{ \AA}$  whereas the displacement for the fourth Ni layer is even smaller with only  $0.02 \text{ \AA}$ . The same tendency can be observed for the first and fourth Mn/Sb layer, where the first shows a movement of  $0.10 \text{ \AA}$  in average, and the fourth moves about  $0.04 \text{ \AA}$  in average.

In both of those layers the atom with the strongest movement was found at the site with the same  $x$ - and  $y$ -coordinate as the misplaced Ni atom. The two next neighbours in that layer on the other hand showed the smallest displacement. For the gold layers next to the Heusler alloy a similar behaviour as in the other relaxation processes was found. The gold layer tends to move away from the Heusler alloy where the gold atoms that are facing Sb atoms are moving more than the gold atoms that are facing Mn atoms.

The outer Ni layers, just like in the other relaxation processes, tend to move towards the central region. In those two layers, the Ni atoms on the edges of the unit cell show a relatively small displacement, whereas the Ni atom in the middle moves at least twice as far. The Ni atoms in the middle move by the same distance in both layers, while the atoms on the edges do not. In the case of the Ni layer that is farther away from the misplaced Mn atom, the movement is much smaller than in the nearer Ni layer.

The total DOS for the inner unit cell can be seen in Fig. 7.12. A comparison with the corresponding DOS plots for the clean structure (Fig. 6.9) or the structure with the vacated Ni site (Fig. 7.2) yields the same characteristic features in the energy

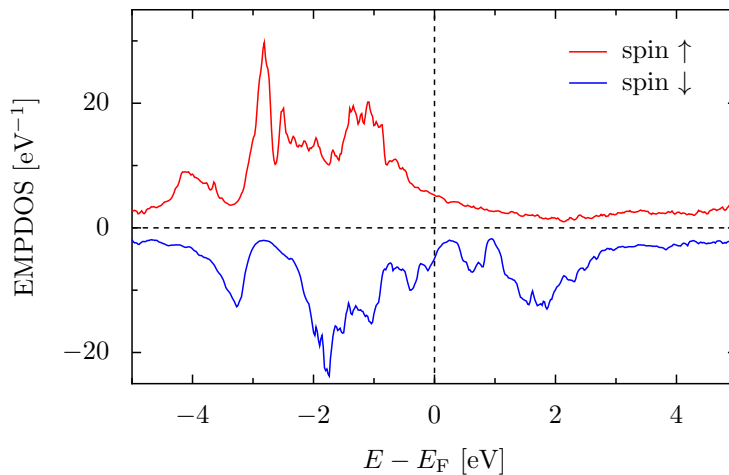


Figure 7.12: Total density of states for the closed inner unit cell of NiMnSb including a swapping of a Ni and a Mn atom. The half-metallic gap in the minority spin channel is completely destroyed.

regions away from the Fermi level. However, around the Fermi level, especially in the minority spin channel, a significant enhancement of the DOS is present.

To further investigate the origin of this enhanced DOS a more detailed plot, constrained to a smaller energy range, is given in Fig. 7.13. The black curve represents the total DOS of the inner unit cell according to Fig. 7.12 for a narrower energy range. The red curve represents the total DOS of all the six Ni atoms of the inner unit cell, and the blue curve the total DOS of all four Mn atoms, respectively. The sum of the blue and red curve matches the black curve quite well. This means that the Sb part to the enhanced DOS in the minority gap is very small. The two other curves that are labeled with “...defect side” show the DOS for a subset of the atoms that were considered for the red and blue curves. In case of the Ni atoms, this subset contains four Ni atoms. Two of them are located in the 4th Ni layer (compare Tab. 7.3), one in the 3rd Mn/Sb layer and one in the central Ni layer. In case of the Mn atoms this subset consists of two atoms, one in the 3rd Mn/Sb layer, and one in the central Ni layer.

The idea behind this is to evaluate the influence of the asymmetry that this specific defect generates. If the curve for a specific atomic species and the “defect side” curve for the same species are very similar, the shares to the enhanced DOS are distributed unequally, thus reflecting the asymmetric nature of the defect. This feature is, for example, strongly pronounced for the Ni atoms around the Fermi level, especially for the minority spin channel. Considering Mn, an asymmetry effect would be evident if the “defect side” DOS is significantly larger than the total

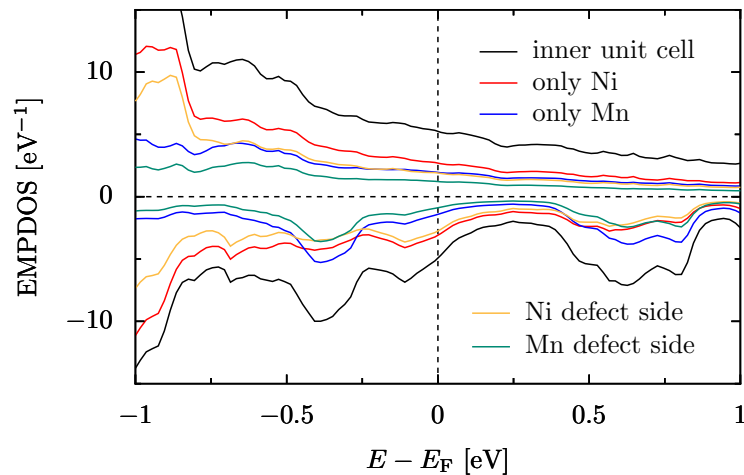


Figure 7.13: Comparison of the total with the species resolved density of states. The curves labeled with “...defect side” represent the DOS for the specific species on the side of the inner unit cell that contains the defect.

Mn DOS, divided by two. This is because the defect side contains two Mn atoms and the inner unit cell, as a whole, contains four Mn atoms. In the energy ranges between  $-0.50\text{ eV}$  and  $-0.25\text{ eV}$  below the Fermi level and between  $0.50\text{ eV}$  and  $0.80\text{ eV}$  above the Fermi level, the defect side DOS clearly exceeds half of the total Mn DOS.

The conclusion one can draw from the information in Fig. 7.13 is that in the minority spin channel, the enhancement of the DOS around the Fermi level can be mainly assigned to the two misplaced atoms whereas their well-positioned bonding partners only play a minor role. In Fig. 7.14 an orbital resolved DOS of the swapped atoms is compared to the total DOS of the respective species in the inner unit cell. The black curve is the minority spin total DOS of the inner unit cell for the clean structure in order to give an impression of the position of the half-metallic gap.

Considering that the blue curve represents a sum over the DOSs of four atoms and the red curve of six atoms, and that the green and yellow-orange curves each represent only the  $3d$  orbitals of a single atom, the importance of the  $d$ - $d$  bonding (anti-bonding) on the increased DOS becomes very clear. At around  $0.4\text{ eV}$  below the Fermi level we can see an increased DOS for the  $3d$  orbitals for both swapped atoms. This indicates the existence of a bonding hybridization of those  $d$  orbitals. A similar behavior can be observed at around  $0.5\text{ eV}$  above the Fermi level, where the PDOS of the swapped atoms also increases simultaneously.

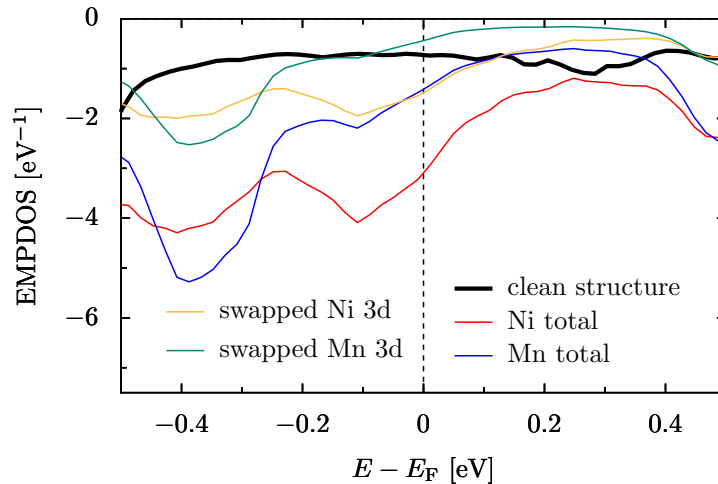


Figure 7.14: Comparison of the species resolved density of states with the  $3d$  orbital PDOS of the swapped atoms. The black curve represents the clean structure, to show the band gap.

The transmission calculated for this transport problem is shown in Fig. 7.15. When only the majority spin channel is considered, the transmission is very similar to the clean case (Fig. 6.8) or to the case with the Ni vacancy (Fig. 7.3). For the minority spin channel similar results can be found, especially in the energy range far away from the Fermi level. The two peaks at around 4 eV below the Fermi level, as well as the two smaller local maxima of the transmission at roughly  $-2$  eV and  $-1$  eV, can be found in any transmission plot we have seen so far. Also the drastically increasing transmission at around 2 eV is a feature well known from the other transmission calculations.

The huge difference compared to the previous calculations comes up when we consider a smaller energy range around the Fermi level, which is shown in the inset of Fig. 7.15. In that energy range the shape of the transmission curve is very similar to the shape of the DOS including the two local maxima at  $-0.4$  eV and  $-0.1$  eV with respect to the Fermi level, as well as the drop at roughly 0.3 eV and the following increase around 0.5 eV. This is a very interesting feature since it is unlike the results of the previous transmission calculations.

In the clean structure, for example, the DOS of the inner unit cell, although it dropped to a remarkable low level, is visibly above zero. The resulting transmission however was much smaller as can be seen in Fig. 6.9 and Fig. 6.8, respectively. This means that the states that contributed to the DOS of the minority spin channel in the clean structure only gave a small contribution to the transmission, whereas here, the in-gap states very well contribute to the transmission of the system. For the LDOS we thus would expect to see an extended minority spin DOS somewhere inside the inner unit cell.

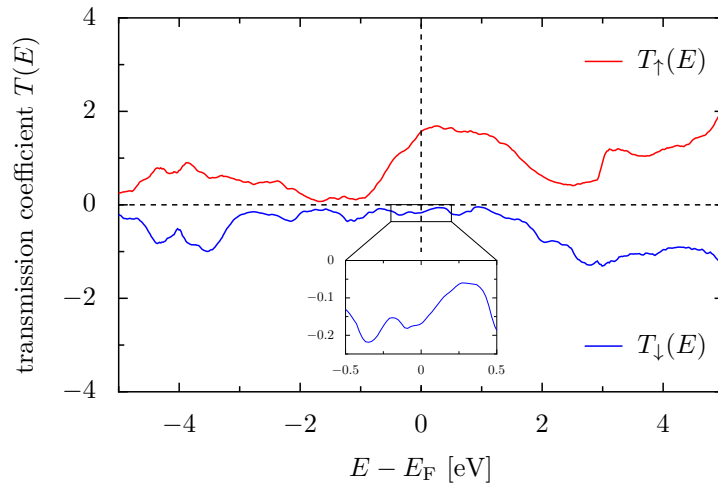


Figure 7.15: Transmission coefficient for the structure including a swapping of a pair of Ni and Mn atoms. The inset zooms into a smaller energy range around the Fermi level for the minority spin channel.

To clarify this assumption, the LDOS is shown in Fig. 7.16. As expected, we indeed observe widely extended blue isosurfaces around the two misplaced atoms, indicating the spacial distribution of the minority spin in-gap states. In the upper NiMnSb unit cell the blue isosurfaces disappear in the middle of the cell, giving a picture similar to that we would expect for a single NiMnSb unit cell in the scattering region. And indeed when the transmission is compared with Fig. 6.5, similarities in shape and value are visible. In that case the transmission showed a small but finite and constant value within the energy range where the gap should be.

Here, on the other hand, the transmission varies much more, which can be attributed to the bonding of the two swapped atoms, as previously shown in the PDOS. However, this gives rise to the question of how important the position of the defect is. In the previous calculation the defect was placed right in the middle of the inner unit cell. According to the results of chapter 6, the formation of a half-metallic

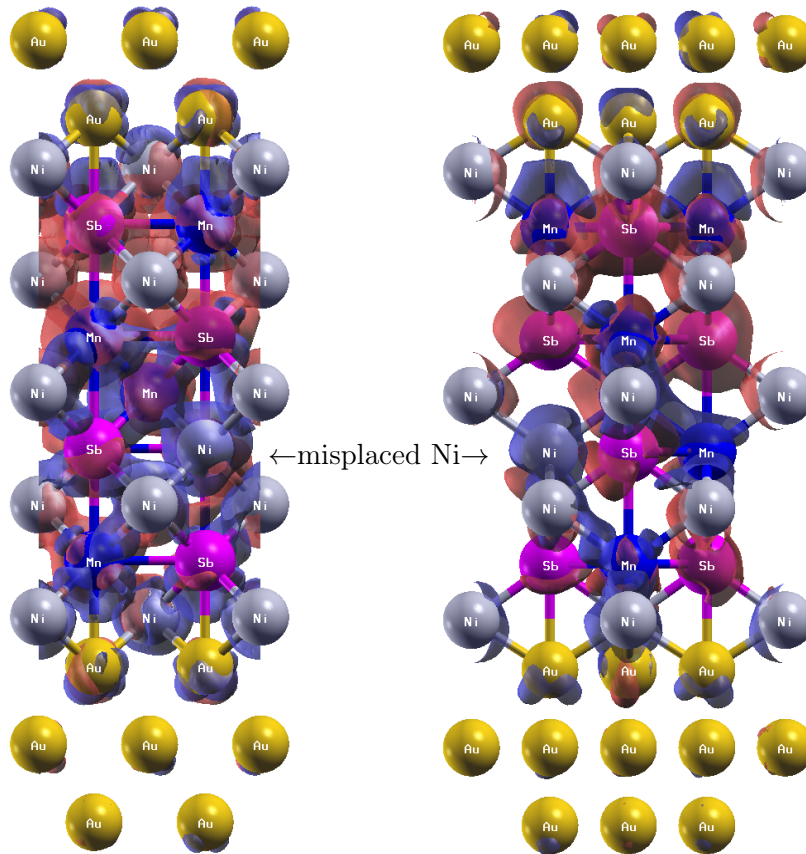


Figure 7.16: LDOS for an energy range of  $\pm 30$  meV around the Fermi level. The blue isosurfaces indicate spacially extended spin- $\downarrow$  states that contribute to the transmission.

unit cell somewhere inside the scattering region is a crucial part in order to generate half-metallic transmission. This is why the positioning of the defect in that area has such a big influence on the transport properties. Therefore the two swapped atoms shall now be moved more towards the interface with the gold leads. There, the half-metallicity is already destroyed due to the different chemical environment. The question is now if the damage of the swapping to the half-metallicity still spreads out into the inner unit cell destroying the half-metallic transmission, or, if a half-metallic unit cell in the middle of the structure can be developed leading to a very high spin polarization in the transmission.

### Current Calculation

The spin polarization of the current (shown in Fig. 7.17), with a value of  $P_C = 0.762$ , is smaller than the one of the transmission, which was found to be  $P_T = 0.805$ . The polarization of the transmission is thus significantly smaller than for the clean structure and also the structure with the Ni vacancy. This is consistent with the results in the previous sections, where the transmission polarization was always higher, although not particularly to that degree.

The polarization values of either transmission or current, are most comparable with the respective values for the clean structure with only one unit cell of NiMnSb in the scattering region ( $P_T = 0.775$  and  $P_C = 0.747$ ). The similarity to the one-unit-cell case is not surprising if we consider the LDOS in Fig. 7.16, where the top unit cell has a small (almost) half-metallic region, just like it was found for one unit cell NiMnSb.

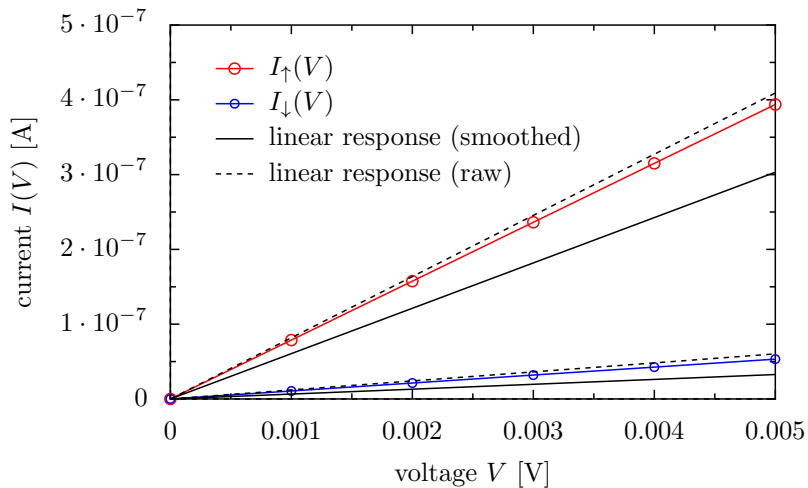


Figure 7.17: Spin-resolved current calculation for the Mn-Ni swapping defect, located in the center of the scattering region.

### Defect near Interface

In the following calculation the defect is moved to the interface layer, meaning that there is now a Mn atom in the layer that connects the Heusler alloy to the gold leads. The misplaced Ni atom is in the neighboring Mn/Sb layer. This defect is from now on called “interface defect” as opposed to the “central defect” that was previously described. Relaxation method 2 (see sec. 7.1) was used again.

Regarding the relaxation process, we observe that the Mn atom behaves similar to the central defect case, as it also moves towards its regular position. The misplaced Ni atom, on the other hand, does not follow the same pattern as it moves in the other direction, towards the gold leads. The Ni atoms at the interfaces with gold on both sides move inwards to the center, whereas the gold atoms at the interface move slightly outwards. This same pattern was observed in all the previous structures. Generally speaking, the movement of the atoms decreases with increasing distance to the defect.

Now we must compare the DOSs that result from those two defect positions. Therefore, Fig. 7.18 shows (in color) the resulting DOS in a smaller range around the Fermi level for interface defect, as well as (in black) the respective DOS of the central defect. Regarding the majority spin channel, the two DOS plots show only minor differences. One of them is that the central defect DOS is generally higher than the one of the interface defect. For the minority spin channel, on the other hand, the situation is completely different. The DOS corresponding to the central defect is again generally higher than the DOS of the interface defect, but to a much

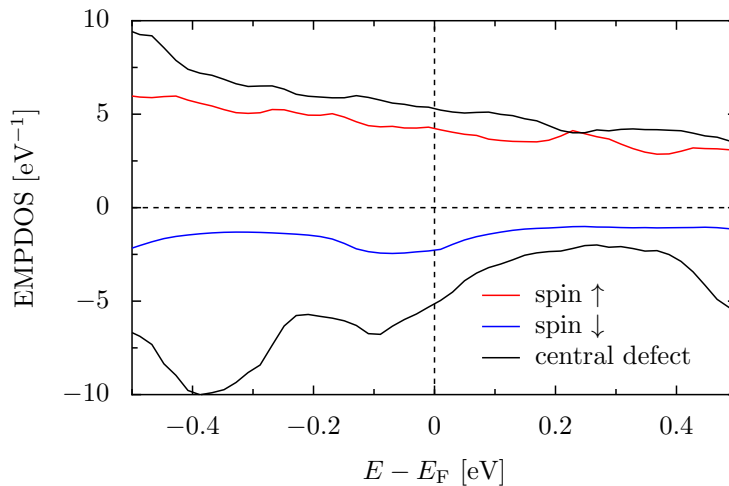


Figure 7.18: Spin-resolved EMPDOS for the central inner unit cell. For comparison: respective data for the central defect (black line)

larger degree. While in the majority spin channel the percental deviation was found to be roughly 50% at its highest value, for the minority spin channel, the percental deviation is **at least** 100% and for  $E - E_F = -0.4$  eV even goes up to roughly 500%.

A huge contribution to the increased DOS for the central defect, at that specific energy, was made by the misplaced Mn atom. In the case of the interface defect this misplaced Mn is as far away from the inner unit cell as possible, which explains the missing increase in the DOS.

The other enhancement of the DOS can be found at  $E - E_F = -0.1$  eV (central and interface defect), and its main contributors are the Ni atoms. In the case of the interface defect the largest contribution comes from the two Ni atoms from the outer layer, which is closer to the defect. These Ni atoms are influenced by the misplaced Ni atom in the neighboring layer. Since both Ni atoms at the edge of the inner unit cell have the same distance to the misplaced Ni atom in the adjacent layer, their influence on the DOS is the same. Similar to the case of the central defect, the enhancement of the DOS is mainly due to the  $3d$  orbitals of the considered Ni atoms. The absence of one of the Mn atoms as bonding partners of those Ni atoms results in a reduced exchange splitting which causes the DOS peaks of the  $3d$  orbitals to move towards the Fermi level, although to a much smaller degree than in the case of the central defect.

Considering the transmission in Fig. 7.19, the results from the DOS are somewhat transferable to the transport properties. Regarding the majority spin channel, we can see that the transmission for the interface defect (in color) exceeds the transmission of the central defect (in black) over large parts of the considered energy range. This is especially interesting since the DOS showed an entirely different situation. When we look at the minority spin channel, we observe that the transmission follows

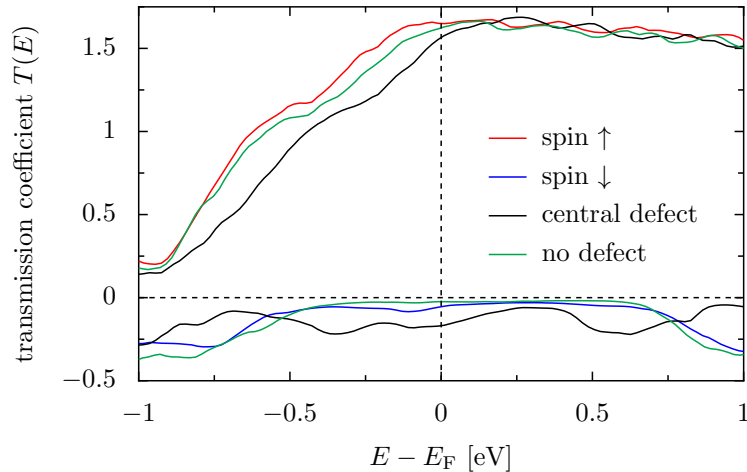


Figure 7.19: Spin-resolved transmission coefficient for the central inner unit cell. For comparison: respective data for the central defect (black line)

the behavior of the DOS quite well. This proportionality of DOS and transmission is already known from the central defect case. The half-metallic gap around the Fermi level is also clearly visible if the transmission is compared with that of the ideal structure without defects (in green). For the central defect this half-metallic gap was not identifiable in that way.

The influence of the position of the defect can also be visualized by using the LDOS as in Fig. 7.20. Near the defect at the bottom part of the Heusler alloy, the minority spin isosurfaces (blue) dominate. The upper part of the Heusler alloy, on the other hand, is completely devoid of minority spin isosurfaces, indicating a huge spin polarization in this area.

Due to the asymmetric nature of the defect, this half-metallic unit cell now moved from the center slightly toward the upper half of the Heusler block. The existence of this half-metallic area inside the scattering region allows for a highly spin-polarized

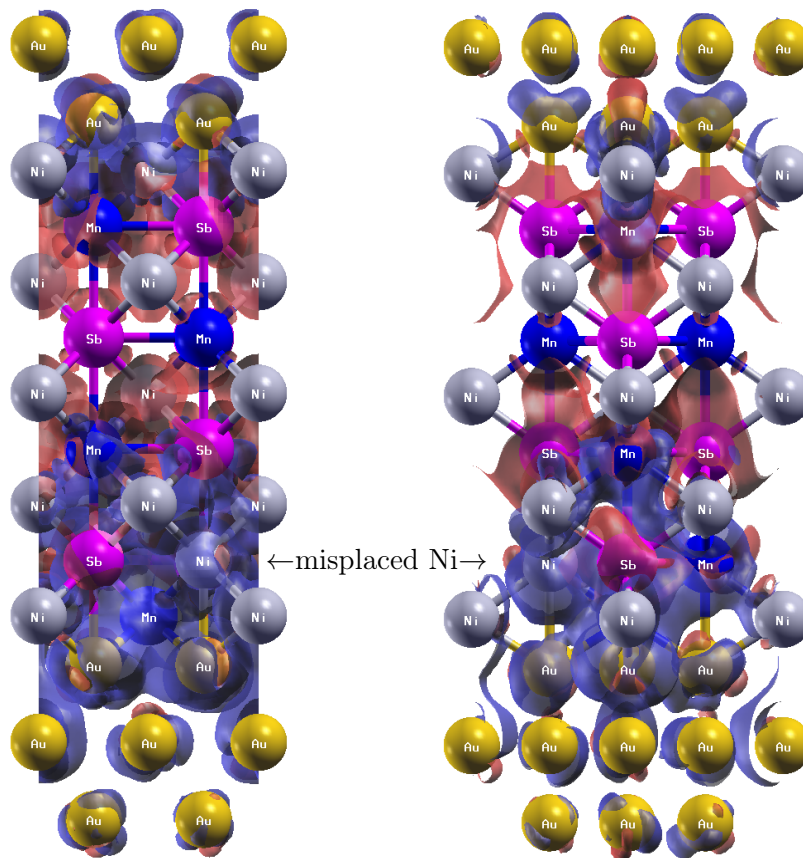


Figure 7.20: LDOS for an energy range of  $\pm 30$  meV around the Fermi level. The half-metallic area is much larger compared to the central defect.

transmission and also for a much more spin-polarized current.

The current for the interface defect is depicted in Fig. 7.21. Its spin polarization  $P_C = 0.935$  is much higher than the one for the central defect ( $P_C = 0.747$ ). The polarization of the transmission shows similar results, as the value for the interface defect  $P_T = 0.936$  is also much larger than the value for the central defect ( $P_T = 0.775$ ). Comparing this with the values for the clean structure,  $P_C = 0.964$  and  $P_T = 0.972$ , we find that the interface defect has almost the same polarization. A strong similarity between the interface defect and the clean structure was also visible in the transmission plot in Fig. 7.19.

In conclusion, we can say that not only the kind of defect matters regarding the transport properties of the system, but also the position of the defect has a crucial impact of the defect on the transmission. The importance of the formation of the half-metallic region within the scattering region becomes clear in this example. In the two-unit-cell case, a defect that has a destructive effect on half-metallicity, such as the swapping of Ni and Mn, can have a devastating effect when it is positioned inside the inner unit cell as the remaining half-metallic area also gets destroyed. Positioned at the interface, however, where the half-metallicity already vanished due to the gold leads, the defect does not cause any harm, so that the inner unit cell is then again half-metallic and thus the current is highly spin-polarized.

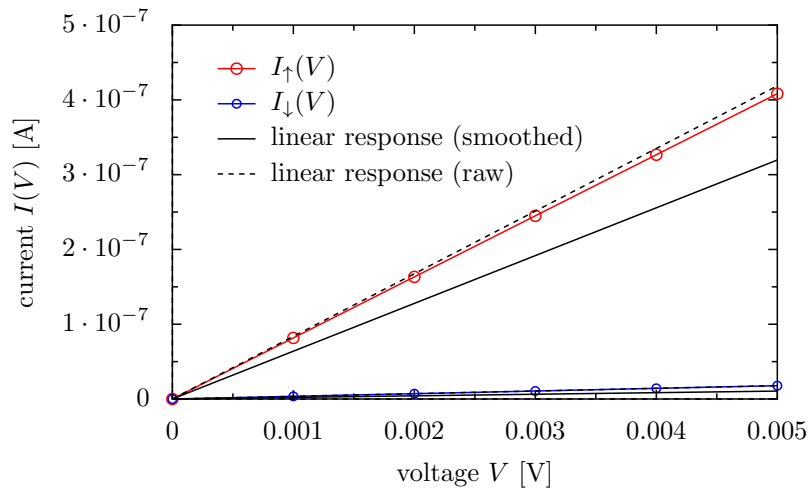


Figure 7.21: Spin-resolved current for the Mn-Ni swapping defect, located at the interface with gold. The spin polarization is much higher compared to the case where the defect is located in the center.

## 7.4 Conclusion

The results of this chapter about the transport properties of NiMnSb under consideration of lattice defects can be summarized as follows.

1. A single Ni vacancy does not cause significant harm to the half-metallic transport. Even though the defect was positioned in the inner unit cell, the most vulnerable part of the scattering region with respect to half-metallicity, the spin polarization of the transmission was still found to be above  $P_T = 0.93$  in contrast to  $P_T = 0.97$  for the ideal structure without any defects.
2. When two unit cells of NiMnSb with a different magnetization are used, the transmission is strongly reduced for both spin channels. The resulting current is of the same order of magnitude as the minority spin current for one (ferromagnetic ordered) unit cell of NiMnSb, adding credibility to this interpretation of the results.
3. This chapter shows that one can find metastable configurations, higher in energy than some other electronic or magnetic configurations. It is difficult to estimate whether these configurations appear in reality, as the resulting energy difference is afflicted by errors and has to be put into context, for example thermal fluctuations. However, similar configurations may be realized by external fields in experiments.
4. Some defects suppress half-metallic transport properties. While the vacated Ni site did not have a huge influence on the transmission, a swapping of Mn and a neighbouring Ni atom, on the other hand, does.
5. The position of the defect matters. For the swapping of Mn with Ni, a defect in the center of the scattering region may severely disrupt the half-metallic transport, whereas a positioning near the interface allows for a half-metallic region inside the scattering region to form and thus enable a highly spin-polarized transmission/current.
6. The relaxation method does not have a huge effect on the transport properties of the structure, even when lattice defects are present. The band gaps in the minority spin transmission were identical, with or without inclusion of the interface layers, although the total energy in the second method (the one that includes the interface) is considerably lower.

A decision which method is to prefer is therefore hard to make. On one hand, the full relaxation of the second method results in a more stable structure, with lower total energy and less stress. On the other hand, it is more expensive with respect to computation time. If the computational effort is bearable, the second method is the one to prefer, just to be on the safe side.

## 8 Summary and Conclusion

In this last chapter we want to summarize the results of this thesis and give an outlook to other aspects that go beyond the subject area and methods used here.

The purpose of the first three chapters of this thesis is to introduce the reader into the topic and make him/her familiar with the methods that are used. In the first chapter, the introduction, an overview over the available literature is given. Theoretical as well as experimental results from the last decades are reviewed in order to convey an impression of the materials under consideration and possible applications.

The second chapter deals with the basics of density functional theory, including a detailed derivation of the Kohn-Sham equations. Furthermore, a brief outline of fundamental properties of the used numeric program, SIESTA, is given. This includes the concept of pseudopotentials, as well as their generation, and the differences between several exchange-correlation functionals that are available in this code.

The third chapter is about transport theory and gives a short introduction to the concept of non-equilibrium Green's function theory. The presented formalism is only valid for non-interacting systems but provides a step-by-step derivation from the Hamiltonian to the Landauer formula for the current. In addition to that, a short introduction to the used transport code, SMEAGOL, is given.

The goal of the fourth chapter is to present a simple toy model that is used to simulate a half-metallic material in its most rudimentary form. The Kronig-Penney model is able to accomplish this task, since it yields multiple bands. Assuming different potentials for different spin channels allows us to mimic a material, where one spin direction has an energy gap while the other one does not. The main result, that is also observable in the SMEAGOL calculation, is that the minority spin transmission, i.e., the one with the band gap, decreases exponentially at the Fermi level as the size of the scattering region increases.

In the fifth chapter we consider the material whose transport properties are the topic of this thesis, namely the ferromagnetic half-metal NiMnSb. The structural parameters such as lattice constant, bulk modulus and its pressure derivative are calculated self-consistently with SIESTA. The resulting band structure, including the half-metallic band gap, together with the atom-resolved projected density of states is discussed in a certain energy range around the Fermi level. In the second part of chapter 5, the transport setup is introduced. This introduction includes the

choice of the lead's material, namely gold, as well as the proper interface geometry. The geometry that was chosen for the subsequent transport calculations is the energetically preferred configuration out of a total number of four. All these configurations implied a transport in [001] direction.

In chapter 6, the transport properties of NiMnSb are discussed. Here, lattice defects are excluded, however, the influence of atomic relaxation is investigated. The calculations include up to four (cubic) unit cells of NiMnSb within the scattering region and are in most parts performed both with and without relaxation. A more detailed conclusion of this chapter can be found in section 6.5.

Chapter 7 then incorporates lattice defects in the form of a vacancy at a Ni site, and a swapping of neighboring Ni and Mn atoms. In one simulation for a system with a vacated Ni site, accidentally, the iteration converged to an interesting metastable anti-ferromagnetic configuration. This observation also helped to confirm some of the trends from the previous chapters. A more detailed conclusion of that chapter can be found in section 7.4.

**Electronic correlations.** An important aspect, that was neglected in this thesis, is the incorporation of electronic correlation. Recently, new research on the transport properties of NiMnSb under consideration of electronic correlations was published. The paper by MORARI *et al.* discusses the spin polarized ballistic transport through correlated Au-NiMnSb-Au heterostructures [98]. Similar to this thesis, the analysis considers various numbers of NiMnSb layers within the scattering region. The geometry is the same as in the previous chapters of this thesis, with the exception that unit cell is smaller. By that, the computational effort is much smaller, and since no lattice defects are investigated, a smaller unit cell has no disadvantages here. DFT

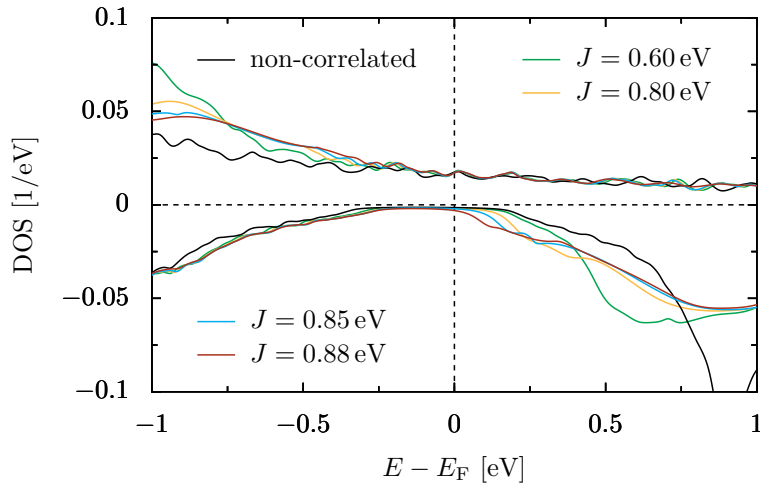


Figure 8.1: Correlated and non-correlated spin-resolved density of states for bulk NiMnSb. Hubbard interaction was set to  $U = 3$  eV for all curves. Data obtained from MORARI *et al.* [98].

calculations are supplemented with local electronic interaction of Hubbard-type on the Mn sites. These correlation effects are incorporated using dynamical mean-field theory (DMFT) [99, 100].

In Fig. 8.1 the bulk density of states for different parameters is displayed. While the Hubbard interaction parameter  $U$  is kept constant at a value of  $U = 3$  eV, the Hund's exchange coupling parameter  $J$  obtains values ranging from 0.6 eV up to 0.88 eV. This parameter  $J$  is responsible for the large magnetic moment at the Mn site. The DOS exhibits in-gap states above the Fermi level with the tendency that these states (the broad shoulders in the energy range of  $E - E_F = 0.125\dots 0.375$  eV) move towards the Fermi level as  $J$  increases. This means that single-particle electron excitations in the minority spin channel exist. The origin of these excitations are attributed to electron-magnon scattering. As a many-body effect, this can not be explained in a single-particle picture. These states are called non-quasiparticle (NQP) states.

Regarding the interface with gold leads, the results show negligible correlation effects near the Fermi level. This feature is observed in Fig. 8.2 for both spin channels. There the DMFT DOS (green) and the non-correlated DOS (yellow) are calculated for a structure containing one unit cell of NiMnSb, and four layers of gold. All densities of states are divided by the total number of valence electrons, namely 400. For comparison the non-correlated bulk DOS is also displayed (black). Considering energies afar from the Fermi level,  $E - E_F \approx \pm 0.5$  eV, the results show that the deviations of the correlated DOS compared to the non-correlated DOS depend on the spin channel. For the majority spin channel these deviations are found below

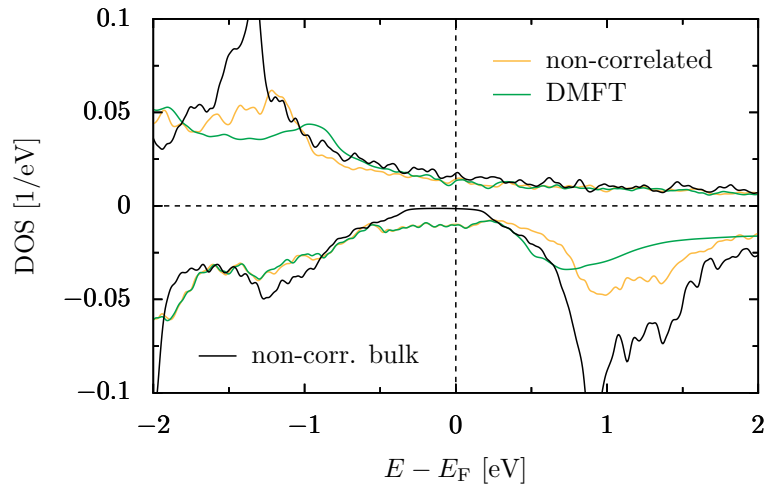


Figure 8.2: Correlated and non-correlated spin-resolved density of states for the Au/NiMnSb/Au heterostructure. The Hubbard interaction was set to  $U = 3$  eV and Hund's rule coupling was set to  $J = 0.6$  eV on the Mn sites for the DMFT calculation. Data obtained from MORARI *et al.* [98].

the Fermi level at energies  $E - E_F < -0.5$  eV, whereas for the minority spin channel the deviations appear above the Fermi level at energies  $E - E_F > 0.4$  eV. The influence of NQP states on the DOS around the Fermi level can not be distinctly exposed, though. The reason for this is the fact that the extended Ni interface states dominate the corresponding energy range and overshadow the NQP states.

The correlated and non-correlated transmission coefficients are displayed in Fig. 8.3. The upper panel depicts the transmission for the two-unit-cell case, and the lower panel the transmission for the one-unit-cell case. A rather clear deviation of the transmission is observed for the majority spin channel at energies larger than  $E - E_F \approx 0.2$  eV for both cases. The magnitude of that deviation is larger for the two-unit-cell case. For low energies, beneath  $E - E_F = -0.7$  eV, the correlated transmission is lower than the non-correlated transmission. In that energy range the deviation is slightly larger for the one-unit-cell case. For the minority spin channel correlated and non-correlated transmissions are almost identical over

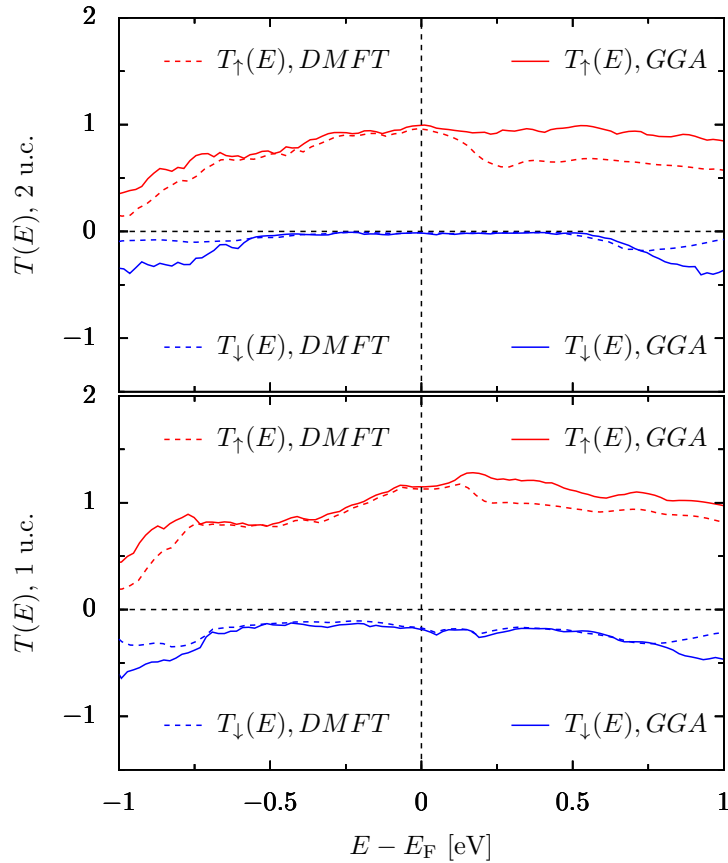


Figure 8.3: Correlated and non-correlated spin-resolved transmission coefficient for one and two unit cells of NiMnSb within the scattering region. Data obtained from MORARI *et al.* [98].

a wide energy range from  $E - E_F = -0.7...0.7$  eV. At very high and very low energies,  $E - E_F \approx \pm 0.8$  eV, the correlated transmission decreases compared to the non-correlated transmission. The order of magnitude of this deviation is roughly the same for both cases, leading to the conclusion that the effects of correlation, are almost independent of the size of the scattering region.

When a narrow energy window around the Fermi level is considered, as it is in the linear response approximation for example, the effects of correlations are negligible. Similar to the non-correlated case we see that the spin polarization of the DOS is reduced, whereas the polarization of the transmission stays at a very high level. This implies, analogously to the interface states in the non-correlated calculation, that the correlated many-body states are localized and thus do not contribute to the transmission.

**Conclusion.** To conclude, one can say that, depending on which measurable quantity of half-metallic ferromagnets are considered, correlation effects may or may not be neglected. Regarding the topic of this thesis, correlation effects definitely play a minor role since they are overshadowed by localized interface states. If these interface states are spacially separated by a larger scattering region, the resulting transmission becomes strongly spin-polarized. Correlation effects do not change that.

When lattice defects play a role, there is no simple answer to the question of how these defects interfere with the spin polarization of the resulting transmission or current. For some defects, for example the vacated Ni site, no significant reduction of the spin polarization is observed. Considering the defects that actually have an impact on the spin polarization of the transmission or current, one has to specify the location of the defect. A defect near the interface has less impact (or none) compared to a defect in the center of the scattering region.

**Outlook.** For future research on this topic many more kinds of defects should be investigated in order to complete the picture. As experimental data from the last two decades has shown, a temperature dependence of the spin polarization is evident. In the case of NiMnSb a critical temperature is 80 K, where a transition from a half-metallic to a normal ferromagnet takes place. It would be very interesting to investigate the transport properties of NiMnSb at temperatures around this transition. Another aspect that was neglected in this thesis is the inclusion of electron-phonon scattering. This could be improved by employing the methods of FREDERIKSEN *et al.*, who extended the NEGF formalism in order to include electron-phonon interactions [101].

Heusler alloys are a very exciting topic regarding spintronic applications. One example is the tunneling magnetoresistance, where two ferromagnetic layers are each connected to leads and are separated by a thin insulating layer. If one is able to switch the magnetization of one of the ferromagnetic layers, with an external field for example, the resistance of this heterostructure changes. In theory, half-metallic ferromagnets such as NiMnSb are ideal for this purpose due to their predicted spin

polarization of 100% at the Fermi level. The result would be a junction that can be switched from a low resistive to a completely insulating behavior. Although such a heterostructure was not the topic of this thesis, we take the freedom to use the obtained results to estimate the efficiency of such a contact.

When we compare the currents for the antiparallel ordered (AFM) structure in section 7.2 with the currents for the ferromagnetic (FM) structure in section 7.1 we are able to calculate a majority spin ( $\delta_{\uparrow}^{\text{MR}}$ ), and total ( $\delta^{\text{MR}}$ ) magnetoresistance (MR) ratio of

$$\delta_{\uparrow}^{\text{MR}} = \frac{I_{\uparrow}^{\text{FM}} - I_{\uparrow}^{\text{AFM}}}{I_{\uparrow}^{\text{AFM}}} \approx 390\%, \quad (8.1)$$

$$\delta^{\text{MR}} = \frac{I^{\text{FM}} - I^{\text{AFM}}}{I^{\text{AFM}}} \approx 158\%. \quad (8.2)$$

These values are promising, considering that the underlying structure consisted of merely two unit cells of NiMnSb. A larger scattering region would definitely result in much larger MR ratios.

Computational analyses like the ones presented in this thesis provide a guideline for experimentalists to conceive and perform suitable experiments for the most promising materials. In theory, however, many aspects are neglected and several approximations have to be made even in the most sophisticated approaches, so that an experimental verification of the theoretical predictions is necessary before reliable conclusions concerning potential technological applications can be drawn.

# Acknowledgement/Danksagung

Here I want to thank everyone who supported me on my way to this point. Special thanks goes to my supervisor Prof. Dr. Ulrich Eckern, who supported and advised me during my time as doctoral candidate. Furthermore I want to thank Prof. Dr. Dr. Udo Schwingenschlögl who helped me with crucial questions in my thesis. For the support regarding the installation and operation of SMEAGOL, I want to thank Dr. Ivan Rungger and Dr. Christian Morari.

Not to forget are my dear colleagues, primary Dr. Wilhelm Appelt, who supported me in the final stage of my thesis, but I also want to thank Sebastian Tölle, Christian Schiegg, Dr. Johannes Wanner, Michael Hartmann and Dr. Michael Dzierzawa for many interesting and helpful (and sometimes scientific) discussions.

Last but not least I want to thank my family and friends for the emotional support and the motivation in critical phases of my time as doctoral candidate, which gave me the strength to hold on until approaching the finish line.

An dieser Stelle möchte ich mich herzlich bei allen Personen bedanken, die mich auf dem Weg zur Promotion tatkräftig unterstützt haben. Besonderer Dank geht hierbei an Prof. Dr. Ulrich Eckern, der mich während meiner Zeit als Doktorand als Betreuer unterstützt und beraten hat. Ebenfalls besonders wichtig um zu diesem Punkt zu kommen, war für mich die Hilfe von Prof. Dr. Dr. Udo Schwingenschlögl der mir bei entscheidenden Fragen während meiner Promotion mit Rat und Tat zur Seite stand. Für die Unterstützung bei der Installation und Bedienung von SMEAGOL möchte ich Dr. Ivan Rungger und Dr. Christian Morari danken.

Nicht zu vergessen sind meine werten Kollegen, hier an erster Stelle Dr. Wilhelm Appelt, der mich sehr in der Schlussphase meiner Promotion unterstützt hat, aber mein Dank geht auch an Sebastian Tölle, Christian Schiegg, Dr. Johannes Wanner, Michael Hartmann und Dr. Michael Dzierzawa für interessante und hilfreiche (manchmal auch wissenschaftliche) Diskussionen.

Zu guter Letzt möchte ich noch meinen Freunden und meiner Familie für die emotionale Unterstützung und die Motivierung in kritischen Phasen meines Doktorandenseins danken, die mir die Kraft gegeben haben bis zum Ende durchzuhalten.



# Bibliography

- [1] F. Heusler, “Über magnetische Manganlegierungen”, *Verhandlungen der Deutschen Physikalischen Gesellschaft* **5**, 219 (1903). (Cited on pages 1 and 2.)
- [2] R. A. de Groot, F. M. Mueller, P. G. van Engen, and K. H. J. Buschow, “New class of materials: Half-metallic ferromagnets”, *Physical Review Letters* **50**, 2024 (1983). (Cited on pages 1, 68, 69 and 71.)
- [3] R. J. Soulen, J. M. Byers, M. S. Osofsky, B. Nadgorny, T. Ambrose, S. Cheng, P. R. Broussard, C. Tanaka, J. Nowak, J. Moodera, et al., “Measuring the spin polarization of a metal with a superconducting point contact”, *Science* **282**, 85 (1998). (Cited on page 1.)
- [4] H. Kato, T. Okuda, Y. Okimoto, Y. Tomioka, K. Oikawa, T. Kamiyama, and Y. Tokura, “Structural and electronic properties of the ordered double perovskites  $A_2MReO_6$  ( $A = Sr, Ca; M = Mg, Sc, Cr, Mn, Fe, Co, Ni, Zn$ )”, *Physical Review B* **69**, 184412 (2004). (Cited on page 1.)
- [5] T. Shishidou, A. Freeman, and R. Asahi, “Effect of GGA on the half-metallicity of the itinerant ferromagnet  $CoS_2$ ”, *Physical Review B* **64**, 180401 (2001). (Cited on page 1.)
- [6] I. Galanakis and P. Mavropoulos, “Towards new half-metallic systems”, *Physical Review B* **67**, 104417 (2002). (Cited on page 2.)
- [7] A. Stroppa, S. Picozzi, A. Continenza, and A. J. Freeman, “Electronic structure and ferromagnetism of Mn-doped group-IV semiconductors”, *Physical Review B* **68**, 155203 (2003). (Cited on page 2.)
- [8] S. Ishida, S. Fujii, S. Kashiwagi, and S. Asano, “Search for half-metallic compounds in  $Co_2MnZ$  ( $Z = IIIb, IVb, Vb$  element)”, *Journal of the Physical Society of Japan* **64**, 2152 (1995). (Cited on page 2.)
- [9] S. Picozzi, A. Continenza, and A. Freeman, “ $Co_2MnX$  ( $X = Si, Ge, Sn$ ) Heusler compounds: An ab initio study of their structural, electronic, and magnetic properties at zero and elevated pressure”, *Physical Review B* **66**, 094421 (2002). (Cited on page 2.)
- [10] M. Jourdan, J. Minár, J. Braun, A. Kronenberg, S. Chadov, B. Balke, A. Gloskovskii, M. Kolbe, H. Elmers, G. Schönhense, et al., “Direct obser-

- vation of half-metallicity in the Heusler compound  $\text{Co}_2\text{MnSi}$ ", *Nature Communications* **5** (2014). (Cited on page 2.)
- [11] A. Birsan and P. Palade, "Band structure calculations of  $\text{Ti}_2\text{FeSn}$ : A new half-metallic compound", *Intermetallics* **36**, 86 (2013). (Cited on page 2.)
- [12] I. Galanakis, P. Mavropoulos, and P. Dederichs, "Introduction to half-metallic Heusler alloys: electronic structure and magnetic properties", arXiv preprint cond-mat/0510276 (2005). (Cited on page 2.)
- [13] R. A. De Groot, A. M. van der Kraan, and K. H. J. Buschow, "FeMnSb: a half-metallic ferrimagnet", *Journal of Magnetism and Magnetic Materials* **61**, 330 (1986). (Cited on page 2.)
- [14] I. Galanakis, K. Özdoğan, and E. Şaşıoğlu, "Ab initio electronic and magnetic properties of half-metallic NiCrSi and NiMnSi Heusler alloys: The role of defects and interfaces", *Journal of Applied Physics* **104**, 083916 (2008). (Cited on pages 2 and 68.)
- [15] S. Picozzi, A. Continenza, and A. Freeman, "First principles study of electronic and magnetic properties of  $\text{Co}_2\text{MnGe}/\text{GaAs}$  interfaces", *Journal of Physics and Chemistry of Solids* **64**, 1697 (2003). (Cited on page 3.)
- [16] S. Picozzi and A. J. Freeman, "Polarization reduction in half-metallic Heusler alloys: the effect of point defects and interfaces with semiconductors", *Journal of Physics: Condensed Matter* **19**, 315215 (2007). (Cited on page 3.)
- [17] I. Galanakis, "Towards half-metallic interfaces:  $\text{Co}_2\text{CrAl}/\text{InP}$  contacts", *Journal of Physics: Condensed Matter* **16**, 8007 (2004). (Cited on page 3.)
- [18] M. Ležaić, I. Galanakis, G. Bihlmayer, and S. Blügel, "Structural and magnetic properties of the (001) and (111) surfaces of the half-metal NiMnSb", *Journal of Physics: Condensed Matter* **17**, 3121 (2005). (Cited on page 3.)
- [19] G. Bona, F. Meier, M. Taborelli, E. Bucher, and P. Schmidt, "Spin polarized photoemission from NiMnSb", *Solid State Communications* **56**, 391 (1985). (Cited on page 3.)
- [20] S. K. Clowes, Y. Miyoshi, Y. Bugoslavsky, W. R. Branford, C. Grigorescu, S. A. Manea, O. Monnereau, and L. F. Cohen, "Spin polarization of the transport current at the free surface of bulk NiMnSb", *Physical Review B* **69**, 214425 (2004). (Cited on page 3.)
- [21] L. Ritchie, G. Xiao, Y. Ji, T. Y. Chen, C. L. Chien, M. Zhang, J. Chen, Z. Liu, G. Wu, and X. X. Zhang, "Magnetic, structural, and transport properties of the Heusler alloys  $\text{Co}_2\text{MnSi}$  and NiMnSb", *Physical Review B* **68**, 104430 (2003). (Cited on page 3.)

- [22] P. Turban, S. Andrieu, B. Kierren, E. Snoeck, C. Teodorescu, and A. Traverse, “Growth and characterization of single crystalline NiMnSb thin films and epitaxial NiMnSb/MgO/NiMnSb(001) trilayers”, *Physical Review B* **65**, 134417 (2002). (Cited on page 3.)
- [23] T. Komesu, C. Borca, H.-K. Jeong, P. Dowben, D. Ristoiu, J. Nozières, S. Stadler, and Y. Idzerda, “The polarization of Sb overlayers on NiMnSb (100)”, *Physics Letters A* **273**, 245 (2000). (Cited on page 3.)
- [24] B. Alling, S. Shallcross, and I. Abrikosov, “Role of stoichiometric and nonstoichiometric defects on the magnetic properties of the half-metallic ferromagnet NiMnSb”, *Physical Review B* **73**, 064418 (2006). (Cited on page 4.)
- [25] B. Jenichen, J. Herfort, T. Hentschel, A. Nikulin, X. Kong, A. Trampert, and I. Žižak, “Residual disorder and diffusion in thin Heusler alloy films”, *Physical Review B* **86**, 075319 (2012). (Cited on page 4.)
- [26] J.-P. Schlomka, M. Tolan, and W. Press, “In situ growth study of NiMnSb films on MgO (001) and Si (001)”, *Applied Physics Letters* **76**, 2005 (2000). (Cited on page 4.)
- [27] P. Larson, S. D. Mahanti, and M. G. Kanatzidis, “Structural stability of Ni-containing half-Heusler compounds”, *Physical Review B* **62**, 12754 (2000). (Cited on page 4.)
- [28] D. Orgassa, H. Fujiwara, T. C. Schulthess, and W. H. Butler, “First-principles calculation of the effect of atomic disorder on the electronic structure of the half-metallic ferromagnet NiMnSb”, *Physical Review B* **60**, 13237 (1999). (Cited on page 4.)
- [29] Y. Kudryavtsev, V. Uvarov, V. Oksenenko, Y. Lee, J. Kim, Y. Hyun, K. Kim, J. Rhee, and J. Dubowik, “Effect of disorder on various physical properties of Co<sub>2</sub>CrAl Heusler alloy films: Experiment and theory”, *Physical Review B* **77**, 195104 (2008). (Cited on page 4.)
- [30] H. Xie, H. Wang, Y. Pei, C. Fu, X. Liu, G. J. Snyder, X. Zhao, and T. Zhu, “Beneficial Contribution of Alloy Disorder to Electron and Phonon Transport in Half-Heusler Thermoelectric Materials”, *Advanced Functional Materials* **23**, 5123 (2013). (Cited on page 4.)
- [31] P. Hasnip, J. Smith, and V. Lazarov, “Ab initio studies of disorder in the full Heusler alloy Co<sub>2</sub>Fe<sub>x</sub>Mn<sub>1-x</sub>Si”, *Journal of Applied Physics* **113**, 17B106 (2013). (Cited on page 4.)
- [32] F. Mancoff, B. Clemens, E. Singley, and D. Basov, “Infrared probe of the electronic structure and carrier scattering in NiMnSb thin films”, *Physical Review B* **60**, R12565 (1999). (Cited on page 4.)

- [33] L. Chioncel, E. Arrigoni, M. I. Katsnelson, and A. I. Lichtenstein, “Electron Correlations and the Minority-Spin Band Gap in Half-Metallic Heusler Alloys”, *Physical Review Letters* **96**, 137203 (2006). (Cited on page 5.)
- [34] L. Chioncel, H. Allmaier, E. Arrigoni, A. Yamasaki, M. Daghofer, M. I. Katsnelson, and A. I. Lichtenstein, “Half-metallic ferromagnetism and spin polarization in  $\text{CrO}_2$ ”, *Physical Review B* **75**, 140406 (2007). (Cited on page 5.)
- [35] M. I. Katsnelson, V. Y. Irkhin, L. Chioncel, A. I. Lichtenstein, and R. A. de Groot, “Half-metallic ferromagnets: From band structure to many-body effects”, *Reviews of Modern Physics* **80**, 315 (2008). (Cited on page 5.)
- [36] H. Allmaier, L. Chioncel, E. Arrigoni, M. I. Katsnelson, and A. I. Lichtenstein, “Half-metallicity in  $\text{NiMnSb}$ : A variational cluster approach with ab initio parameters”, *Physical Review B* **81**, 054422 (2010). (Cited on page 5.)
- [37] L. Chioncel, M. I. Katsnelson, R. A. de Groot, and A. I. Lichtenstein, “Non-quasiparticle states in the half-metallic ferromagnet  $\text{NiMnSb}$ ”, *Physical Review B* **68**, 144425 (2003). (Cited on page 5.)
- [38] C. Borca, D. Ristoiu, H. Jeong, T. Komesu, A. Caruso, J. Pierre, L. Ranno, J. Nozieres, and P. A. Dowben, “Epitaxial growth and surface properties of half-metal  $\text{NiMnSb}$  films”, *Journal of Physics: Condensed Matter* **19**, 315211 (2007). (Cited on page 5.)
- [39] K. E. H. M. Hanssen, P. E. Mijnders, L. P. L. M. Rabou, and K. H. J. Buschow, “Positron-annihilation study of the half-metallic ferromagnet  $\text{NiMnSb}$ : Experiment”, *Physical Review B* **42**, 1533 (1990). (Cited on page 5.)
- [40] M. Kirillova, A. Makhnev, E. Shreder, V. Dyakina, and N. Gorina, “Interband Optical Absorption and Plasma Effects in Half-Metallic  $\text{XMnY}$  Ferromagnets”, *physica status solidi (b)* **187**, 231 (1995). (Cited on page 5.)
- [41] C. Hordequin, E. Lelievre-Berna, and J. Pierre, “Magnetization density in the half-metallic ferromagnet  $\text{NiMnSb}$ ”, *Physica B: Condensed Matter* **234**, 602 (1997). (Cited on page 5.)
- [42] C. Hordequin, J. Pierre, and R. Currat, “Magnetic excitations in the half-metallic  $\text{NiMnSb}$  ferromagnet: From Heisenberg-type to itinerant behaviour”, *Journal of Magnetism and Magnetic Materials* **162**, 75 (1996). (Cited on page 5.)
- [43] C. N. Borca, T. Komesu, H.-K. Jeong, P. A. Dowben, D. Ristoiu, C. Hordequin, J. P. Nozières, J. Pierre, S. Stadler, and Y. U. Idzerda, “Evidence for temperature dependent moments ordering in ferromagnetic  $\text{NiMnSb}(100)$ ”, *Physical Review B* **64**, 052409 (2001). (Cited on page 5.)

- [44] C. Hordequin, D. Ristoiu, L. Ranno, and J. Pierre, “On the cross-over from half-metal to normal ferromagnet in NiMnSb”, *The European Physical Journal B: Condensed Matter and Complex Systems* **16**, 287 (2000). (Cited on page 5.)
- [45] I. Galanakis, P. H. Dederichs, and N. Papanikolaou, “Origin and properties of the gap in the half-ferromagnetic Heusler alloys”, *Physical Review B* **66**, 134428 (2002). (Cited on page 5.)
- [46] S. Majumdar, M. Chattopadhyay, V. Sharma, K. Sokhey, S. Roy, and P. Chad-dah, “Transport properties of the ferromagnetic Heusler alloy  $\text{Co}_2\text{TiSn}$ ”, *Physical Review B* **72**, 012417 (2005). (Cited on page 6.)
- [47] M. Otto, R. Van Woerden, P. Van der Valk, J. Wijngaard, C. Van Bruggen, and C. Haas, “Half-metallic ferromagnets. II. Transport properties of NiMnSb and related inter-metallic compounds”, *Journal of Physics: Condensed Matter* **1**, 2351 (1989). (Cited on page 6.)
- [48] N. Anh Tuan and N. Phuc Duong, “Structural, magnetic, and magnetotransport properties of NiMnSb thin films deposited by flash evaporation”, *Applied Physics Letters* **99**, 162507 (2011). (Cited on page 6.)
- [49] S. Gardelis, J. Androulakis, J. Giapintzakis, O. Monnereau, and P. D. Buckle, “Structural, magnetic, and electrical properties of NiMnSb thin films grown on InSb by pulsed-laser deposition”, *Applied Physics Letters* **85**, 3178 (2004). (Cited on page 6.)
- [50] Z. Wen, T. Kubota, T. Yamamoto, and K. Takanashi, “Fully epitaxial  $\text{C1}_b$ -type NiMnSb half-Heusler alloy films for current-perpendicular-to-plane giant magnetoresistance devices with a Ag spacer”, *Scientific Reports* **5**, 18387 (2015). (Cited on page 6.)
- [51] W. Zou, Z. Lu, S. Wang, G. Yan, S. Li, L. Li, W. Miao, L. Lu, F. Zhang, and Y. Du, “Investigation on the magnetism and transport properties of NiMnSb polycrystalline films with oxidized grain surface”, *Journal of Magnetism and Magnetic Materials* **321**, 291 (2009). (Cited on page 6.)
- [52] R. Kabani, M. Terada, A. Roshko, and J. Moodera, “Magnetic properties of NiMnSb films”, *Journal of Applied Physics* **67**, 4898 (1990). (Cited on page 6.)
- [53] R. Meservey, P. Tedrow, and J. Moodera, “Electron spin polarized tunneling study of ferromagnetic thin films”, *Journal of Magnetism and Magnetic Materials* **35**, 1 (1983). (Cited on page 7.)
- [54] J. Moodera and D. Mootoo, “Nature of half-metallic ferromagnets: Transport studies”, *Journal of Applied Physics* **76**, 6101 (1994). (Cited on page 7.)
- [55] J. Giapintzakis, C. Grigorescu, A. Klini, A. Manousaki, V. Zorba, J. Androulakis, Z. Viskadourakis, and C. Fotakis, “Low-temperature growth of

- NiMnSb thin films by pulsed-laser deposition”, *Applied Physics Letters* **80**, 2716 (2002). (Cited on page 7.)
- [56] J. Caballero, A. Reilly, Y. Hao, J. Bass, W. Pratt, F. Petroff, and J. Childress, “Effect of deposition parameters on the CPP-GMR of NiMnSb-based spin-valve structures”, *Journal of Magnetism and Magnetic Materials* **198**, 55 (1999). (Cited on page 7.)
- [57] V. G. Harris and Y. Chen, “Equilibrium Chemical Disorder at the Surface of a Single-Crystal  $C1_b$  NiMnSb Half-Heusler Alloy: Implications for Spintronics”, *IEEE Magnetics Letters* **6**, 1 (2015). (Cited on page 7.)
- [58] S. Gardelis, J. Androulakis, O. Monnereau, P. D. Buckle, and J. Giapintzakis, “Possible use of the half-Heusler alloy NiMnSb in spintronics: synthesis and physical properties of arc melted NiMnSb and of NiMnSb thin films grown on InSb by pulsed laser deposition”, *Journal of Physics: Conference Series* **10**, 167 (2005). (Cited on page 7.)
- [59] C. Ciccarelli, L. Anderson, V. Tshitoyan, A. Ferguson, F. Gerhard, C. Gould, L. Molenkamp, J. Gayles, J. Železný, L. Šmejkal, et al., “Room-temperature spin-orbit torque in NiMnSb”, *Nature Physics* (2016). (Cited on page 7.)
- [60] Y. Sakuraba, M. Hattori, M. Oogane, Y. Ando, H. Kato, A. Sakuma, T. Miyazaki, and H. Kubota, “Giant tunneling magnetoresistance in  $\text{Co}_2\text{MnSi}/\text{AlO}/\text{Co}_2\text{MnSi}$  magnetic tunnel junctions”, *Applied Physics Letters* **88**, 192508 (2006). (Cited on page 7.)
- [61] A. Thomas, D. Meyners, D. Ebke, N.-N. Liu, M. D. Sacher, J. Schmalhorst, G. Reiss, H. Ebert, and A. Hütten, “Inverted spin polarization of Heusler alloys for spintronic devices”, *Applied Physics Letters* **89**, 012502 (2006). (Cited on page 7.)
- [62] W. Wang, H. Sukegawa, R. Shan, T. Furubayashi, and K. Inomata, “Preparation and characterization of highly  $L2_1$ -ordered full-Heusler alloy  $\text{Co}_2\text{FeAl}_{0.5}\text{Si}_{0.5}$  thin films for spintronics device applications”, *Applied Physics Letters* **92**, 221912 (2008). (Cited on page 7.)
- [63] T. Graf, S. S. Parkin, and C. Felser, “Heusler compounds - A material class with exceptional properties”, *IEEE Transactions on Magnetics* **47**, 367 (2011). (Cited on page 7.)
- [64] C. Wang, J. Meyer, N. Teichert, A. Auge, E. Rausch, B. Balke, A. Hütten, G. H. Fecher, and C. Felser, “Heusler nanoparticles for spintronics and ferromagnetic shape memory alloys”, *Journal of Vacuum Science & Technology B, Nanotechnology and Microelectronics: Materials, Processing, Measurement, and Phenomena* **32**, 020802 (2014). (Cited on page 7.)

- [65] A. Hirohata, J. Sagar, L. Lari, L. R. Fleet, and V. K. Lazarov, “Heusler-alloy films for spintronic devices”, *Applied Physics A* **111**, 423 (2013). (Cited on page 8.)
- [66] F. Casper, T. Graf, S. Chadov, B. Balke, and C. Felser, “Half-Heusler compounds: novel materials for energy and spintronic applications”, *Semiconductor Science and Technology* **27**, 063001 (2012). (Cited on page 8.)
- [67] P. Hohenberg and W. Kohn, “Inhomogeneous Electron Gas”, *Physical Review* **136**, B864 (1964). (Cited on page 9.)
- [68] G. Giuliani and G. Vignale, *Quantum theory of the electron liquid* (Cambridge University Press, 2005). (Cited on page 11.)
- [69] M. Levy, “Universal variational functionals of electron densities, first-order density matrices, and natural spin-orbitals and solution of the v-representability problem”, *Proceedings of the National Academy of Sciences* **76**, 6062 (1979). (Cited on page 12.)
- [70] W. Kohn and L. J. Sham, “Self-Consistent Equations Including Exchange and Correlation Effects”, *Physical Review* **140**, A1133 (1965). (Cited on page 13.)
- [71] D. M. Ceperley and B. Alder, “Ground state of the electron gas by a stochastic method”, *Physical Review Letters* **45**, 566 (1980). (Cited on page 21.)
- [72] J. P. Perdew and Y. Wang, “Accurate and simple analytic representation of the electron-gas correlation energy”, *Physical Review B* **45**, 13244 (1992). (Cited on page 21.)
- [73] J. P. Perdew, K. Burke, and M. Ernzerhof, “Generalized gradient approximation made simple”, *Physical Review Letters* **77**, 3865 (1996). (Cited on page 21.)
- [74] Y. Zhang and W. Yang, “Comment on “Generalized gradient approximation made simple””, *Physical Review Letters* **80**, 890 (1998). (Cited on page 21.)
- [75] B. Hammer, L. B. Hansen, and J. K. Nørskov, “Improved adsorption energetics within density-functional theory using revised Perdew-Burke-Ernzerhof functionals”, *Physical Review B* **59**, 7413 (1999). (Cited on page 21.)
- [76] J. M. Soler, E. Artacho, J. D. Gale, A. García, J. Junquera, P. Ordejón, and D. Sánchez-Portal, “The SIESTA method for ab initio order-N materials simulation”, *Journal of Physics: Condensed Matter* **14**, 2745 (2002). (Cited on page 22.)
- [77] J. C. Phillips and L. Kleinman, “New Method for Calculating Wave Functions in Crystals and Molecules”, *Physical Review* **116**, 287 (1959). (Cited on page 23.)

- [78] N. Troullier and J. L. Martins, “Efficient pseudopotentials for plane-wave calculations”, *Physical Review B* **43**, 1993 (1991). (Cited on page 24.)
- [79] D. R. Hamann, M. Schlüter, and C. Chiang, “Norm-Conserving Pseudopotentials”, *Physical Review Letters* **43**, 1494 (1979). (Cited on pages 24 and 26.)
- [80] L. Kleinman and D. M. Bylander, “Efficacious Form for Model Pseudopotentials”, *Physical Review Letters* **48**, 1425 (1982). (Cited on page 25.)
- [81] S. G. Louie, S. Froyen, and M. L. Cohen, “Nonlinear ionic pseudopotentials in spin-density-functional calculations”, *Physical Review B* **26**, 1738 (1982). (Cited on page 27.)
- [82] M. Paulsson, “Non equilibrium green’s functions for dummies: Introduction to the one particle NEGF equations”, arXiv preprint cond-mat/0210519 (2002). (Cited on page 33.)
- [83] I. N. Bronstein, K. A. Semendjajew, G. Musiol, and H. Mühlig, “Taschenbuch der Mathematik”, ISBN 3817120052, p. 782 (2001). (Cited on page 39.)
- [84] Y. Meir and N. S. Wingreen, “Landauer formula for the current through an interacting electron region”, *Physical Review Letters* **68**, 2512 (1992). (Cited on page 40.)
- [85] M. Büttiker, Y. Imry, R. Landauer, and S. Pinhas, “Generalized many-channel conductance formula with application to small rings”, *Physical Review B* **31**, 6207 (1985). (Cited on page 40.)
- [86] H. Haug and A.-P. Jauho, *Quantum kinetics in transport and optics of semiconductors*, vol. 2 (Springer, 2008). (Cited on page 40.)
- [87] A. R. Rocha, V. M. García-Suárez, S. Bailey, C. Lambert, J. Ferrer, and S. Sanvito, “Spin and molecular electronics in atomically generated orbital landscapes”, *Physical Review B* **73**, 085414 (2006). (Cited on page 41.)
- [88] I. Rungger and S. Sanvito, “Algorithm for the construction of self-energies for electronic transport calculations based on singularity elimination and singular value decomposition”, *Physical Review B* **78**, 035407 (2008). (Cited on page 41.)
- [89] R. d. L. Kronig and W. Penney, in *Proceedings of the Royal Society of London A: Mathematical, Physical and Engineering Sciences* (The Royal Society, 1931), vol. 130, pp. 499–513. (Cited on page 43.)
- [90] F. Bloch, “Über die Quantenmechanik der Elektronen in Kristallgittern”, *Zeitschrift für Physik A: Hadrons and Nuclei* **52**, 555 (1929). (Cited on page 44.)

- [91] P. Markoš and C. M. Soukoulis, *Wave propagation: from electrons to photonic crystals and left-handed materials* (Princeton University Press, 2008). (Cited on page 49.)
- [92] A. Eisenbach, Y. Bliokh, V. Freilikh, M. Kaveh, and R. Berkovits, “Transmission resonances anomaly in one-dimensional disordered quantum systems”, *Physical Review B* **94**, 014207 (2016). (Cited on page 61.)
- [93] F. Murnaghan, “The compressibility of media under extreme pressures”, *Proceedings of the National Academy of Sciences* **30**, 244 (1944). (Cited on page 69.)
- [94] W. Van Roy, J. De Boeck, B. Brijs, and G. Borghs, “Epitaxial NiMnSb films on GaAs(001)”, *Applied Physics Letters* **77(25)**, 4190 (2000). (Cited on page 70.)
- [95] I. Galanakis, P. Dederichs, and N. Papanikolaou, “Slater-Pauling behavior and origin of the half-metallicity of the full-Heusler alloys”, *Physical Review B* **66**, 174429 (2002). (Cited on page 71.)
- [96] H. J. Monkhorst and J. D. Pack, “Special points for Brillouin-zone integrations”, *Physical Review B* **13**, 5188 (1976). (Cited on page 78.)
- [97] R.-J. Zhang, U. Eckern, and U. Schwingenschlögl, “Fate of half-metallicity near interfaces: the case of NiMnSb/MgO and NiMnSi/MgO”, *ACS Applied Materials & Interfaces* **6**, 14516 (2014). (Cited on page 99.)
- [98] C. Morari, W. Appelt, A. Östlin, A. Prinz-Zwick, U. Schwingenschlögl, U. Eckern, and L. Chioncel, “Spin-polarized ballistic conduction through correlated Au-NiMnSb-Au heterostructures”, *Physical Review B* **96**, 205137 (2017). (Cited on pages 128, 129 and 130.)
- [99] A. Georges, G. Kotliar, W. Krauth, and M. J. Rozenberg, “Dynamical mean-field theory of strongly correlated fermion systems and the limit of infinite dimensions”, *Reviews of Modern Physics* **68**, 13 (1996). (Cited on page 129.)
- [100] G. Kotliar, S. Y. Savrasov, K. Haule, V. S. Oudovenko, O. Parcollet, and C. A. Marianetti, “Electronic structure calculations with dynamical mean-field theory”, *Reviews of Modern Physics* **78**, 865 (2006). (Cited on page 129.)
- [101] T. Frederiksen, M. Brandbyge, N. Lorente, and A.-P. Jauho, “Inelastic scattering and local heating in atomic gold wires”, *Physical Review Letters* **93**, 256601 (2004). (Cited on page 131.)